P5 MARTIJN NIJKAMP
4660839

3D Printing in Construction

On the gap between innovation and practical use.

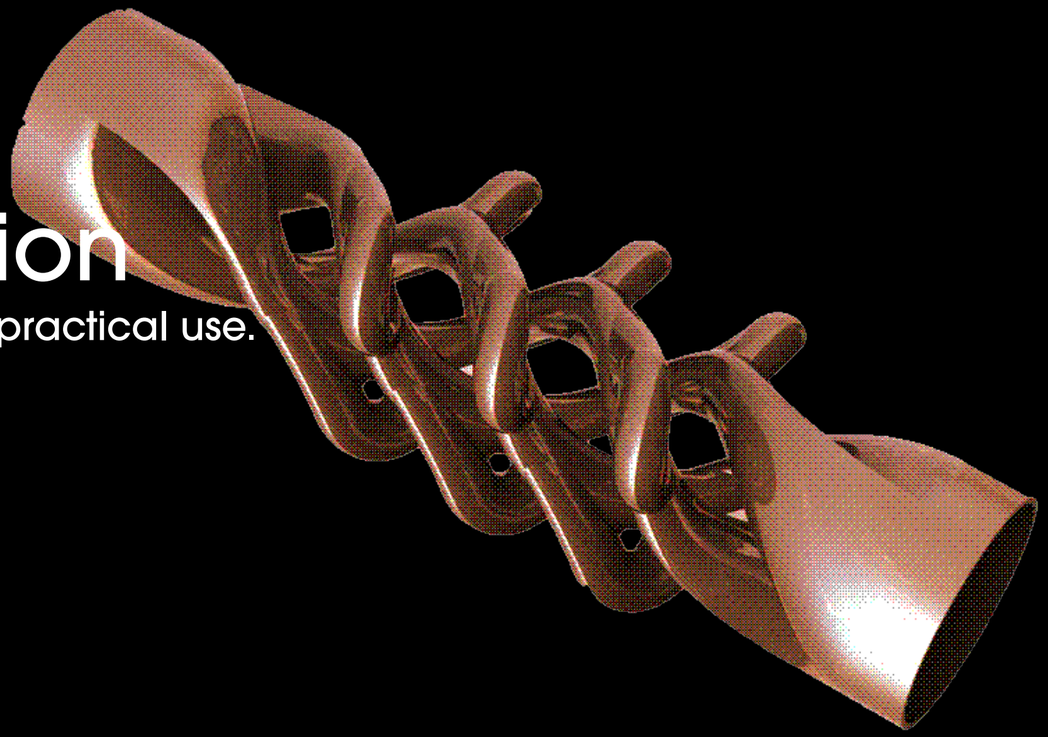

First mentor
Dr.ing. M. Bilow

Second mentor
Ir. E.R. van den Ham

DELFT 24/06/2024

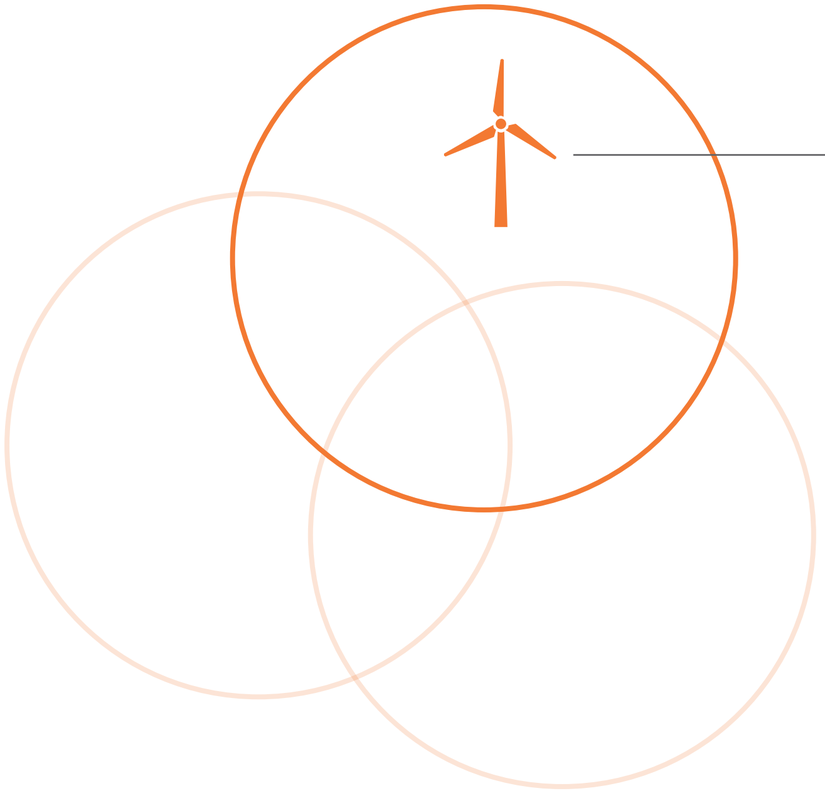

CURRENT PREDICAMENTS

ENERGY TRANSITION

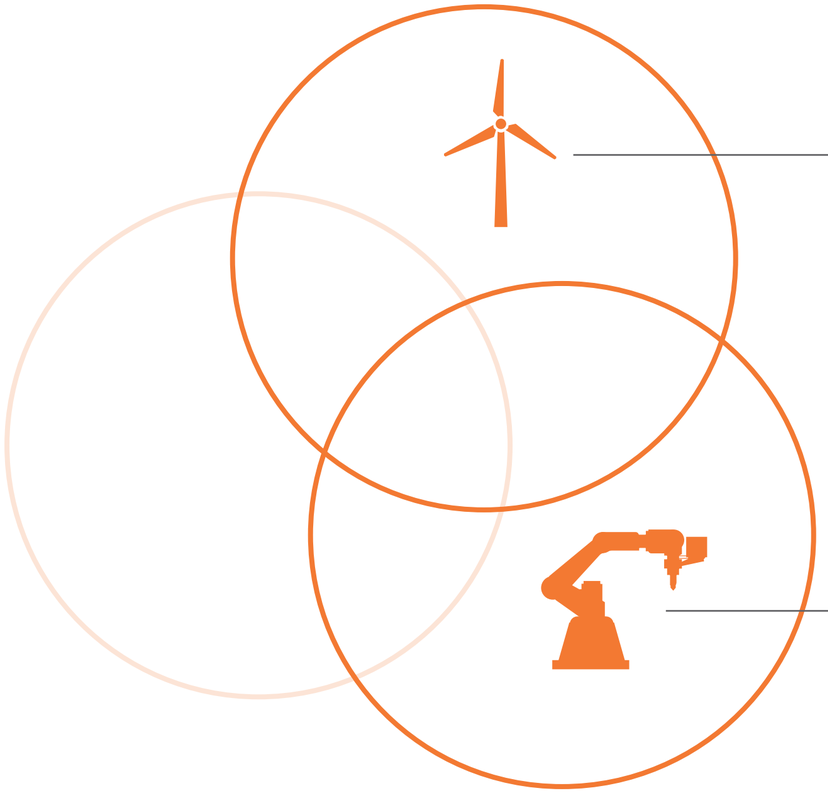

CURRENT PREDICAMENTS
ENERGY TRANSITION

HIGH-TECH
MANUFACTURING
3D-PRINTING

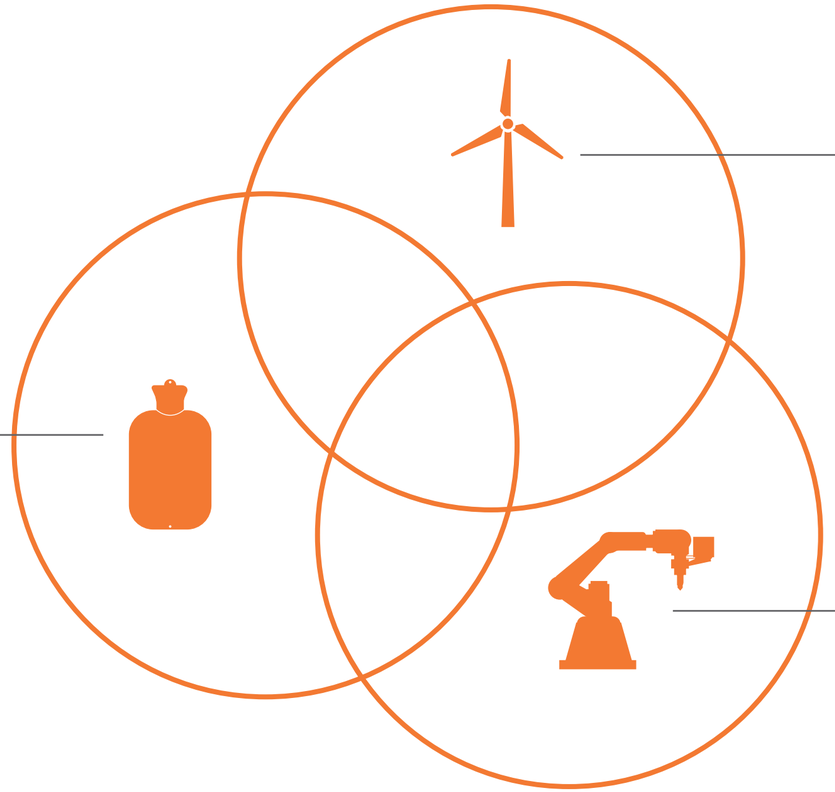

RESILIENT
SOLUTIONS
HEATING &
VENTILATION

CURRENT PREDICAMENTS
ENERGY TRANSITION

HIGH-TECH
MANUFACTURING
3D-PRINTING

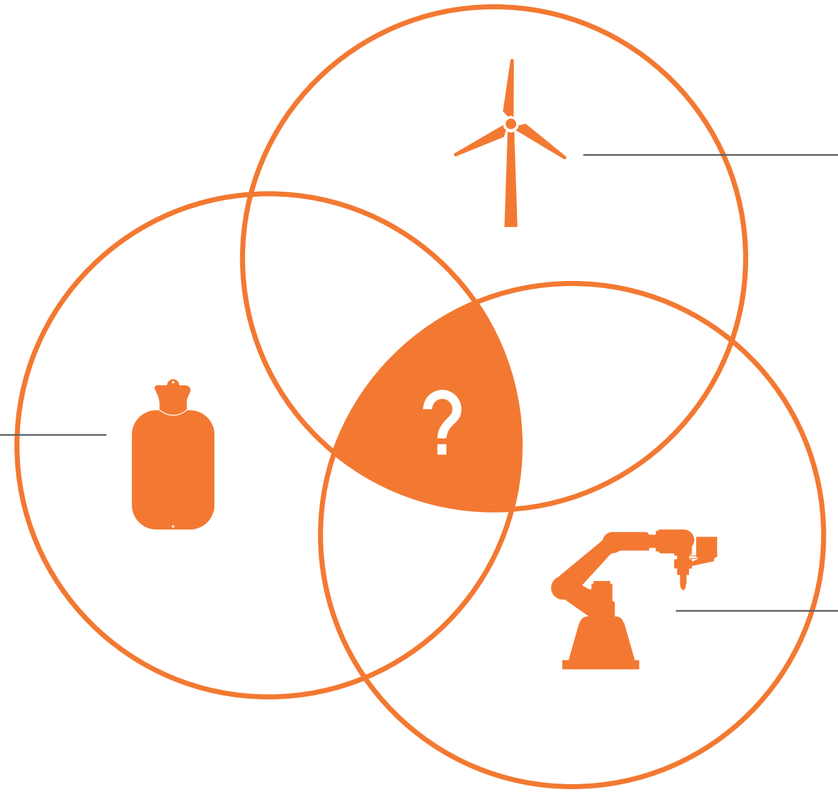

CURRENT PREDICAMENTS
ENERGY TRANSITION

RESILIENT SOLUTIONS
HEATING & VENTILATION

HIGH-TECH MANUFACTURING
3D-PRINTING

FOSSIL ENERGY

ENERGY TRANSITION

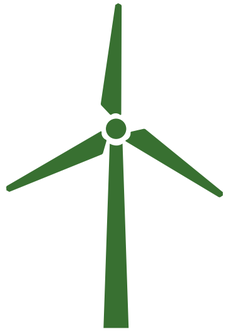

GREEN ENERGY

FOSSIL ENERGY

ENERGY TRANSITION

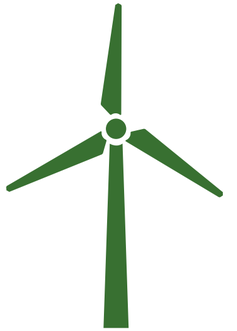

GREEN ENERGY

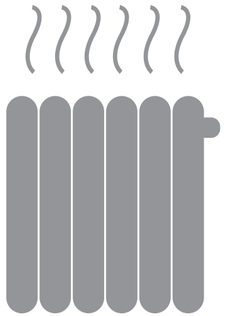

COMPLEX

FOSSIL ENERGY

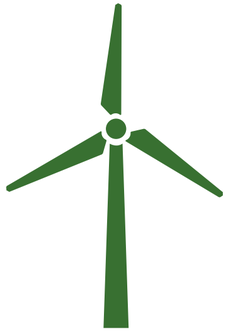

ENERGY TRANSITION

GREEN ENERGY

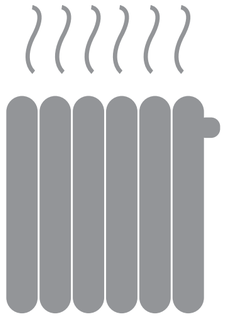

COMPLEX

DECOMPLEXIFYING

RESILIENT

WHAT IS RESILIENCE?

Designing for **durability** & **disassembly** and **maintenance**.
Passive techniques.
Designing to encourage **environmental consciousness**.
Design to **function in case of extreme events** such as storms or power outages.

COMPLEX

DECOMPLEXIFYING

RESILIENT

WHAT IS RESILIENCE?

Designing for **durability** & **disassembly** and **maintenance**.
Passive techniques.
Designing to encourage **environmental consciousness**.
Design to **function in case of extreme events** such as storms or power outages.

COMPLEX

DECOMPLEXIFYING

RESILIENT

WHAT IS RESILIENCE?

Designing for **durability** & **disassembly** and **maintenance**.
Passive techniques.
Designing to encourage **environmental consciousness**.
Design to **function in case of extreme events** such as storms or power outages.

COMPLEX

DECOMPLEXIFYING

RESILIENT

WHAT IS RESILIENCE?

Designing for **durability** & **disassembly** and **maintenance**.
Passive techniques.
Designing to encourage **environmental consciousness**.
Design to **function in case of extreme events** such as storms or power outages.

WATER TOWER

Source: warka water

WARM WATER BOTTLES

Source: https://www.yumeko.nl

WIND CATCHERS

Source: archdaily.com: What is a Traditional Windcatcher?

HEAT STORAGE BRICKS

Source: https://www.ted.com/speakers/john_o_donnell

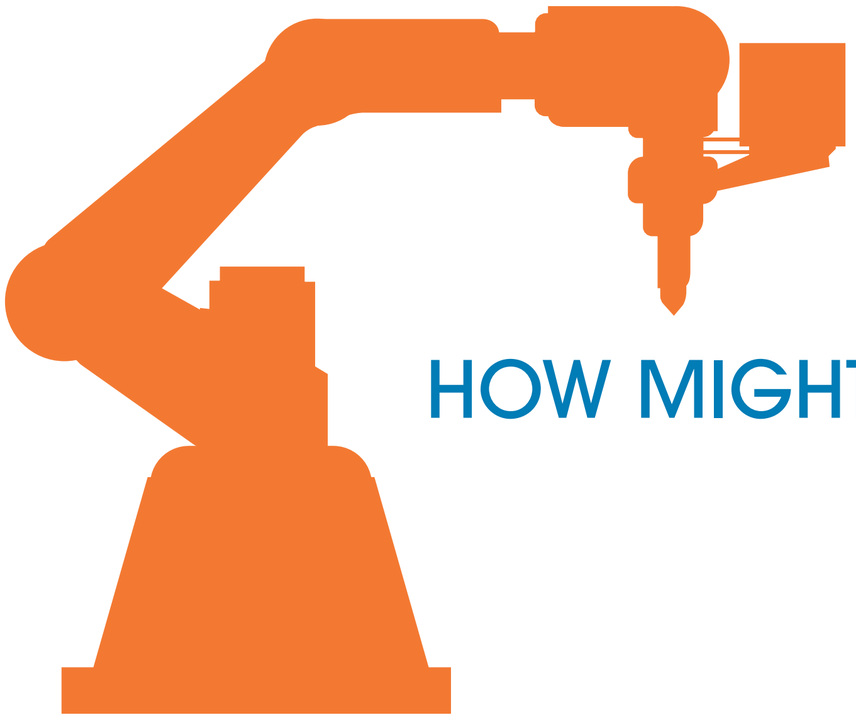

HOW MIGHT 3D PRINTING CONTRIBUTE?

ADVANTAGES

I Mass Customization
II Complexity
III Consolidated Manufacturing

ADVANTAGES

I Mass Customization
II Complexity
III Consolidated Manufacturing

ADVANTAGES

I Mass Customization
II Complexity
III Consolidated Manufacturing

SCALABILITY

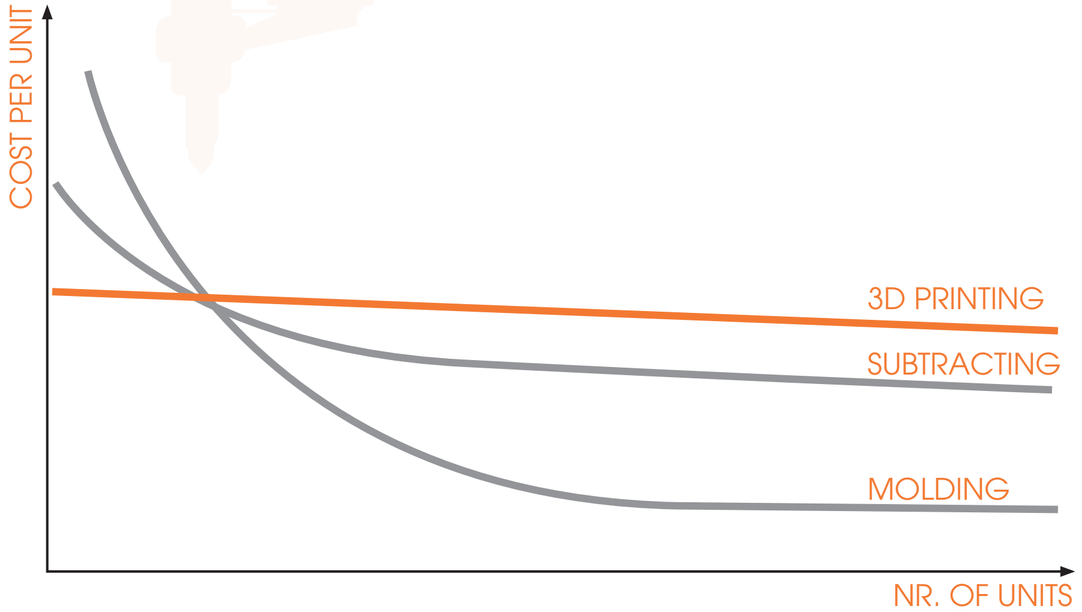

TRADITIONAL ARCHITECTURAL CONCEPTS

SOURCE: PERI 3D CONSTRUCTION

BUT PRINTED

STIFLES REAL INNOVATION.

FOR NOW, PRINTING AS SUCH NOT VIABLE.

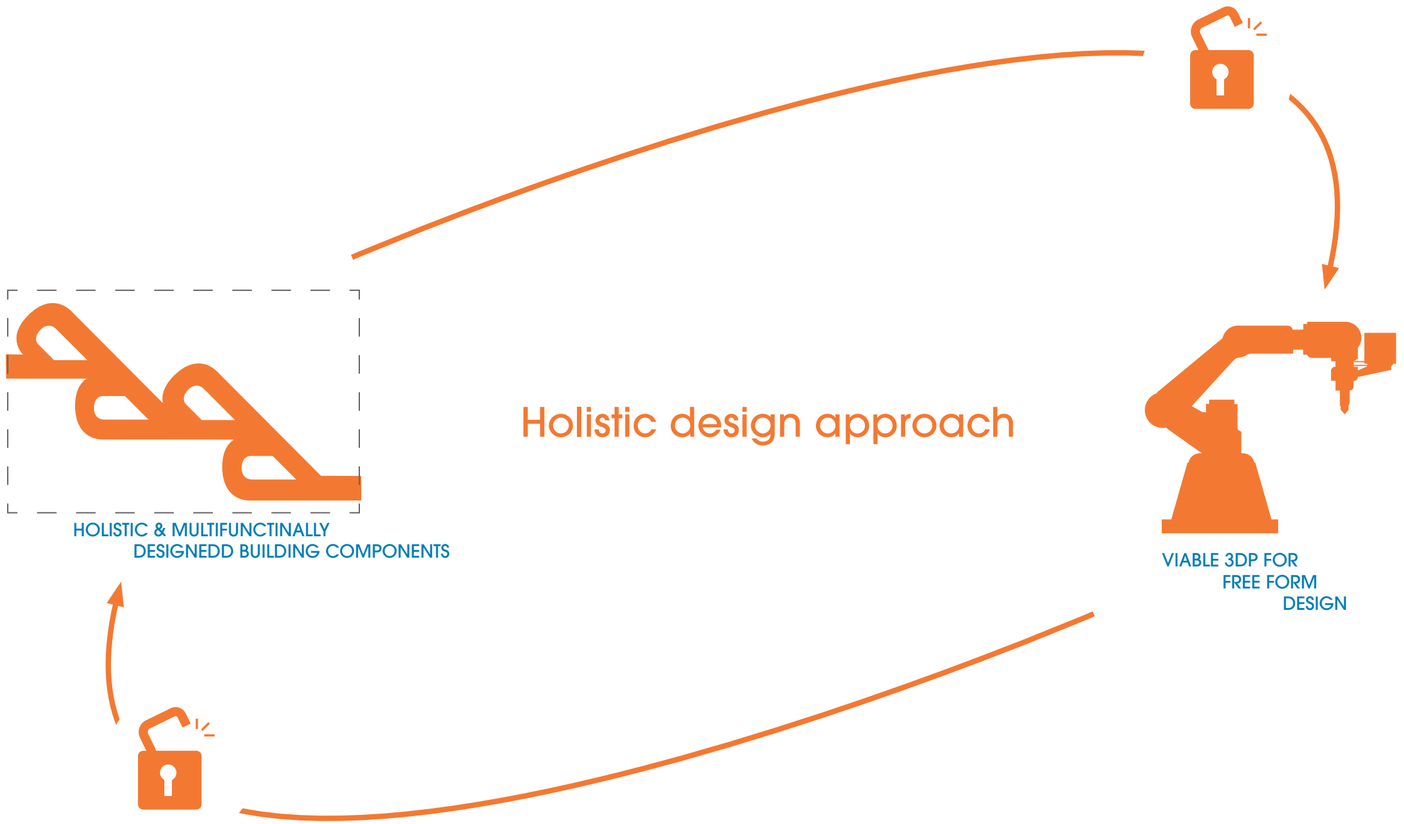
Holistic design approach
HOLISTIC & MULTIFUNCTINALLY
DESIGNEDD BUILDING COMPONENTS
VIABLE 3DP FOR
FREE FORM
DESIGN

OBJECTIVES

GENERAL OBJECTIVES

I HIGH ENERGY PERFORMANCE
II PASSIVE
III RESILIENT
IV AFFORDABLE
V SCALABLE
VI HOLLISTIC

OBJECTIVES FOR 3DP

I Mass Customization
II Inherent Complexity
III Consolidated Manufacturing

OBJECTIVES

GENERAL OBJECTIVES

I HIGH ENERGY PERFORMANCE
II PASSIVE
III RESILIENT
IV AFFORDABLE
V SCALABLE
VI HOLLISTIC

OBJECTIVES FOR 3DP

I Mass Customization
II Inherent Complexity
III Consolidated Manufacturing

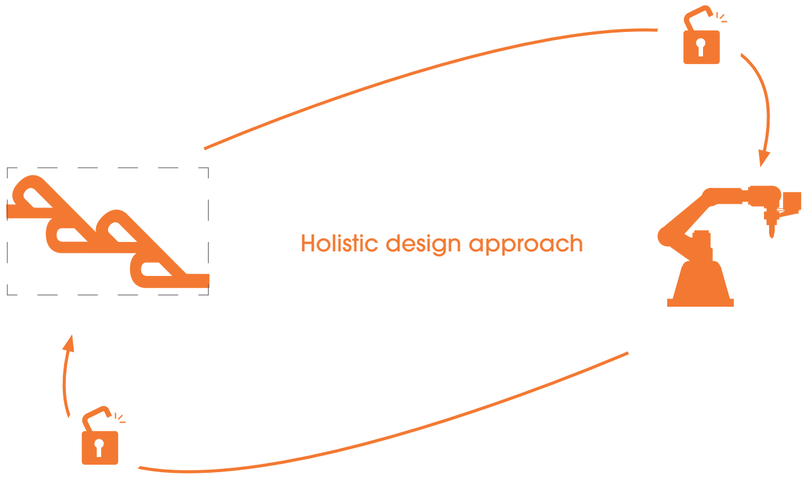

1) IDENTIFY MULTI-FACETED ISSUES

2) IDENTIFY EXISTING SOLUTIONS

3) INTEGRATE INTO HOLISTIC DESIGN

4) OPTIMIZE FOR 3D PRINTING

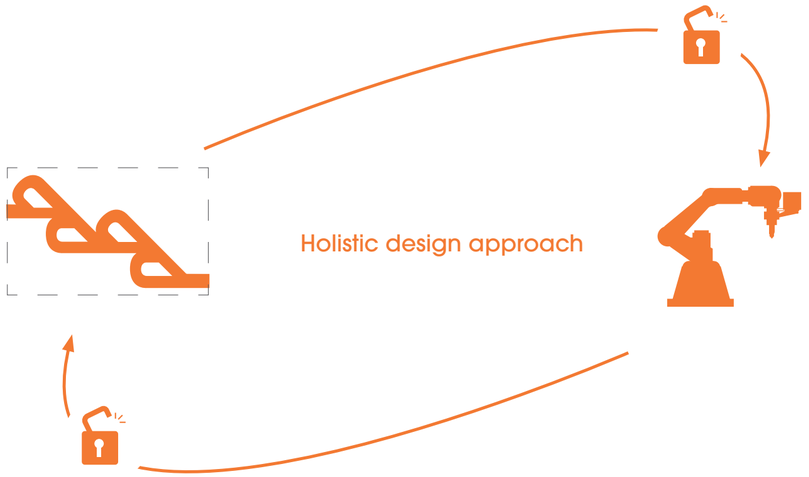

1) IDENTIFY MULTI-FACETED ISSUES

2) IDENTIFY EXISTING SOLUTIONS

3) INTEGRATE INTO HOLISTIC DESIGN

4) OPTIMIZE FOR 3D PRINTING

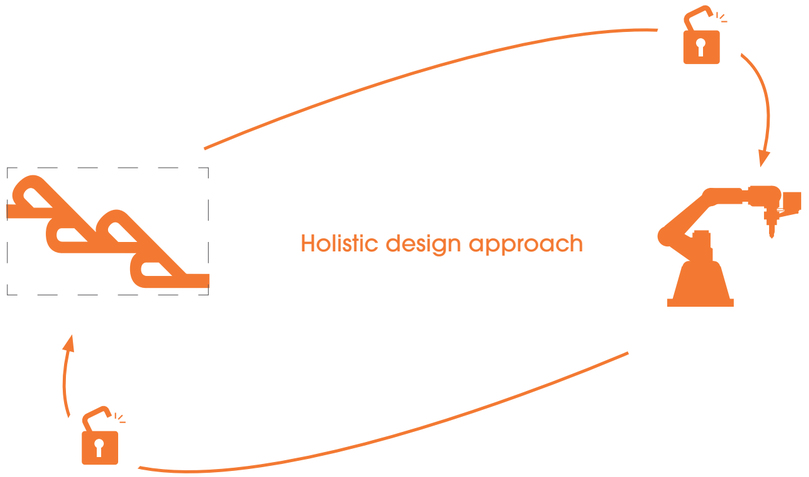

1) IDENTIFY MULTI-FACETED ISSUES

2) IDENTIFY EXISTING SOLUTIONS

3) INTEGRATE INTO HOLISTIC DESIGN

4) OPTIMIZE FOR 3D PRINTING

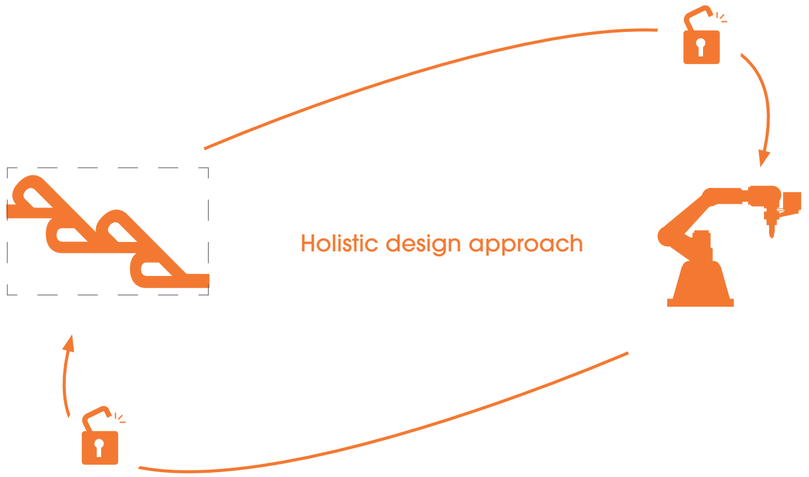

1) IDENTIFY MULTI-FACETED ISSUES

2) IDENTIFY EXISTING SOLUTIONS

3) INTEGRATE INTO HOLISTIC DESIGN

4) OPTIMIZE FOR 3D PRINTING

NATURAL

VENTILATION

1) IDENTIFY MULTI-FACETED ISSUES
2) IDENTIFY EXISTING SOLUTIONS
3) OPTIMIZE FOR 3D PRINTING
4) INTEGRATE INTO HOLISTIC DESIGN

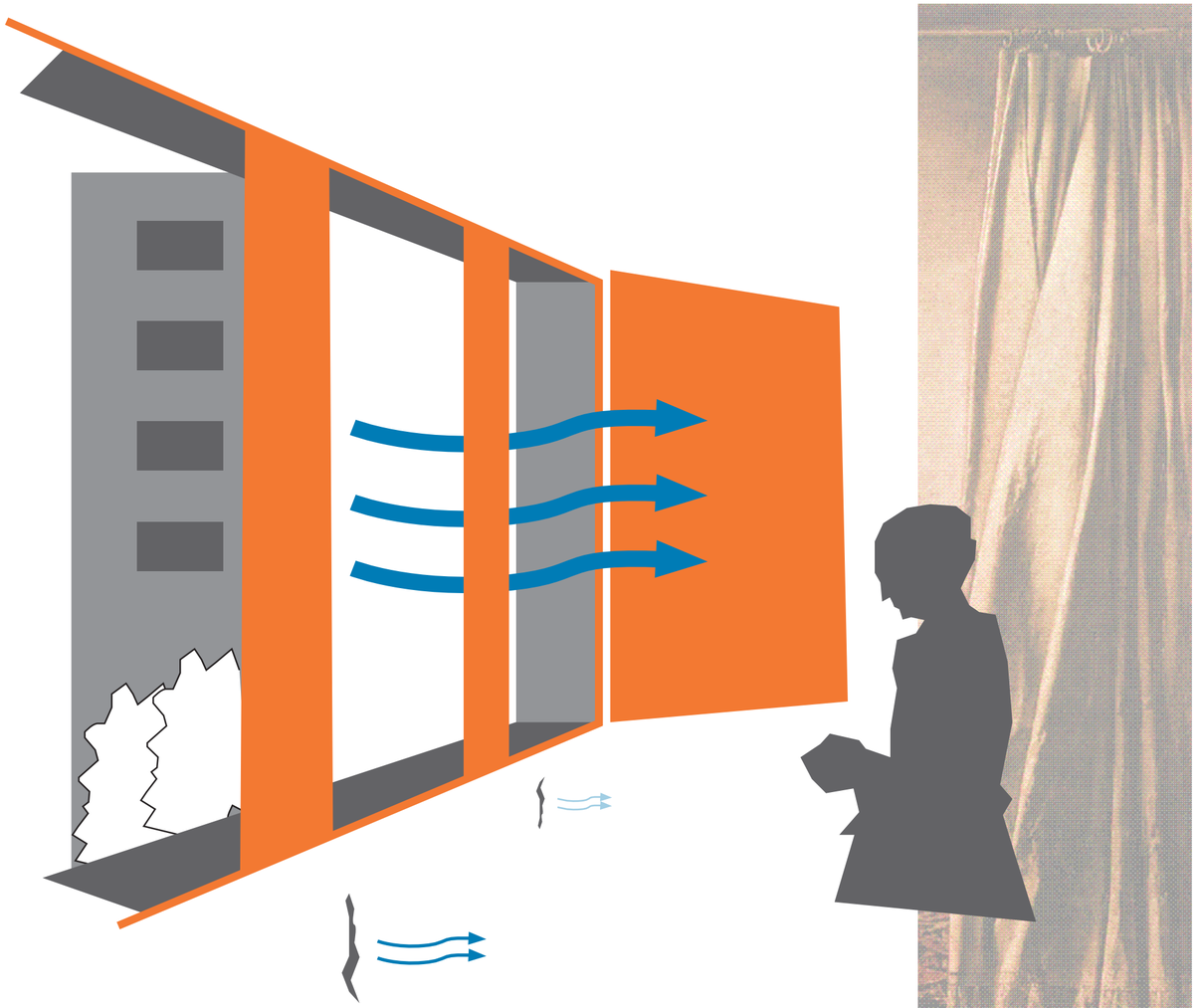

PASSIVE & RESILIENT

FRESH OUTSIDE AIR

1) IDENTIFY MULTI-FACETED ISSUES

2) IDENTIFY EXISTING SOLUTIONS

3) OPTIMIZE FOR 3D PRINTING

4) INTEGRATE INTO HOLISTIC DESIGN

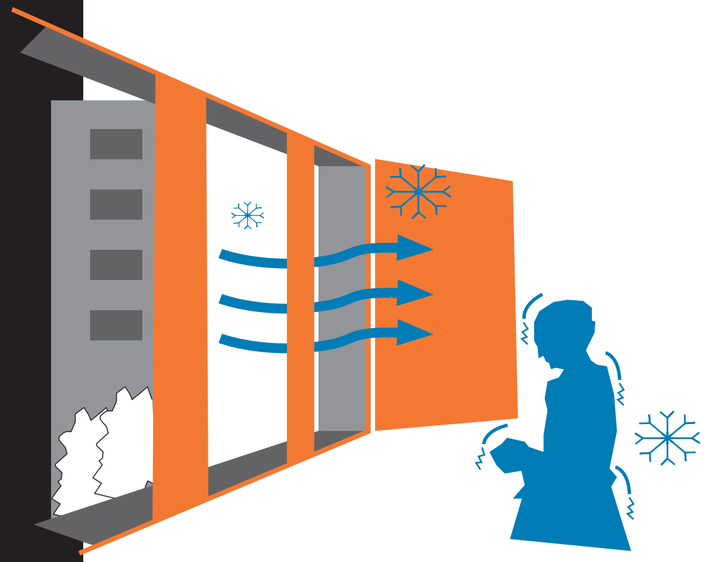

COLD DRAFTS

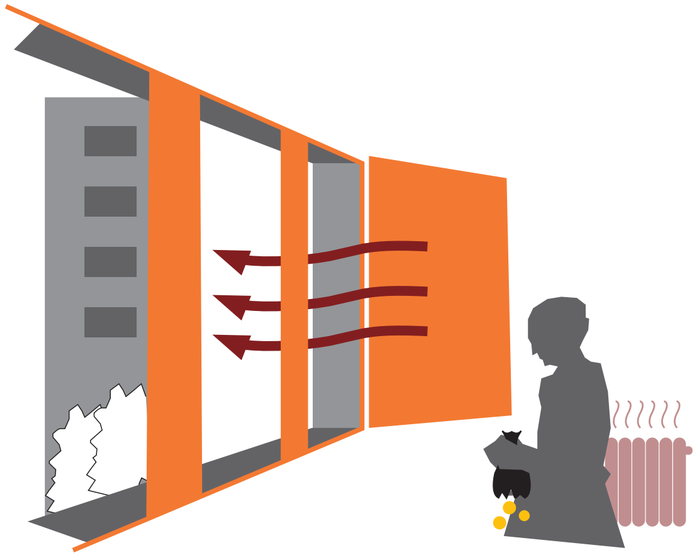

HEAT LOSS

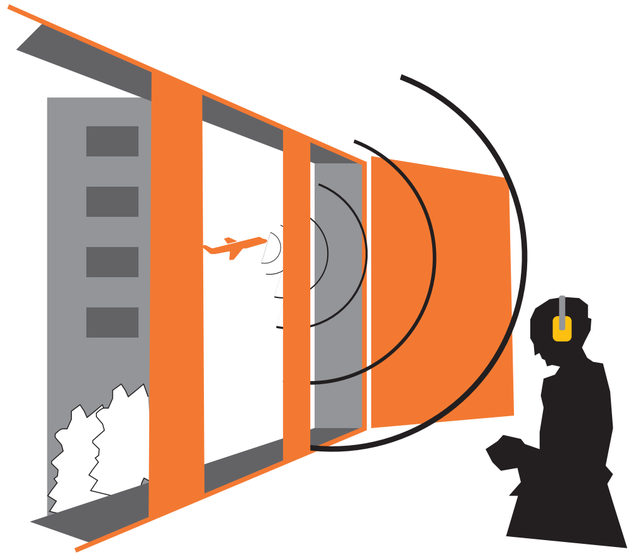

ACOUSTIC DISCOMFORT

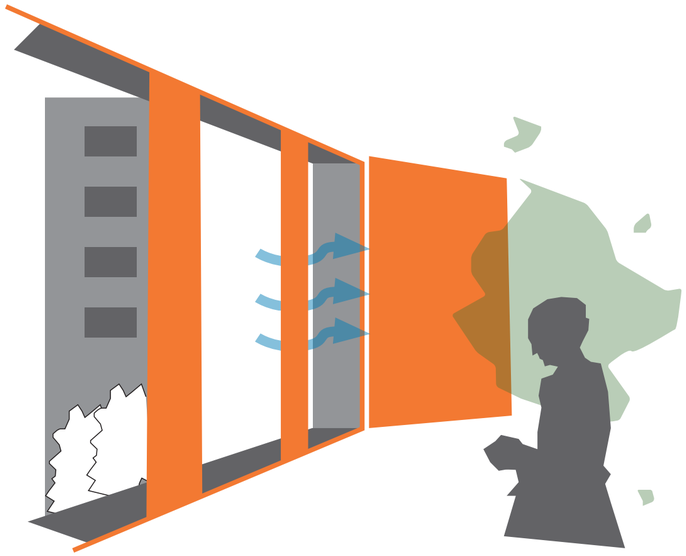

CANNOT GUARANTEE GOOD IAQ

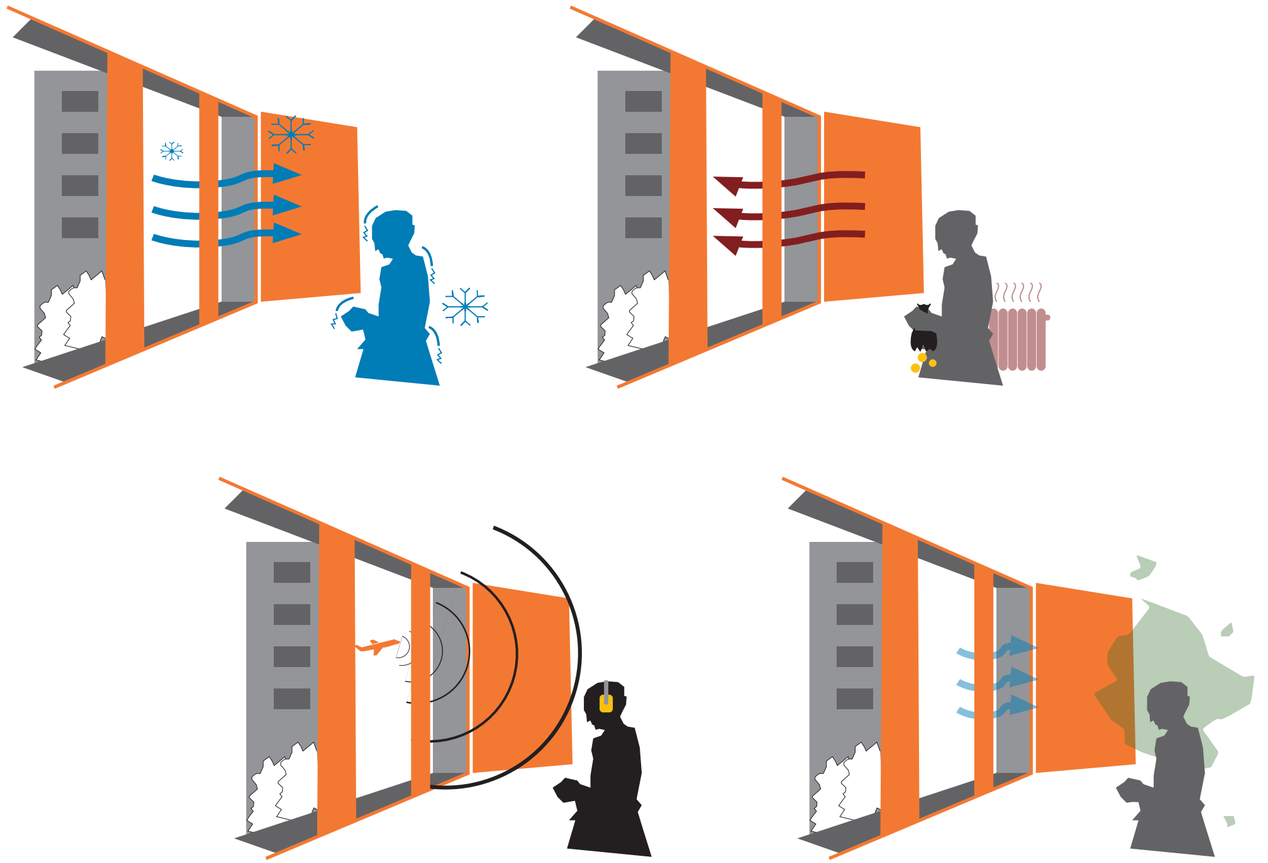

USERS HAVE TO CHOOSE BETWEEN GOOD VENTILATION AND COMFORT

1) IDENTIFY MULTI-FACETED ISSUES
2) IDENTIFY EXISTING SOLUTIONS
3) OPTIMIZE FOR 3D PRINTING
4) INTEGRATE INTO HOLISTIC DESIGN

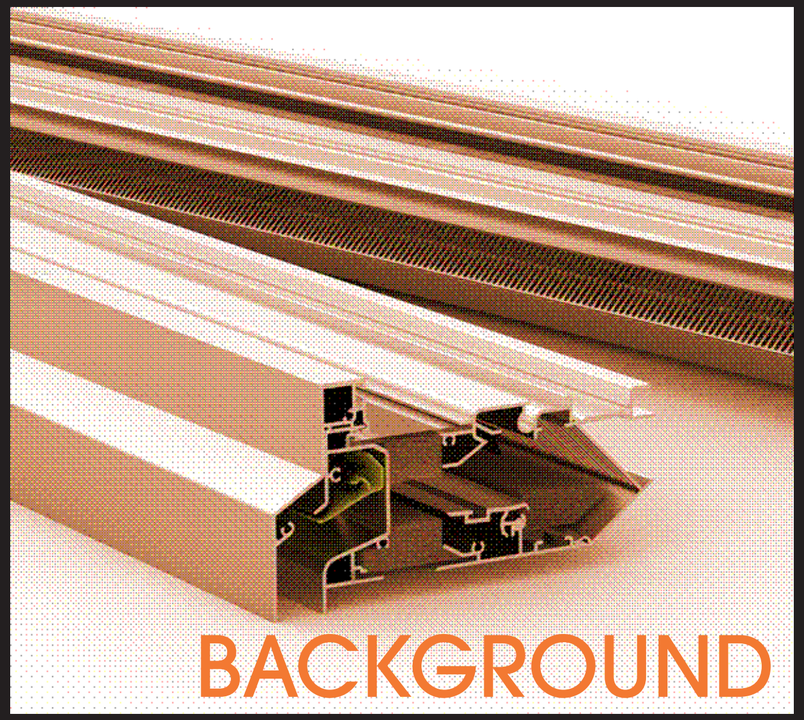

BACKGROUND

VENTILATORS

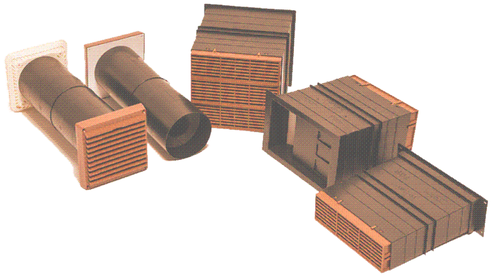

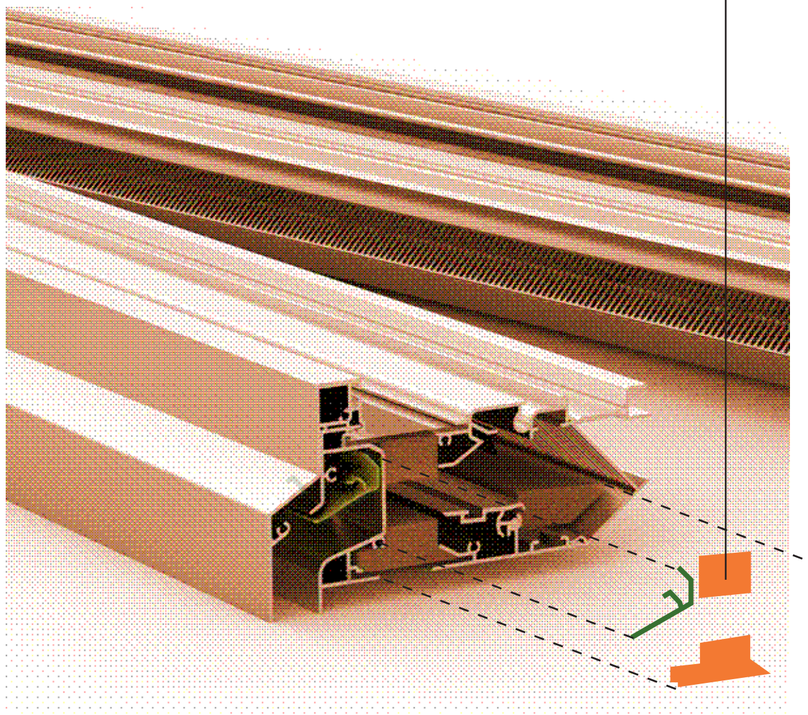

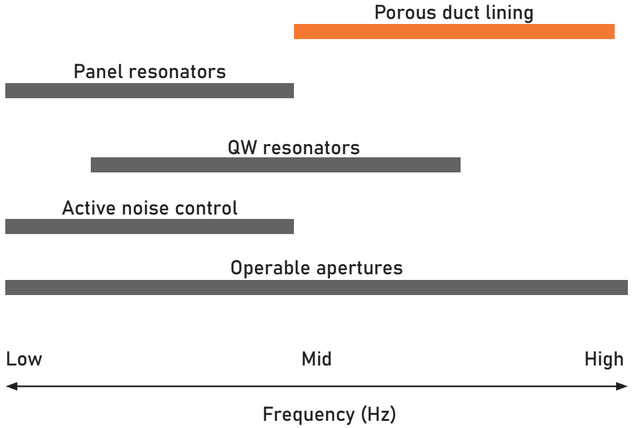

SOURCE: DE SALIS ET AL. (2002)

1) IDENTIFY MULTI-FACETED ISSUES
2) IDENTIFY EXISTING SOLUTIONS
3) OPTIMIZE FOR 3D PRINTING
4) INTEGRATE INTO HOLISTIC DESIGN

1) IDENTIFY MULTI-FACETED ISSUES

2) IDENTIFY EXISTING SOLUTIONS

3) OPTIMIZE FOR 3D PRINTING

4) INTEGRATE INTO HOLISTIC DESIGN

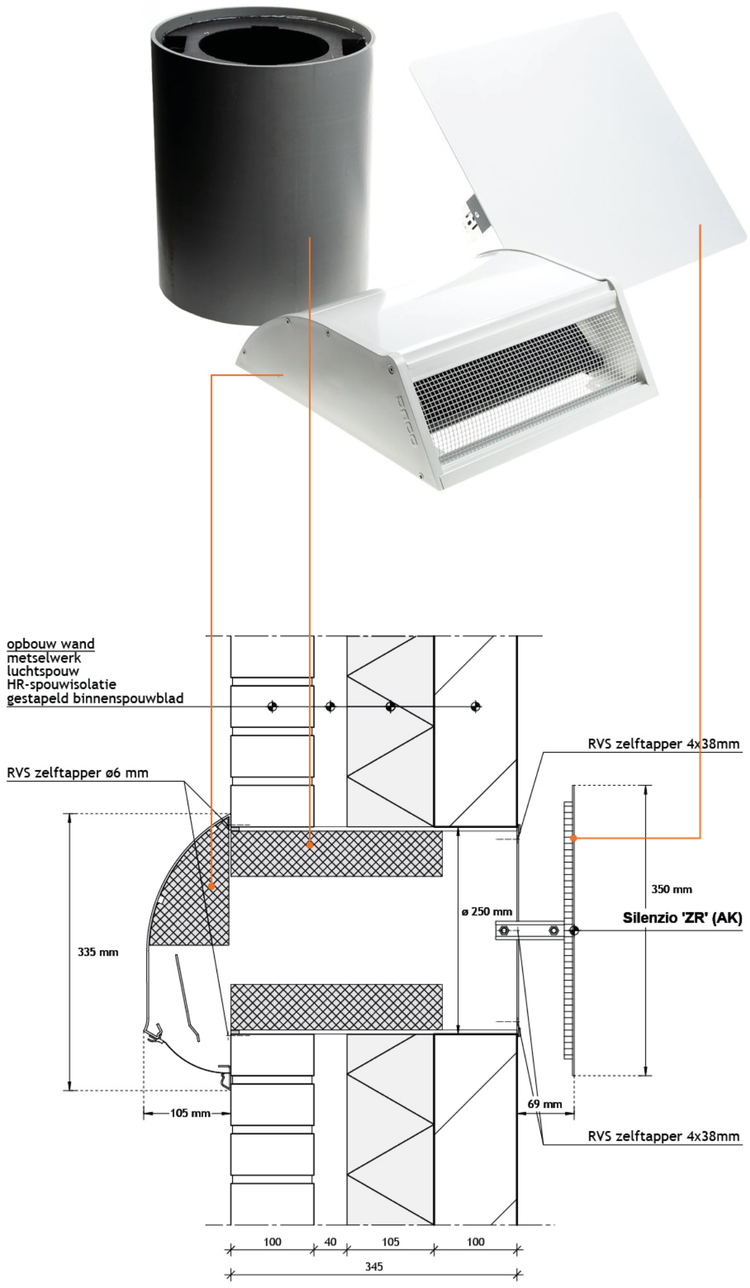

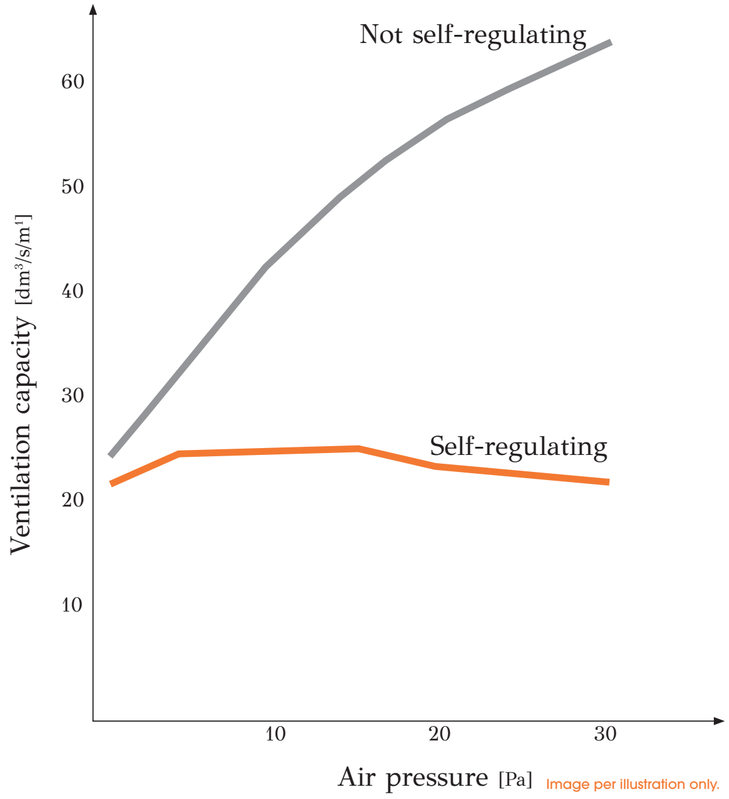

Image per illustration only.

1) IDENTIFY MULTI-FACETED ISSUES

2) IDENTIFY EXISTING SOLUTIONS

3) OPTIMIZE FOR 3D PRINTING

4) INTEGRATE INTO HOLISTIC DESIGN

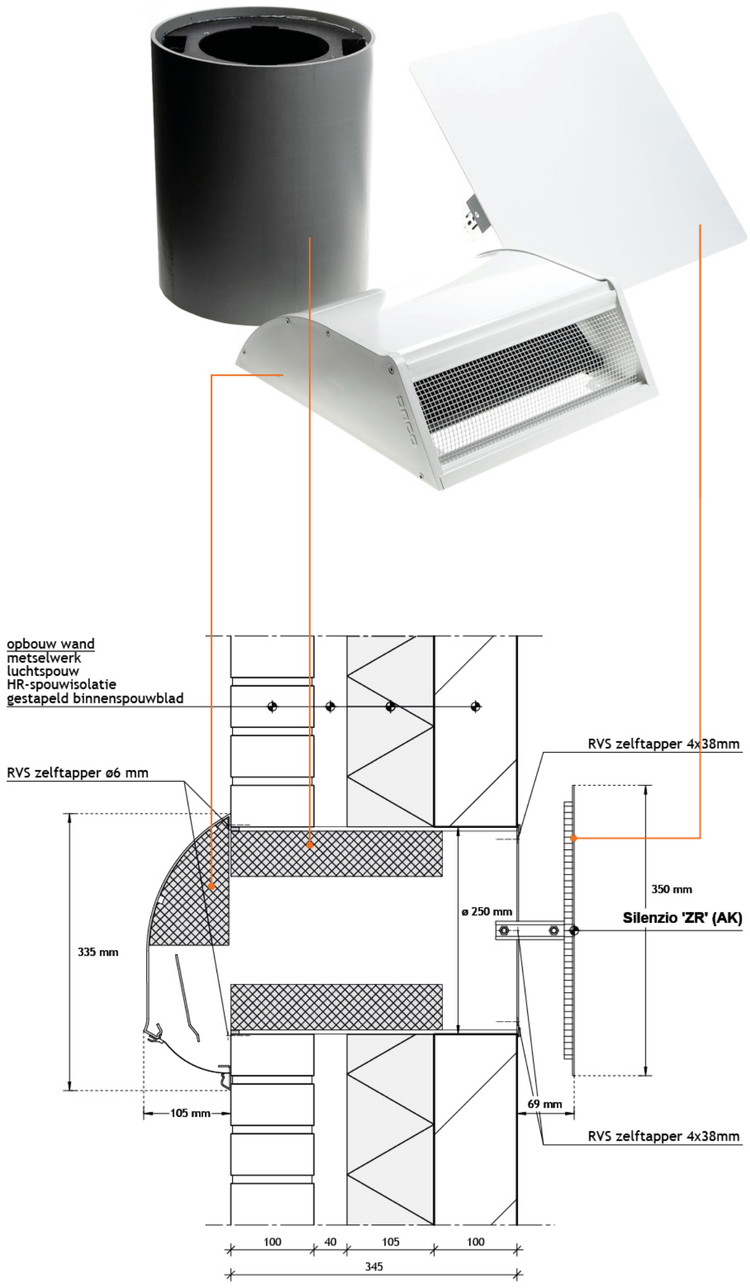

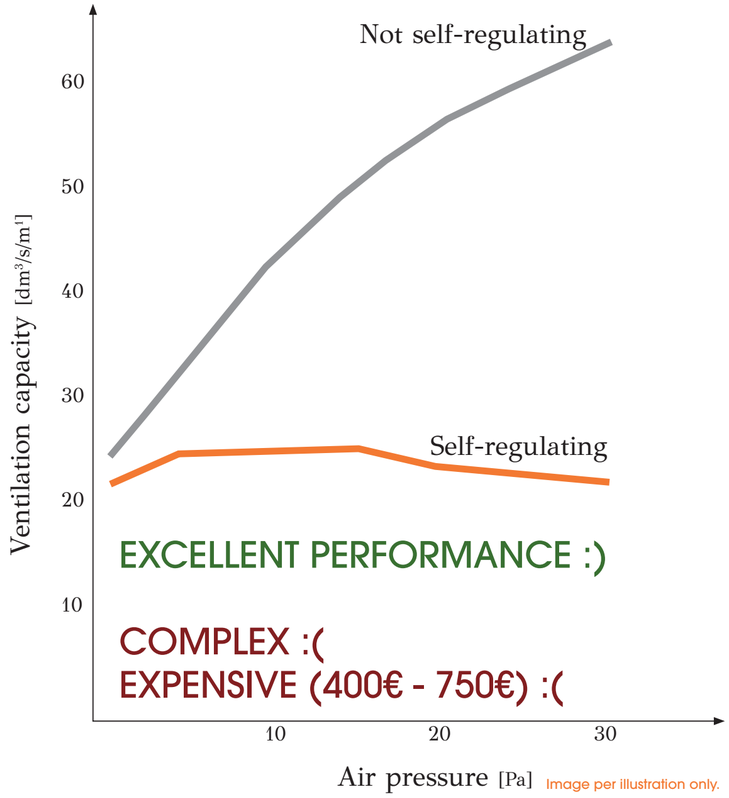

Image per illustration only.

3D PRINTING:

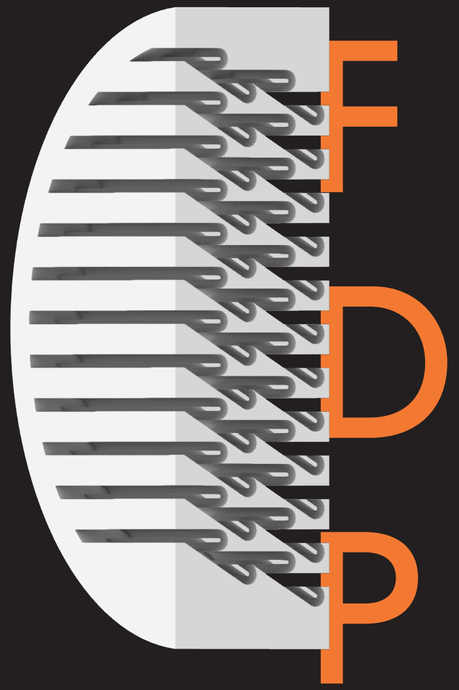

FLUID DIODE PLATE (FDP)

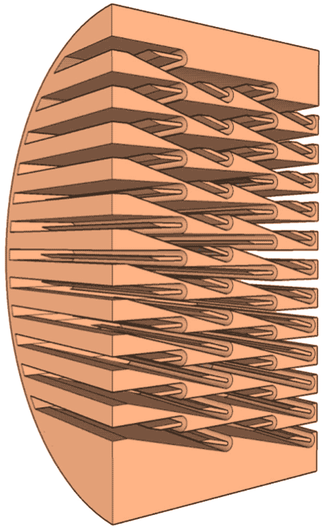

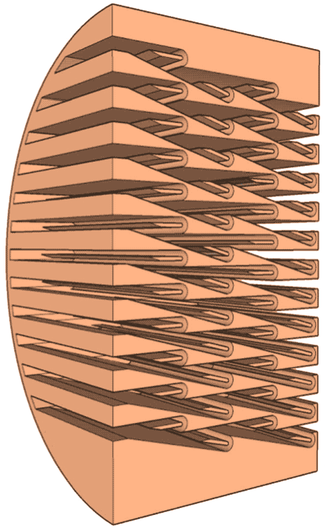

SOURCE: Cao et al. (2020)

Tesla valve (forward flow)

Tesla valve (backward flow)

1) IDENTIFY MULTI-FACETED ISSUES
2) IDENTIFY EXISTING SOLUTIONS
3) OPTIMIZE FOR 3D PRINTING
4) INTEGRATE INTO HOLISTIC DESIGN

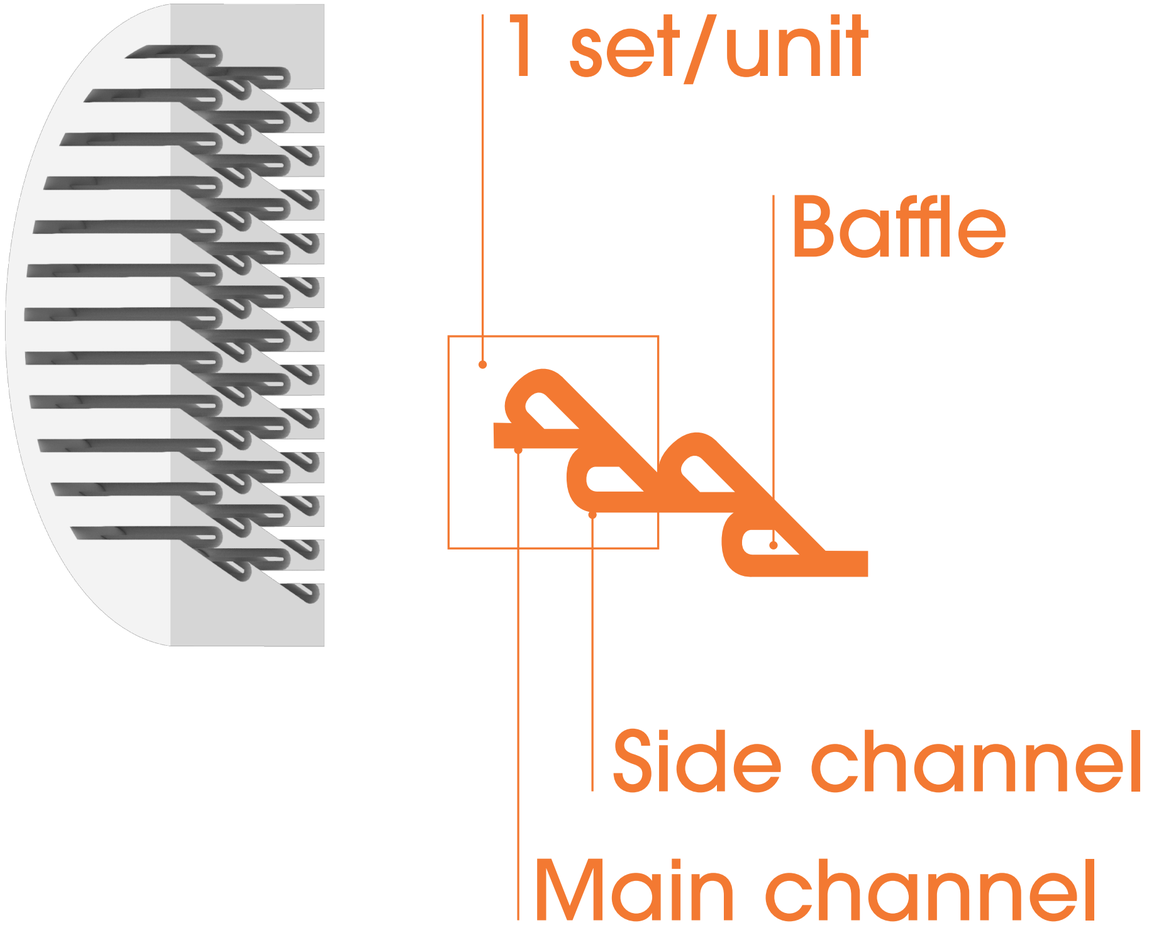
1 set/unit
Baffle
Side channel
Main channel

CAO et al.

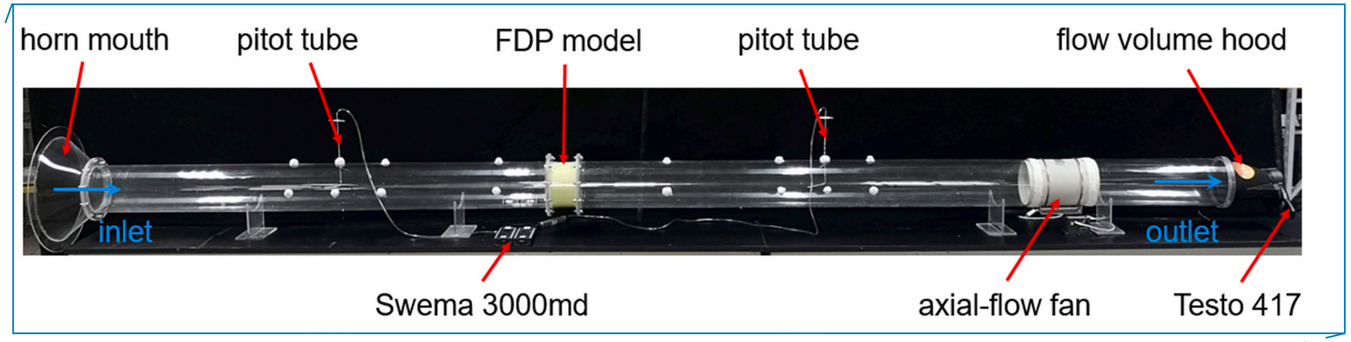

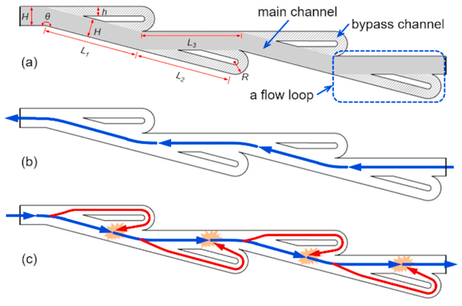

Fig. 2. Schematic of (a) Tesla structure; (b) forward flow; (c) reverse flow. The channel junctions of reverse flow are indicated by the orange stars. (For interpretation of the references to colour in this figure legend, the reader is referred to the Web version of this article.)

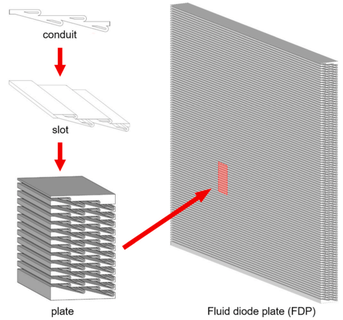

Fig. 3. Evolution of FDP.

4. Numerical methodology

4.1. Physical model and grid

The geometric model used in a numerical simulation was the same as the experimental model, as shown in Fig. 6. To validate the simulation results, 5 test points of the pressure profile were compared with experimental results for the same case. The mesh in the FDP was locally refined. To verify the independence of the grid, three different grid configurations were used in the numerical simulation, which were coarse (1.84 million), medium (2.98 million), and fine (3.72 million).

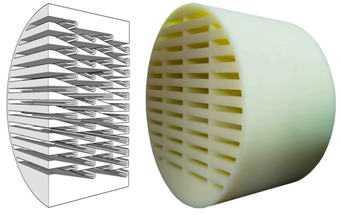

Fig. 4. Appearance and internal section structure of FDP used in experiment (reverse side in front).

4.2. Computational fluid dynamics (CFD) modeling

In this study, ANSYS Fluent is used is used to solve governing equations of fluid dynamics. The governing equation used in the numerical simulation can be expressed in the following general form:

$$\frac{\partial}{\partial t}(\rho\varphi) + div(\rho\vec{u}\varphi) = \mathrm{div}(\Gamma_\varphi grad\varphi) + S_\varphi \quad (1)$$

where ϕ represents the flow variables (velocity, enthalpy, turbulence parameters, and mass fraction), ρ is the air density, $\vec{u}$ is the velocity vector, Γ_ϕ is the diffusion coefficient, and S_ϕ is the source term. Five commonly used turbulence models were used to simulate the flow characteristics: the *k-ε* models (including the standard *k-ε* model [34], RNG *k-ε* model [35], and Realizable *k-ε* model [36]), SST *k-ω* model [37], and Reynolds stress model (RSM) [38]. The semi-implicit method for the pressure-linked equations-consistent (SIMPLEC) algorithm [39] was employed. A second-order upwind scheme was adopted for the momentum, turbulence energy, and rate of energy dissipation, with PRESTO! adopted for the pressure discretization [40]. The convergence of the simulation could be determined based upon whether the residuals of the governing equations were less than 10^{-3}, and all the monitored

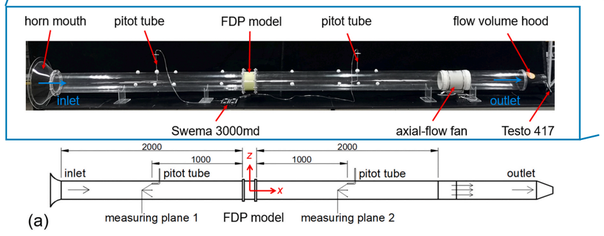

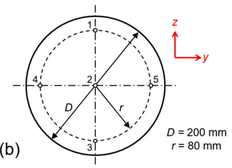

Fig. 5. Experimental setup of FDP and measurement points.

Table 1
Measuring scope and accuracy values of measurement instruments.

Measuring Instrument	Items	Range	Accuracy	Resolution
Swema 3000MD	Pressure	−300 to +1500 Pa	0.3 Pa	0.1 Pa
Testo 417	Velocity	0.3–20 m/s	0.1 m/s	0.01 m/s

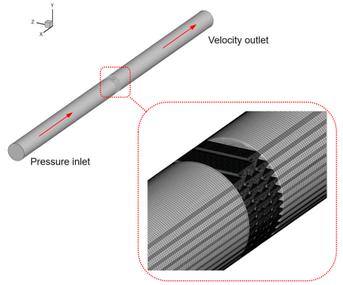

Fig. 6. Geometric model and detail of the refined mesh of numerical simulation.

variables were stable between two iterations.

4.3. Boundary conditions

The finite volume method was used to calculate the CFD and transform the differential equations into discrete equations. For near wall treatment no-slip wall boundary conditions with enhanced wall function (EWF) were applied. The experimental channel was considered a confined space envelope with a defined solid-wall boundary. According to the experiment setup, the air inlet opening was taken as a pressure inlet, and the air outlet opening was taken as a velocity outlet.

4.4. Case settings

The flow pressure losses of the FDP are closely related to its parameters. In this study, the flow characteristics of the FDP and the variation of the pressure losses under different flow velocities were first studied, and then the influences of different factors, including the flow loop number, channel ratio, and porosity, on the pressure losses of the forward and reverse flows were studied. Two evaluation indices, the pressure loss ratio (F_{FDP}) [41] and minor loss coefficient (ζ) [42], were used to evaluate the flow pressure losses of the FDP. These two evaluation indices are often used in different fields, where F_{FDP} is mostly used in research on louvers, and ζ is mostly used in research on pressure losses such as those of pipes.

To study the effect of the size relationship between the bypass channel and the main channel on the flow pressure losses, channel ratio η is defined as follows:

$$\eta = \frac{h}{H} \quad (2)$$

where *h* is the height of the bypass channel, and *H* is the height of the main channel.

Meanwhile, to study the influence of the porosity of the FDP on the flow pressure losses, porosity α is defined as follows:

$$\alpha = \frac{s}{S} \quad (3)$$

where *s* is the area of the channel openings of the FDP, and *S* is the total area of the FDP.

When the pressure on the front side of the FDP is P_1, the pressure on the backside is P_2. The pressure difference of F_{FDP} in the forward direction is ΔP_f and the pressure difference of F_{FDP} in the reverse direction is ΔP_r. Pressure loss ratio F_{FDP} can be expressed as follows:

$$F_{FDP} = \frac{\Delta P_r}{\Delta P_f} = \frac{P_{r1} - P_{r2}}{P_{f1} - P_{f2}} \quad (4)$$

The minor loss coefficient, ζ, is usually given as a ratio of head loss $h_m = p/(\rho g)$ through the plate to velocity head $v^2/(2g)$, as shown in Eq. (5):

$$\zeta = \frac{h_m}{\frac{v^2}{2g}} = \frac{\Delta P}{\frac{1}{2}\rho v^2} = \frac{P_1 - P_2}{\frac{1}{2}\rho v^2} \quad (5)$$

The Reynolds numbers (*Re*) of the supply air in the main channel are listed in Table 2. They could be calculated as follows:

$$Re = \frac{HV_c}{\nu} \quad (6)$$

where ν is the kinematic viscosity of the air, $v_c = v/\alpha$ is the air velocity in the main channel, and inflow velocity *v* is the mean velocity of air at inlet of the duct.

The detail variables and geometric dimensions of the numerical simulation cases are listed in Tables 2 and 3, respectively.

5. Validation

5.1. Grid independence validation

Different grid arrangements with minimum grid sizes of 1.84 million (coarse grid), 2.98 million (medium grid), and 3.72 million (fine grid) were compared to test the grid independence of the numerical solutions. The pressure profiles at the vertical centerline of measuring plane 2 are compared with the experimental data in Fig. 7. Obviously, the data of the coarse grid deviates from that of the medium grid and fine grid, but the results for the fine grid and medium grid are similar, which are fairly

Table 2
Simulated variables.

Case No.	Inflow velocity *v* (m/s)	Flow loop number *N*	Channel ratio *η*	Porosity %	*Re*
1–1	**0.2**	4	0.53	0.33	205
1–2	**0.44**	4	0.53	0.33	450
1–3	**0.88**	4	0.53	0.33	901
1–4	**1.32**	4	0.53	0.33	1351
1–5	**1.76**	4	0.53	0.33	1802
1–6	**2**	4	0.53	0.33	2048
1–7	**3**	4	0.53	0.33	3071
1–8	**4**	4	0.53	0.33	4095
1–9	**6**	4	0.53	0.33	6143
1–10	**8**	4	0.53	0.33	8190
1–11	**10**	4	0.53	0.33	10,237
1–12	**12**	4	0.53	0.33	12,285
1–13	**15**	4	0.53	0.33	15,356
1–14	**18**	4	0.53	0.33	18,428
2–1	1.76	**1**	0.53	0.33	1802
2–2	1.76	**2**	0.53	0.33	1802
2–3	1.76	**6**	0.53	0.33	1802
3–1	1.76	4	**0.33**	0.33	1802
3–2	1.76	4	**0.63**	0.33	1802
4–1	1.76	4	0.53	**0.35**	1699
4–2	1.76	4	0.53	**0.29**	2050

Table 3
Geometric dimensions.

Parameter (mm)	Case No.					
	1–1–1–14	2–1–2–3	3–1	3–2	4–1	4–2
h	2.66	2.66	1.65	3.15	1.87	4.00
H	5.00				3.50	7.50
L_1	26.77				18.78	40.16
L_2	25.25				17.63	37.84
L_3	26.12				18.29	39.19
R	6.93	6.93	3.47	3.47	2.43	5.20
θ	195°					

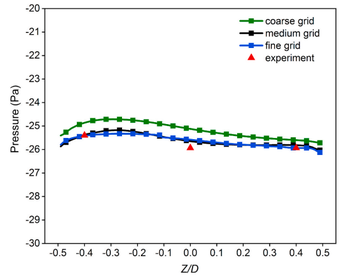

Fig. 7. Pressure profiles at vertical centerline of measuring plane 2 with three different grids.

close to the experimental data. This indicates that the resolution of the medium grid was adequate to guarantee the computational precision. Considering the simulation accuracy and computational time cost, the medium grid was adopted in the work discussed in the following sections of this paper.

5.2. Turbulence model validation

Before conducting a flow pressure loss simulation, five turbulence models were tested for validation. In this study, measurements were made at five points in measuring plane 2 for reverse flow with $V = 0.88$ m/s (as seen in Fig. 5), and then the average measured value at each point was compared with the simulation results with the different turbulence models. As shown in Fig. 8, the k-ω SST model agreed better with the experimental data than the other turbulence models, with a deviation of only 0.70% from the experimental results. Therefore, the *k-ω* SST model was adopted for the numerical simulations in this study.

To further validate the accuracy of the numerical settings in different cases, the values for pressure difference ΔP of reverse flow under different flow rates on measuring plane 2 were compared, as shown in Fig. 9. This indicated that the simulated results agreed well with the experimental data in each case, which showed that the present CFD methods performed well in the prediction of the airflow in this study.

6. Results and discussion

6.1. Effect of inflow velocity on flow pressure loss

The effects of different inflow velocities on the check effect of the

CAO et al.

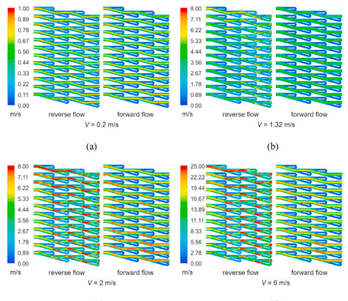

Fig. 10. Velocity distributions for different air velocities: (a) Case 1-1 $V = 0.2$ m/s ($Re = 205$), (b) Case 1-4 $V = 1.32$ m/s ($Re = 1351$), (c) Case 1-6 $V = 2$ m/s ($Re = 2048$), and (d) Case 1-9 $V = 6$ m/s ($Re = 6143$).

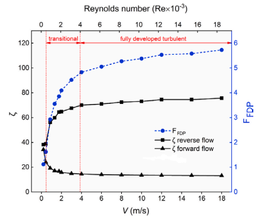

Fig. 11. Minor loss coefficients and pressure loss ratios in two flow directions for different flow loop numbers.

Fig. 13 shows the values for the minor loss coefficient and the pressure loss ratio in the two flow directions for different flow loop numbers. It indicates that when the flow loop number is relatively small ($N = 1$, $N = 2$), the minor loss coefficients of the forward flow and reverse flow are almost the same. However, when the flow loop number increases, the minor loss coefficient of the forward flow remains stable, while the minor loss coefficient of the reverse flow increases rapidly and nonlinearly, reaching 5.90 times that of the forward flow when $N = 6$. Therefore, when using the FDP, a larger flow loop number will provide a better backflow prevention effect.

6.3. *Effect of channel ratio on flow pressure loss*

It is easy to understand that most of the flow pressure loss to reverse flow in the FDP comes from the flow in the bypass channel. Therefore, the channel ratio η of the FDP should be considered. First, when η was too small, the flow into the bypass channel was insufficient to improve the reverse flow pressure loss. When η was too large, the flow through the main channel was relatively small, which led to an insufficient overall flow through the FDP. Therefore, the η value for the FDP should be in a suitable range to not only ensure the flow rate in the forward direction but also ensure the resistance to reverse flow.

Fig. 14 shows the velocity distributions of the FDP with $\eta = 0.33$, $\eta = 0.53$, and $\eta = 0.63$, which were established by changing the diameter of the bypass channel (Case 3-1, Case 1-5, and Case 3-2, $Re = 1802$). It shows that the forward flow was almost independent of the channel ratio, with almost no fluid flow in the bypass channel. However, for the reverse flow, when η was too small (Case 3-1), the flow rate in the bypass channel was insufficient to influence the flow velocity at the intersection of the channels, which resulted in insufficient flow blockage.

Fig. 15 shows the minor loss coefficients and pressure loss ratios of the FDP for $\eta = 0.33$, $\eta = 0.53$, and $\eta = 0.63$. It indicates that with an increase in the channel ratio, the resistance to the forward flow remains almost the same at a low level. In contrast, the resistance to reverse flow rapidly increases. For $\eta = 0.63$ in Case 3-2, the resistance to reverse flow could reach 4.68 times that of forward flow. In all three cases, the diameter of the main channel was the same, with only the diameter of the bypass channel changed. Therefore, to increase the check effect of the FDP without affecting the forward flow, it would be necessary to increase the diameter of the bypass channel as much as possible while maintaining the diameter of the main channel.

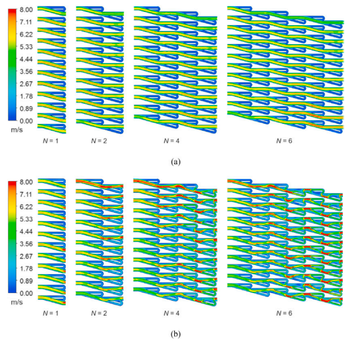

Fig. 12. Velocity distributions of forward flow (a) and reverse flow (b) with different flow loop numbers of FDP for $Re = 1802$ (Case 2-1, Case 2-2, Case 1-5, and Case 2-3).

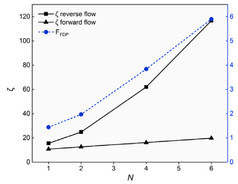

Fig. 13. Minor loss coefficients and pressure loss ratios in two flow directions for different flow loop numbers for $Re = 1802$ (Case 2-1, Case 2-2, Case 1-5, and Case 2-3).

6.4. *Effect of porosity on flow pressure loss*

An important index for evaluating the FDP was its porosity, which was directly related to the flow rate and flow pressure loss. This section shows how the size and density of the channels were adjusted to compare three types of FDPs with different porosities under the condition of making full use of the same circular area (Case 4-1 $Re = 1699$, Case 1-5 $Re = 1802$, and Case 4-2 $Re = 2050$). Fig. 16 (a) shows the velocity contours of the forward flow. It shows that with a decrease in the porosity, the diameter of each main flow channel increases, and the flow velocity in each main flow channel increases. For the reverse flow in Fig. 16 (b), it shows that the turbulence in the FDP with low porosity is more intense. There were two possible reasons for this situation. First, the flow velocity in the FDP with low porosity was larger. As discussed in section 6.1, an increase in the flow velocity will lead to an increase in the flow pressure loss. Second, because more fluid enters the bypass channel for the FDP with low porosity, according to section 6.3, there will be a more obvious flow blockage.

Fig. 17 shows the minor loss coefficients and pressure loss ratios of a FDP and thin orifice plate for $\alpha = 0.35$, $\alpha = 0.33$, and $\alpha = 0.29$. The thin orifice plate (the thickness was almost negligible) was used to compare the influence of the frictional resistance of the FDP on its forward flow. First, it was found that with an increase in porosity, the minor loss coefficients of both the forward flow and reverse flow decreased. The flow pressure loss of the reverse flow decreased more obviously, while that of the forward flow remained at a relatively low value. For the case of $\alpha = 0.29$, the pressure loss ratio reached 3.78, which meant the pressure loss to the reverse flow could reach 3.78 times that of the forward flow. Therefore, for the same height, a FDP with a large diameter and small porosity would be better at preventing backflow. Second, when the porosity of the FDP increased from 0.29 to 0.35, the thickness of the FDP had to be significantly increased to ensure the same number of flow loop. However, it was found that the minor loss coefficients of the FDP's

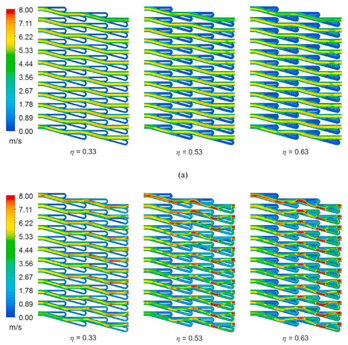

Fig. 14. Velocity distributions of forward flow (a) and reverse flow (b) with different channel ratios of FDP for $Re = 1802$ (Case 3-1, Case 1-5, and Case 3-2).

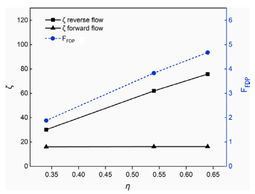

Fig. 15. Minor loss coefficients and pressure loss ratios in two flow directions with different channel ratios of FDP for $Re = 1802$.

forward flow, $\zeta_{forward\ flow}$, and that of the orifice plate with the same porosity, ζ_0, were similar in different cases. In other words, the frictional resistance of the FDP had little effect on the increase in the total flow pressure loss.

7. Limitations and prospects

Starting with the small-scale laboratory experiments, this study had numerous limitations. Although the laboratory experiments and numerical simulations could isolate the impact of uncontrollable factors, field tests in real ventilation systems are still needed to further explore the influence of the complex flow profiles. First, the influences of the inflow direction and unsteady inflow velocity on the flow pressure losses of the FDP were not considered in this study, which is very common in practical ventilation engineering. Second, in order to adapt to the characteristics of the Tesla mechanism stack of the FDP used in this study, the Tesla structure had to be optimized. However, this Tesla structure still has the potential for further optimization. The optimization principles included a larger porosity, more channels under the premise of minimum thickness, and a larger channel ratio. Finally, when the FDP is used in engineering, problems that are more practical need to be considered. These include how to avoid internal deposition and how to determine the appropriate FDP specifications based on the inflow velocity. These problems will be further studied in future research.

8. Conclusions

Based on the principle of the Tesla structure, this paper presented a novel FDP with no moving parts for use in the ventilation field. The ability of the FDP to prevent backflow was tested experimentally in a wind tunnel and validated by CFD simulations. Meanwhile, the pressure loss ratio (F_{FDP}) and minor loss coefficient (ζ) were used to evaluate the flow pressure losses of the FDP. The following conclusions can be drawn.

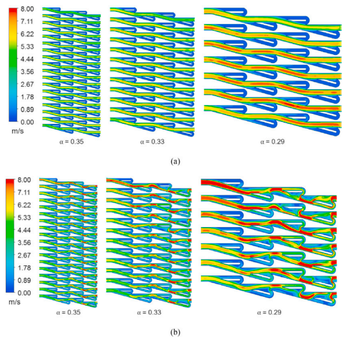

Fig. 16. Velocity distributions of forward flow (a) and reverse flow (b) with different porosities of FDP (Case 4-1 $Re = 1699$, Case 1-5 $Re = 1802$, and Case 4-2 $Re = 2050$).

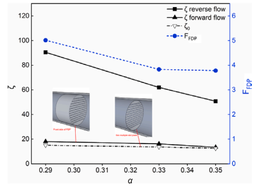

Fig. 17. Minor loss coefficients and pressure loss ratios in two flow directions for different porosities of FDP (Case 4-1 $Re = 1699$, Case 1-5 $Re = 1802$, and Case 4-2 $Re = 2050$).

(1) The reverse flow resistance of the FDP was much higher than the forward flow resistance, which have the potential to prevent or restrain the backflow in building ventilation systems, especially when the airflow velocity is high.
(2) The inflow velocity, number of flow loop, channel ratio, and porosity were the four important factors affecting the flow characteristics of the FDP. When the inflow velocity was increased, the pressure loss ratio first increased and then tended to become stable. A larger flow loop number or channel diameter resulted in a more significant reflux prevention effect. The check effect of a FDP with a larger porosity was better than that of a FDP with a small porosity. Within the scope of this study, the pressure loss ratio could reach 3.78–5.90.
(3) The minor loss coefficient of the FDP forward flow was generally less than 20, which was close to that of a thin orifice plate with the same porosity. This means that the FDP did not cause excessive additional flow resistance to the system for the forward flow.

Declaration of competing interest

The authors declare that they have no known competing financial interests or personal relationships that could have appeared to influence the work reported in this paper.

Acknowledgement

This research was financially sponsored by the National Key Research & Development Program (Grant No. 2018YFC0705300), the National Science Foundation of China (No. 51908446), the project funded by the China Postdoctoral Science Foundation (No. 2019M653573), and Shaanxi Provincial Key Science and Technology Innovation Team (Grant No. 2017KCT-14).

HU et al.

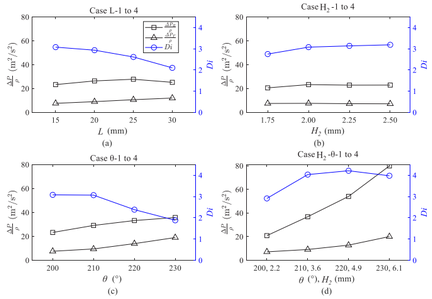

Fig. 4. Results of the parametric study for all cases, including the pressure loss of the forward flow ($\Delta P_f/\rho$) and reverse flow ($\Delta P_R/\rho$) and the pressure loss ratio (*Di*) of the shape. (a) Case L-1 to 4: *Di* vs. Main channel length (*L*) with fixed H_2 and θ; (b) Case H_2-1 to 4: *Di* vs. Bypass channel height (H_2) with fixed *L* and θ; (c) Case θ-1 to 4: *Di* vs. Shape angle (θ) with fixed *L* and H_2; (d) Case H_2-θ-1 to 4: *Di* vs. Different shape angles (θ) and corresponding bypass heights (H_2) with fixed *L* and H_3.

increase simultaneously. The maximum pressure loss ratio is 4.2 for a shape angle of 220° with a bypass height of 4.9 mm (Case H_2-0-3), followed by 4.1 for a shape angle of 210° with a bypass height of 3.6 mm (Case H_2-0-2). As the slope angle and height of the bypass channel increase, the pressure loss for reverse flow increases steeply and becomes more significant. In contrast, the pressure loss for forward flow gradually increases. However, when the slope angle exceeds 220° and the bypass channel height exceeds 4.9 mm, the pressure loss for forward flow grows at a faster rate, leading to a decrease in the pressure loss ratio.

Additionally, we observed the airflows in Cases H_2-0-1 to 4. Fig. 5 presents the velocity magnitude distribution of airflow for each case in the Tesla valve.

For reverse flow, all four cases exhibit the characteristic behavior in a Tesla valve: the collision between the airflow in the main channel and the backward airflow from the bypass channel. However, the characteristic slightly differs in Cases H_2-0-3 and 4. Especially in the second unit in Cases H_2-0-4, many small vortices occurred in the main and bypass channels, as indicated by the red arrow in the figure. Most air passes the valve through the bypass channel rather than the main channel. This change in the flow path and those small vortices contribute to the large pressure loss.

In contrast, no vortexes are generated in the main channel for forward flow, and the flow predominantly passes through the main channel in all four cases. However, vortexes are formed in the bypass channels. In the first bypass (i.e., the one on the right), a small portion of airflow enters with low velocity, and some of it forms a vortex, while the rest flows out and rejoins the airflow in the main channel. The airflow's direction aligns with the main channel, and its low speed has a small impact on the main channel's airflow. In the second bypass channel (i.e., the one on the left), a portion of the airflow from the main channel reverses direction and enters the bypass channel in the upper section close to the valve outlet. After passing through the bypass channel, it rejoins the upstream flow in the main channel. Increasing θ and H_2 leads to a stronger airflow passing through the bypass channel, contributing to the increase in the pressure loss.

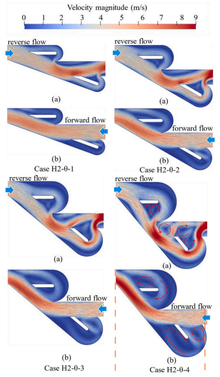

Fig. 5. Velocity magnitude distribution of reverse (a) and forward flow (b) for Case H_2-0-1 to 4.

3.6. Selection of optimal shape in the current study

Among all the studied cases, the largest pressure loss ratio *Di* values are found in Cases H_2-0-2 and H_2-0-3, which are 4.1 and 4.2, respectively. While these values are almost the same, the pressure loss in the installing direction of FDP, without using a piecewise function, as the discontinuity in a piecewise function may bring instability in the numerical iterations in CFD.

The samples of *Re* and ζ for both Shape 1 and Shape 2 are shown in Fig. 10. According to the pattern in these samples, the five-parameter logistic function is considered suitable to be the fitting function Equation (6), which can be written as

$$\zeta = f(Re) = A + \frac{D-A}{(1+\exp(B \bullet Re + C))^S}, \tag{8}$$

where *A*, *B*, *C*, *D*, and *S* are the five function parameters. Accordingly, the performance curve can be given by

$$\zeta(V) = f\left(\frac{\alpha H_1}{\nu} V\right) = A + \frac{D-A}{\left(1+\exp\left(B \bullet \frac{\alpha H_1}{\nu} \bullet V + C\right)\right)^S}, \tag{9}$$

where $\alpha = 0.3125$, $H_1 = 5$ mm, and $\nu = 1.5 \times 10^{-5}$ m^2/s are all known constants, and *V* is the only independent variable in the function.

After the fitting, the five function parameters are listed in Table 2, and the fitting functions are plotted in Fig. 10. The R^2 values are 0.9948 and 0.9906 for Shapes 1 and 2, respectively, indicating good fits. Notice that these curves exhibit nonlinear characteristics when the Reynolds number is low but converge to a certain value when the Reynolds number is high, and clear inflection points can be observed in Fig. 10. These functions of performance curves will be used as a load term representing the FDP at the openings in Section 5 when simulating the natural ventilation in a building without resolving the airflows inside the FDPs.

5. Building ventilation with FDPs

In this section, the FDPs are installed in an isolated building model, and their performance in building ventilation is investigated. The FDPs with Shapes 1 and 2 under both forward and reverse flow conditions are considered, and the volumetric ventilation rates are compared.

5.1. Building geometry and case setting

The building geometry is set according to the wind tunnel experiment of Tominaga and Blocken [46], a classical building model used in many later studies [47–51]. In this study, the size of the building model is scaled up by a factor of 20 to restore the model from the reduced scale to the full scale.

The geometry and dimensions are shown in Fig. 11. This building model has two symmetric openings located at the center of opposite walls. The wind direction is normal to the openings, and the airflow is expected to produce significant cross-ventilation in the building. In the other two cases, an FDP is installed at the opening on the windward wall. When the forward direction of FDP is along the approaching wind, this scenario is called the "forward direction"; when the forward direction of FDP is opposite to the approaching wind, it is called the "reverse direction."

A total number of 17 simulations were conducted in this study, as listed in Table 3. They include the cases with or without the FDPs, those under forward or reverse direction if an FDP is involved, and cases with different reference wind speeds at the building rooftop (U_{ref}). Notably, in the case without an FDP, the indoor ventilation rate should be proportional to the reference wind speed when the outdoor Reynolds number ($=HU_{ref}/\nu$) is sufficiently large; however, it is no longer proportional when an FDP is installed because the pressure loss brought by FDP is not proportional to the dynamic pressure, shown in Equation (9). Therefore, only one reference wind speed is considered in the case with no FDP, while multiple reference wind speeds are considered when an FDP is installed at the opening.

5.2. Simulation setup

The simulation domain and mesh grid are shown in Fig. 12. The building was located in a wind tunnel with a width of 48 m (=12*W* or 15*H*) and a height of 19.2 m (=6*H*). The inlet and outlet of the tunnel are 24 m (=7.5*H*) and 40 m(=12.5*H*), respectively, from the center of the building. The domain size adhered to the recommendations outlined in the guidelines by Tominaga et al. [52].

The indoor and outdoor meshes are generated in two closed spaces. In general, the minimum cell size was 0.04 m (=*W*/100), which was adjacent to the building walls and openings, and the maximum was 0.64 m, which was adjacent to the tunnel walls. The total cell number is approximately 4.3 million.

The interfaces of indoor and outdoor meshes are walls and openings (see Fig. 12 (b)). The surfaces of both sides are set as the wall boundaries using the wall function of Spalding's law [43]. The same wall boundary setting is imposed on the floor. For openings with no FDP, the two surfaces of both sides are connected by a "cyclic" boundary condition in OpenFOAM, which directly maps all the physical quantities on the two sides of the interfaces.

When an FDP is installed at Opening 1, a self-made boundary condition is compiled and used in OpenFOAM. All other physical quantities are directly mapped as the cyclic boundary except for the pressure in this boundary condition. A pressure drop (i.e., ΔP, the outdoor-indoor pressure loss at the opening interface) is specified according to Equations (5) and (9), which is determined by the normal speed of the flow through that interface (i.e., the quantity *V* in Eqs. (5) and (9)). The normal speed is positive when the forward direction of FDP is along the approaching wind and negative when the forward direction of FDP is opposite to the approaching wind. In a CFD solver, the pressure drop and normal speed are coupled and solved iteratively. For example, according

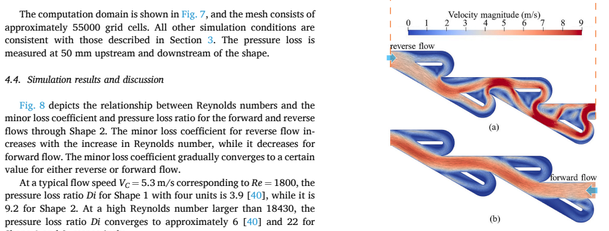

Fig. 9. Velocity magnitude distribution for reverse (a) and forward flow (b) at *Re* = 1800 for the four-unit shape of Case H_2-0-2.

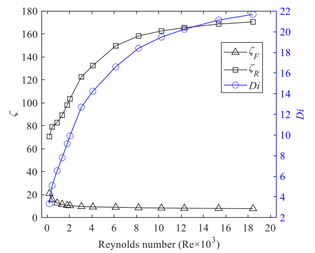

Fig. 8. Minor loss coefficients ζ and pressure loss ratio *Di* in the forward and reverse flow directions of Shape 2 for different Reynolds numbers.

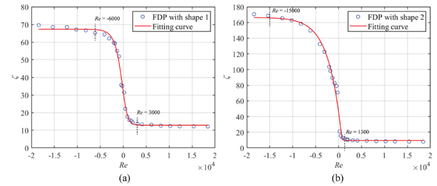

Fig. 10. Curve fitting results of the minor loss coefficients for FDP with Shape 1 (a) and Shape 2 (b) under forward and reverse flows at different Reynolds numbers.

Table 2
Function parameters in the logistic function Equation (8).

Parameters	*A*	*B*	*C*	*D*	*S*
FDP with Shape 1	62.25	-1.93×10^3	0.399	12.91	0.4654
FDP with Shape 2	149.1	-8.46×10^3	6.314	8.17	0.0416

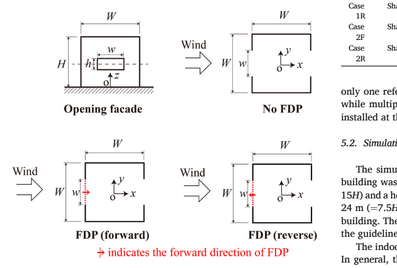

Fig. 11. Building geometry with the full-scale dimensions of $W = 4$ m, $H = 3.2$ m, $w = 1.84$ m, and $h = 0.72$ m. The FDP can consist of either Shape 1 or 2.

Table 3
Simulation cases.

Cases	Shape of FDP	Direction of FDP	Reference wind speed at the building rooftop U_{ref} (m/s)
Case 0	No FDP	–	4
Case 1F	Shape 1	Forward	2, 4, 6, or 8
Case 1R	Shape 1	Reverse	2, 4, 6, or 8
Case 2F	Shape 2	Forward	2, 4, 6, or 8
Case 2R	Shape 2	Reverse	2, 4, 6, or 8

1) OPTIMIZED VALVE PERFORMANCE

2) SIMULATED PERFORMANCE OF BEST PERFORMING VALVE

3) MATHEMATICALLY DEFINED THE PERFORMANCE

Fig. 4. Results of the parametric study for all cases, including the pressure loss of the forward flow ($\Delta P_F/\rho$) and reverse flow ($\Delta P_R/\rho$) and the pressure loss ratio (Di) of the shape. (a) Case L-1 to 4: Di vs. Main channel length (L) with fixed H_2 and θ; (b) Case H_2-1 to 4: Di vs. Bypass channel height (H_2) with fixed L and θ; (c) Case θ-1 to 4: Di vs. Shape angle (θ) with fixed L and H_2; (d) Case H_2-θ-1 to 4: Di vs. Different shape angles (θ) and corresponding bypass heights (H_2) with fixed L and H_2.

increase simultaneously. The maximum pressure loss ratio is 4.2 for a shape angle of 220° with a bypass height of 4.9 mm (Case H_2-0-3), followed by 4.1 for a shape angle of 210° with a bypass height of 3.6 mm (Case H_2-0-2). As the slope angle and height of the bypass channel increase, the pressure loss for reverse flow increases steeply and becomes more significant. In contrast, the pressure loss for forward flow gradually increases. However, when the slope angle exceeds 220° and the bypass channel height exceeds 4.9 mm, the pressure loss for forward flow grows at a faster rate, leading to a decrease in the pressure loss ratio.

Additionally, we observed the airflows in Cases H_2-0-1 to 4. Fig. 5 presents the velocity magnitude distribution of airflow for each case in the Tesla valve.

For reverse flow, all four cases exhibit the characteristic behavior in a Tesla valve: the collision between the airflow in the main channel and the backward airflow from the bypass channel. However, the characteristic slightly differs in Cases H_2-0-3 and 4. Especially in the second unit in Cases H_2-0-4, many small vortices occurred in the main and bypass channels, as indicated by the red arrow in the figure. Most air passes the valve through the bypass channel rather than the main channel. This change in the flow path and those small vortices contribute to the large pressure loss.

In contrast, no vortexes are generated in the main channel for forward flow, and the flow predominantly passes through the main channel in all four cases. However, vortexes are formed in the bypass channels. In the first bypass (i.e., the one on the right), a small portion of airflow enters with low velocity, and some of it forms a vortex, while the rest flows out and rejoins the airflow in the main channel. The airflow's direction aligns with the main channel, and its low speed has a small impact on the main channel's airflow. In the second bypass channel (i.e., the one on the left), a portion of the airflow from the main channel reverses direction and enters the bypass channel in the upper section close to the valve outlet. After passing through the bypass channel, it rejoins the upstream flow in the main channel. Increasing θ and H_2 leads to a stronger airflow passing through the bypass channel, contributing to the increase in the pressure loss.

Fig. 5. Velocity magnitude distribution of reverse (a) and forward flow (b) for Case H_2-0-1 to 4.

3.6. Selection of optimal shape in the current study

Among all the studied cases, the largest pressure loss ratio Di values are found in Cases H_2-0-2 and H_2-0-3, which are 4.1 and 4.2, respectively. While these values are almost the same, the pressure loss in the

The computation domain is shown in Fig. 7, and the mesh consists of approximately 55000 grid cells. All other simulation conditions are consistent with those described in Section 3. The pressure loss is measured at 50 mm upstream and downstream of the shape.

4.4. Simulation results and discussion

Fig. 8 depicts the relationship between Reynolds numbers and the minor loss coefficient and pressure loss ratio for the forward and reverse flows through Shape 2. The minor loss coefficient for reverse flow increases with the increase in Reynolds number, while it decreases for forward flow. The minor loss coefficient gradually converges to a certain value for either reverse or forward flow.

At a typical flow speed $V_0 = 5.3$ m/s corresponding to $Re = 1800$, the pressure loss ratio Di for Shape 1 with four units is 3.9 [40], while it is 9.2 for Shape 2. At a high Reynolds number larger than 18430, the pressure loss ratio Di converges to approximately 6 [40] and 22 for Shape 1 and 2, respectively.

Fig. 9 presents the velocity magnitude distribution of forward and reverse flows passing through Shape 2 at $Re = 1800$. In the case of reverse flow, the introduction of two additional units to Shape 2 leads to enhanced flow resistance. Clear flow collisions can be observed at the junctures of the main and bypass channels in the first to third units. Because of the collisions, the flow gradually becomes uneven in the pipe with an increasing maximum flow speed over the units. Especially in the fourth unit, prominent and well-defined vortices appear within the main channel and the main flow path changes to the bypass channel. All the above collisions and vortices increase the flow resistance. The forward flow is similar to that in the two-unit Tesla valve in Fig. 5. The flow in the first unit (on the right) shows a similar vortex in the bypass channel, like a cavity flow. In the other three units, a small plume of airflow separates from the main flow path, enters the bypass channel, and rejoins the flow in the main channel upstream.

4.5. Fitting of the performance curves

For convenience of further application, the samples for both forward and reverse flow are fit into one function. In the case of reverse flow, V and Re are set to negative, and in the case of forward flow, V and Re are set to positive. In further simulations for the building ventilation (Section 5), this allows the code to conveniently calculate the pressure loss according to the direction of the normal velocity on FDP and the

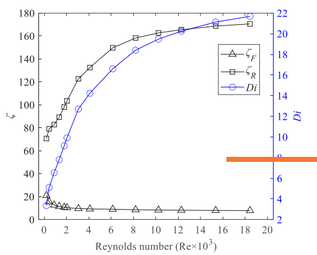

Fig. 8. Minor loss coefficients ζ and pressure loss ratio Di in the forward and reverse flow directions of Shape 2 for different Reynolds numbers.

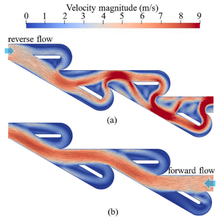

Fig. 9. Velocity magnitude distribution for reverse (a) and forward flow (b) at $Re = 1800$ for the four-unit shape of Case H_2-θ-2.

installing direction of FDP, without using a piecewise function, as the discontinuity in a piecewise function may bring instability in the numerical iterations in CFD.

The samples of Re and ζ for both Shape 1 and Shape 2 are shown in Fig. 10. According to the pattern in these samples, the five-parameter logistic function is considered suitable to be the fitting function Equation (6), which can be written as

$$\zeta = f(Re) = A + \frac{D - A}{(1 + \exp(B * Re + C))^S}, \tag{8}$$

where A, B, C, D, and S are the five function parameters. Accordingly, the performance curve can be given by

$$\zeta(V) = f\left(\frac{\alpha H_1}{\varepsilon} V\right) = A + \frac{D - A}{\left(1 + \exp\left(B * \frac{\alpha H_1}{\varepsilon} * V + C\right)\right)^S}, \tag{9}$$

where $\alpha = 0.3125$, $H_1 = 5$ mm, and $\varepsilon = 1.5 \times 10^{-5}$ m^2/s are all known constants, and V is the only independent variable in the function.

After the fitting, the five function parameters are listed in Table 2, and the fitting functions are plotted in Fig. 10. The R^2 values are 0.9948 and 0.9906 for Shapes 1 and 2, respectively, indicating good fits. Notice that these curves exhibit nonlinear characteristics when the Reynolds number is low but converge to a certain value when the Reynolds number is high, and clear inflection points can be observed in Fig. 10. These functions of performance curves will be used as a load term representing the FDP at the openings in Section 5 when simulating the natural ventilation in a building without resolving the airflows inside the FDPs.

5. Building ventilation with FDPs

In this section, the FDPs are installed in an isolated building model, and their performance in building ventilation is investigated. The FDPs with Shapes 1 and 2 under both forward and reverse flow conditions are

5.1. Building geometry and case setting

The building geometry is set according to the wind tunnel experiment of Tominaga and Blocken [46], a classical building model used in many later studies [47–51]. In this study, the size of the building model is scaled up by a factor of 20 to restore the model from the reduced scale to the full scale.

The geometry and dimensions are shown in Fig. 11. This building

PERFORMANCE CURVES

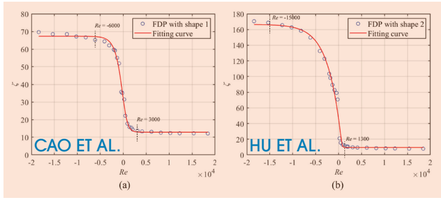

Fig. 10. Curve fitting results of the minor loss coefficients for FDP with Shape 1 (a) and Shape 2 (b) under forward and reverse flows at different Reynolds numbers.

Table 2
Function parameters in the logistic function Equation (8).

Parameters	A	B	C	D	S
FDP with Shape 1	62.25	-1.93×10^{-3}	0.399	12.91	0.4654
FDP with Shape 2	149.1	-8.46×10^{-4}	6.314	8.17	0.0416

Table 3
Simulation cases.

Cases	Shape of FDP	Direction of FDP	Reference wind speed at the building rooftop U_{ref} (m/s)
Case 0	No FDP	–	4
Case 1F	Shape 1	Forward	2, 4, 6, or 8
Case 1R	Shape 1	Reverse	2, 4, 6, or 8
Case 2F	Shape 2	Forward	2, 4, 6, or 8
Case 2R	Shape 2	Reverse	2, 4, 6, or 8

Fig. 11. Building geometry with the full-scale dimensions of $W = 4$ m, $H = 3.2$ m, $w = 1.84$ m, and $h = 0.72$ m. The FDP can consist of either Shape 1 or 2.

model has two symmetric openings located at the center of opposite walls. The wind direction is normal to the openings, and the airflow is expected to produce significant cross-ventilation in the building. In the other two cases, an FDP is installed at the opening on the windward wall. When the forward direction of FDP is along the approaching wind, this scenario is called the "forward direction"; when the forward direction of FDP is opposite to the approaching wind, it is called the "reverse direction."

A total number of 17 simulations were conducted in this study, as listed in Table 3. They include the cases with or without the FDPs, those under forward or reverse direction if an FDP is involved, and cases with different reference wind speeds at the building rooftop (U_{ref}). Notably, in the case without an FDP, the indoor ventilation rate should be proportional to the reference wind speed when the outdoor Reynolds number ($=HU_{ref}/\nu$) is sufficiently large; however, it is no longer proportional when an FDP is installed because the pressure loss brought by FDP is not proportional to the dynamic pressure, shown in Equation (9). Therefore, only one reference wind speed is considered in the case with no FDP, while multiple reference wind speeds are considered when an FDP is installed at the opening.

5.2. Simulation setup

The simulation domain and mesh grid are shown in Fig. 12. The building was located in a wind tunnel with a width of 48 m ($=12W$ or $15H$) and a height of 19.2 m ($=6H$). The inlet and outlet of the tunnel are 24 m ($=7.5H$) and 40 m($=12.5H$), respectively, from the center of the building. The domain size adhered to the recommendations outlined in the guidelines by Tominaga et al. [52].

The indoor and outdoor meshes are generated in two closed spaces. In general, the minimum cell size was 0.04 m ($=W/100$), which was adjacent to the building walls and openings, and the maximum was 0.64 m, which was adjacent to the tunnel walls. The total cell number is approximately 4.3 million.

The interfaces of indoor and outdoor meshes are walls and openings (see Fig. 12 (b)). The surfaces of both sides are set as the wall boundaries using the wall function of Spalding's law [43]. The same wall boundary setting is imposed on the floor. For openings with no FDP, the two surfaces of both sides are connected by a "cyclic" boundary condition in OpenFOAM, which directly maps all the physical quantities on the two sides of the interfaces.

When an FDP is installed at Opening 1, a self-made boundary condition is compiled and used in OpenFOAM. All other physical quantities are directly mapped as the cyclic boundary except for the pressure in this boundary condition. A pressure drop (i.e., ΔP, the outdoor-indoor pressure loss at the opening interface) is specified according to Equations (5) and (9), which is determined by the normal speed of the flow through that interface (i.e., the quantity V in Eqs. (5) and (9)). The normal speed is positive when the forward direction of FDP is along the approaching wind and negative when the forward direction of FDP is opposite to the approaching wind. In a CFD solver, the pressure drop and normal speed are coupled and solved iteratively. For example, according

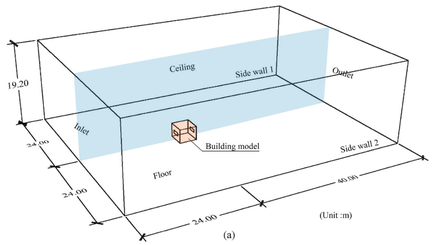

(a)

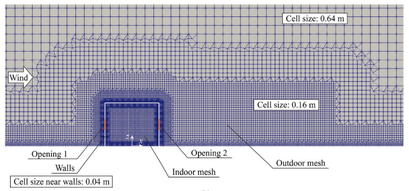

(b)

Fig. 12. Simulation domain (a) and mesh gird (b).

to Equation (9), the corresponding pressure drop is large when the initial normal speed is large. Then, when the Poisson equation is solved, the too-large pressure drop will lower the normal speed passing to the next iteration. After many iterations, the solver will find a balanced solution that satisfies the performance curve in Equation (9) and the Navier-Stocks equations for the flows on the two sides.

The boundary conditions of the outdoor mesh are similar to all other previous studies on this building model. The ceiling and two sides of the tunnel are set as slip walls, and the floor is set as a no-slip wall with the wall function of Spalding's law. A velocity inlet and a pressure outlet are applied in this simulation. The inlet velocity profile $U(z)$, turbulence kinetic energy $k(z)$, turbulent dissipation rate $\varepsilon(z)$, and special dissipation rate $\omega(z)$ are specified as the same as those in van Hooff et al. [47], that is

$$U(z) = \frac{u_*}{\kappa}\ln\left(\frac{z+z_0}{z_0}\right), \tag{10}$$

$$k(z) = 0.033U_{ref}^2\exp\left(-0.32\frac{z}{H}\right), \tag{11}$$

$$\varepsilon(z) = \frac{(u_*)^3}{\kappa(z+z_0)}, \tag{12}$$

$$\omega(z) = \frac{\varepsilon(z)}{C_\mu k(z)}, \tag{13}$$

where the empirical constant $C_\mu = 0.09$, and the von Karman constant $\kappa = 0.42$. The friction velocity u_* and aerodynamic roughness length z_0 determined based on a fitting procedure to approximate the profile given in the wind tunnel experiment in Tominaga and Blocken [46]. In the current study, for the reference speed $U_{ref} = 4$ m/s, these values are set to $u_* = 0.3973$ m/s and $z_0 = 0.0423$ m; for other reference speed $U_{ref} = 2$, 6, or 8 m/s, the value of u_* is scaled accordingly.

Again, the simulations in this section adopt the SST k-ω model in solving the steady RANS equations in OpenFOAM, as those described in the 2D simulations in Section 3. The SIMPLE algorithm is applied as the pressure–velocity calculation procedure for the continuity and momentum equations. The TVD scheme is employed for all the advection terms. Convergence is assumed to be obtained when all the scaled residuals reach the 10^{-4} level and all the physical quantities do not change significantly over the iterations. For validation, the simulation results of the case with no FDP are compared to the experimental results in Tominaga and Blocken [46], and they show good agreement. Please see supplementary material B for the details of this validation, along with the grid independence test.

5.3. Simulation results and discussion

The airflow control performance is evaluated by comparing the normalized volumetric ventilation rate Q_n in forward and reverse directions, and it is defined as

$$Q_n = \frac{Q}{whU_{ref}}, \tag{14}$$

where Q (m^3/s) is the volumetric ventilation rate, w is the opening width, and h is the opening height. Q is also the flow rate passing

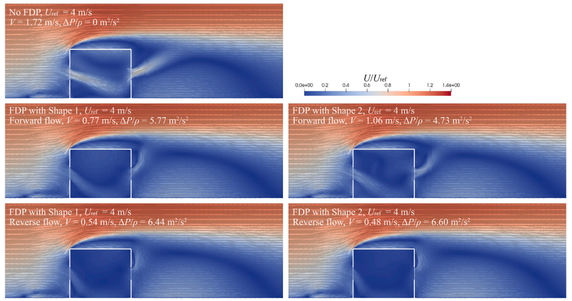

Fig. 14. Velocity fields at the plane $y = 0$ at the reference wind speed of 4 m/s.

applications.

In summary, this study's findings underscore the significance of FDP in enhancing building ventilation efficiency, offering a promising solution for energy savings and improved indoor air quality. Further exploration of its practical applications and integration into sustainable building design can pave the way for greener and more comfortable built environments.

CRediT authorship contribution statement

Hong Hu: Writing – review & editing, Writing – original draft, Validation, Software, Project administration, Methodology, Investigation, Data curation, Conceptualization. **Ikuryo Son:** Investigation. **Hideki Kikumoto:** Writing – review & editing, Supervision. **Bingchao Zhang:** Writing – review & editing, Methodology. **Kengo Hayashi:** Conceptualization.

Declaration of competing interest

The authors declare that they have no known competing financial interests or personal relationships that could have appeared to influence the work reported in this paper.

Data availability

Data will be made available on request.

Acknowledgements

This research was conducted with the support of the Window Research Institute 2021 Research Grant and the Japan Society for the Promotion of Science (JSPS) KAKENHI Grant Number 23KJ0520. We would like to express our gratitude for their assistance and funding.

Appendix A. Supplementary data

Supplementary data to this article can be found online at https://doi.org/10.1016/j.buildenv.2024.111259.

References

[1] M. Awada, B. Becerik-Gerber, S. Hoque, Z. O'neill, G. Pedrielli, J. Wen, T. Wu, Ten questions concerning occupant health in buildings during normal operations and extreme events including the COVID-19 pandemic, Build. Environ. 188 (2021) 107480, https://doi.org/10.1016/j.buildenv.2020.107480.

[2] Y. Zhai, A. Honnekeri, M. Pigman, M. Fountain, H. Zhang, X. Zhou, E. Arens, Use of adaptive control and its effects on human comfort in a naturally ventilated office in Alameda, California ☆, Energy Build. 203 (2019) 109435 https://doi.org/10.1016/j.enbuild.2019.109435.

[3] Y. An, T. Xia, R. You, D. Lai, J. Liu, C. Chen, A Reinforcement Learning Approach for Control of Window Behavior to Reduce Indoor PM 2.5 Concentrations in Naturally Ventilated Buildings, 2021, https://doi.org/10.1016/j.buildenv.2021.107978.

[4] W. Li, Q. Chen, Design-based natural ventilation cooling potential evaluation for buildings in China, J. Build. Eng. 41 (2021) 102345, https://doi.org/10.1016/j.jobe.2021.102345.

[5] H.M. Maghrabie, M.A. Abdelkareem, K. Elsaid, E.T. Sayed, A. Radwan, H. Rezk, T. Wilberforce, A.G. Abo-Khalil, A.G. Olabi, A review of solar chimney for natural ventilation of residential and non-residential buildings, Sustain. Energy Technol. Assessments 52 (2022) 102082, https://doi.org/10.1016/J.SETA.2022.102082.

[6] H. Zhang, D. Yang, V.W.Y. Tam, Y. Tao, G. Zhang, S. Setunge, L. Shi, A critical review of combined natural ventilation techniques in sustainable buildings, Renew. Sustain. Energy Rev. 141 (2021) 110795, https://doi.org/10.1016/J.RSER.2021.110795.

[7] C. Allocca, Q. Chen, L.R. Glicksman, Design analysis of single-sided natural ventilation, Energy Build. 35 (2003) 785–795, https://doi.org/10.1016/S0378-7788(02)00239-6.

[8] C. Ren, S.J. Cao, F. Haghighat, A practical approach for preventing dispersion of infection disease in naturally ventilated room, J. Build. Eng. 48 (2022) 103921, https://doi.org/10.1016/J.JOBE.2021.103921.

[9] J. Cho, C. Yoo, Y. Kim, Effective opening area and installation location of windows for single sided natural ventilation in high-rise residences, J. Asian Architect. Build Eng. 11 (2012) 391–398, https://doi.org/10.3130/jaabe.11.391.

[10] X. Zhang, A.U. Weerasuriya, J. Wang, C.Y. Li, Z. Chen, K.T. Tse, J. Hang, Cross-ventilation of a generic building with various configurations of external and internal openings, Build. Environ. 207 (2022) 108447, https://doi.org/10.1016/J.BUILDENV.2021.108447.

[11] H. Shetabivash, Investigation of opening position and shape on the natural cross ventilation, Energy Build. 93 (2015) 1–15, https://doi.org/10.1016/J.ENBUILD.2014.12.053.

[12] S. Kato, R. Kono, T. Hasama, R. Ooka, T. Takahashi, A wind tunnel experimental analysis of the ventilation characteristics of a room with single-sided opening in uniform flow, Int. J. Vent. 5 (2006) 171–178, https://doi.org/10.1080/14733315.2006.11683734.

[13] A. Sarkar, R. Bardhan, Improved indoor environment through optimised ventilator and furniture positioning: A case of slum rehabilitation housing, Mumbai, India, (n. d.) https://doi.org/10.1016/j.foar.2019.12.001.,.

[14] S. Haddad, A. Synnefa, M. Angel Padilla Marcos, R. Paolini, S. Delrue, D. Prasad, M. Santamouris, On the potential of demand-controlled ventilation system to enhance indoor air quality and thermal condition in Australian school classrooms,

through the opening on the windward wall, and it is calculated by integrating the normal velocity over the area of the opening. The value of Q_n is equal to the average normal velocity over the opening normalized by the reference speed.

The results of the normalized volumetric ventilation rate Q_n are presented in Fig. 13. The blue part of the figure represents the results of the reverse flow (i.e., the FDP is installed in the reverse direction so that the airflow is relatively difficult to penetrate) at different wind speeds, while the orange part represents the results of forward flow (i.e., the FDP is installed in the forward direction so that the airflow is relatively easy to penetrate).

These results show that the volumetric ventilation rate is not proportional to the approaching wind when the FDP is installed, and this is true for both forward and reverse flows. Q_n is relatively higher in the forward flow and increases with the reference wind speed. For the reverse flow, Q_n is relatively lower, and it decreases as the reference wind speed increases. The Q_n values asymptotically converge to a certain value with increased reference wind speed for the forward and reverse flows. However, even in the forward flow with a large reference wind speed, the Q_n value is still lower than that of the case with no FDP because of the inevitable porosity of the FDP.

Generally, the FDP with Shape 2 provides more ventilation than the FDP with Shape 1 in the forward direction, while it provides less ventilation in the reverse direction. For example, at $U_{ref} = 8$ m/s, the Q_n value in that of Shape 2 is 20 % higher than that in the case of Shape 1 in the forward direction, and it is 14 % lower in the reverse direction. This indicates better performance in controlling the airflow direction. Therefore, Shape 2 outperforms Shape 1. In addition, the difference in volumetric ventilation rate becomes more significant with the increase in U_{ref}, indicating that FDP performs better with large external wind.

Notably, at $U_{ref} = 4$ m/s, the Q_n value of Shape 2 exhibits a sudden jump, and it becomes almost constant when U_{ref} further increases to 6 or 8 m/s. This means that when $U_{ref} > 4$ m/s, the volumetric ventilation rate is almost proportional to the approaching wind. This behavior is in line with the performance curves in Fig. 10. Notice that in Fig. 10, the minor loss coefficient becomes almost constant when the Reynolds number in Equation (8) reaches a critical value, indicating that the pressure loss becomes proportional to the dynamic pressure, and the flow becomes fully developed turbulence. For forward flow, the critical Reynolds numbers are approximately 3000 and 1300 for Shapes 1 and 2, respectively. In Fig. 13, the Reynolds number in the case of Shape 2 is 546 at $U_{ref} = 2$ m/s, but it reaches 1693 at $U_{ref} = 4$ m/s, which causes this sudden change and lock down in Q_n. However, the Reynolds numbers in the case of Shape 1 are all lower than the critical value of 3000, so the Q_n value increases slowly, and it is lower than that of Shape 2.

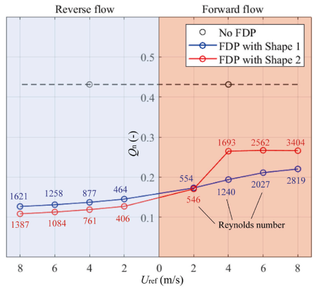

Fig. 13. Normalized volumetric ventilation rate for all cases at different reference wind speeds. For the case of no FDP, the simulation is conducted only for the reference wind speed of 4 m/s, while the value is assumed to be the same for other reference wind speeds. The corresponding Reynolds numbers of the flow in FDP are also given near the sample points.

Fig. 14 provides the velocity fields at $U_{ref} = 4$ m/s for all the cases for comparison. Notice that the velocity field is affected only by the pressure drop at the opening, so the ventilation route does not change significantly. Though the mechanism is still cross-ventilation, the jet flow in the building shows a downward trend and quickly goes down to the floor when the pressure drop is large. In addition, Fig. 14 also shows that the difference between the forward and reverse flow fields is more significant using the FDP with Shape 2 than using the FDP with Shape 1. Notably, the forward flow field is closer to the flow field of no FDP.

6. Conclusion

This study first delved into a parametric exploration of the internal shapes of FDPs based on the principles of the Tesla valve. The pressure loss ratio, indicating the difference between forward and reverse flow, was used as the main indicator to evaluate the performance of Tesla valve shapes. The optimal shape (named Shape 2) was selected, and its relationships between the pressure loss and approaching flow speed in FDP were modeled. Along with the shape proposed by a previous study (named Shape 1), the FDPs with these shapes were installed in a typical building model to compare their flow control performance in a cross-ventilation scenario.

The parametric study of Tesla valve shapes revealed that the pressure loss ratio increases with the increase in bypass channel height and decreases with the increase in the main channel length or slope. However, when the main channel length and baffle thickness were fixed, the slope and bypass channel height became correlated, and the variation of the pressure loss ratio showed an initial increase followed by a decrease when the slope and the bypass channel height increased simultaneously. In this study, the shape with $\theta = 220^\circ$ and $H_2 = 4.91$ mm exhibited the highest pressure loss ratio of 4.2, followed closely by the shape with $\theta = 210^\circ$ and $H_2 = 3.58$ mm with a ratio of 4.1. However, the former shape exhibited a pressure loss in the forward flow that was 40 % higher than the latter shape, which was unfavorable to ventilation. Therefore, the latter shape was selected as Shape 2 and was studied further. At a Reynolds number of 1800, the pressure loss ratio of Shape 2 is double that of Shape 1.

The performance of FDPs with Shapes 1 and 2 for building ventilation applications was evaluated and compared. The results showed that the ventilation rate differed when the FDP was installed in different directions at the building's windward openings. The difference in volumetric ventilation rate became more significant with increasing external wind speed, indicating that FDP performs better with large external wind. In addition, Shape 2 outperformed Shape 1 at all external wind speeds. It provides 20–30 % more ventilation in the forward direction and 10–15 % less ventilation in the reverse direction.

While the shape parametric study in this paper holds its own significance in delineating the impact of each parameter on the target performance, it might also be valuable to identify a global extremum for the optimal shape parameter set, using optimization algorithms, such as Bayesian optimization [45], genetic algorithms [53] or machine learning techniques [54]. In addition, sensitivity analysis in geometric parameter optimization is also a valuable method to evaluate the impact of different geometric parameters on the performance of FDP. Future studies could incorporate approaches such as analytical methods [55], numerical methods [56], and machine learning methods [57] to identify the most efficient parameter and benefit the FDP design in real-world

HU et al.

PERFORMANCE CURVES

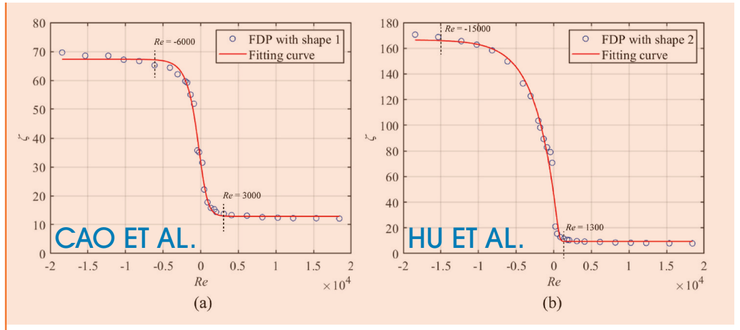

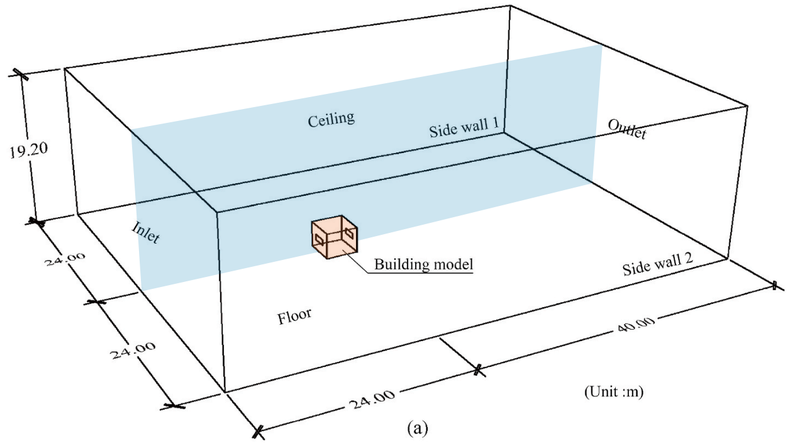

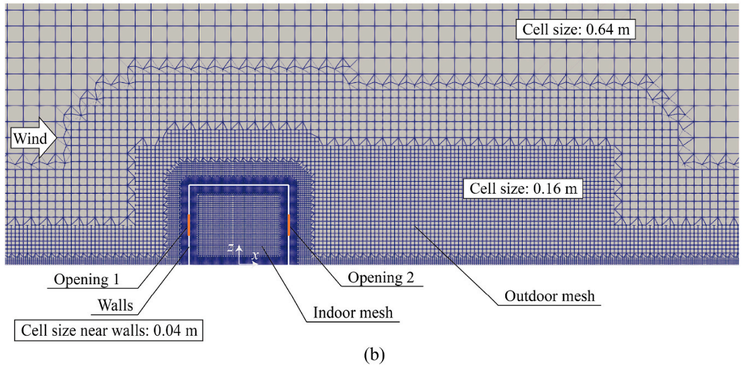

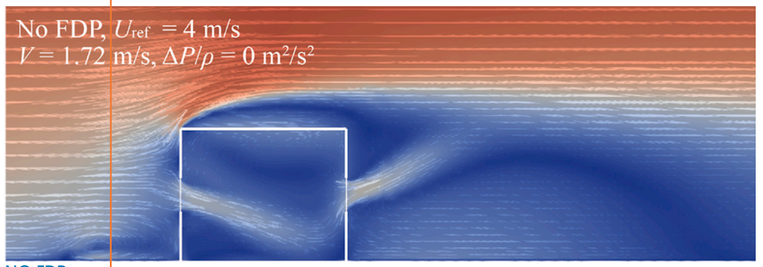

NO FDP

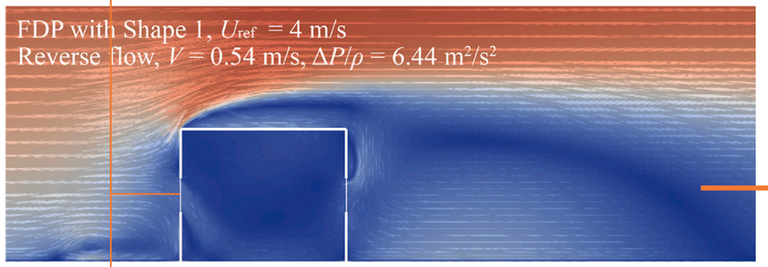

CAO ET AL.

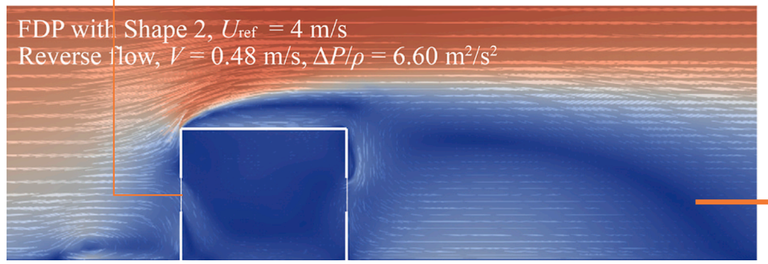

HU ET AL.

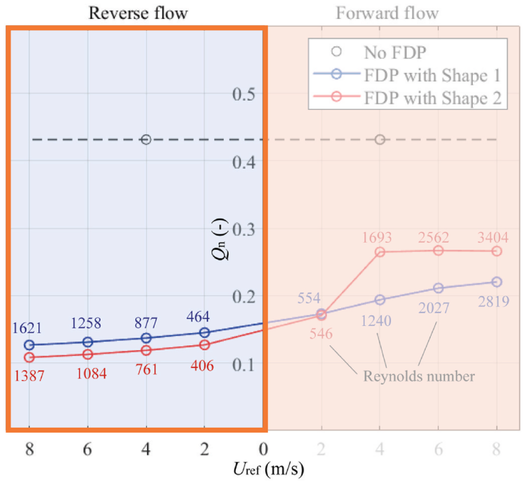

NORMALIZED VENTILATION RATE

$$Q_n = \frac{Q}{whU_{ref}}$$

SIMULATION SET UP

SIMULATION

NORMALIZED VENTILATION RATE

HU et al.

PERFORMANCE CURVES

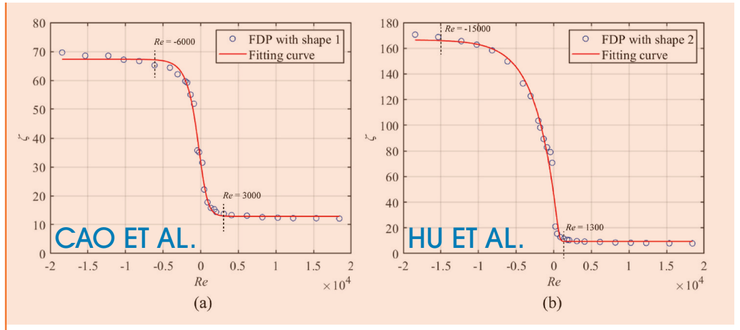

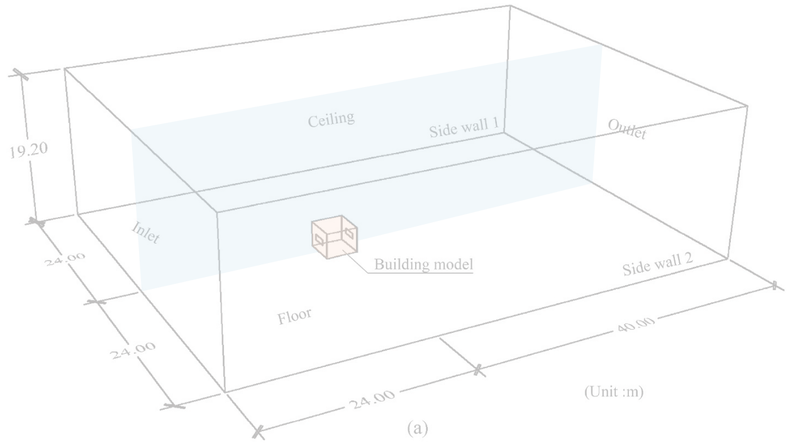

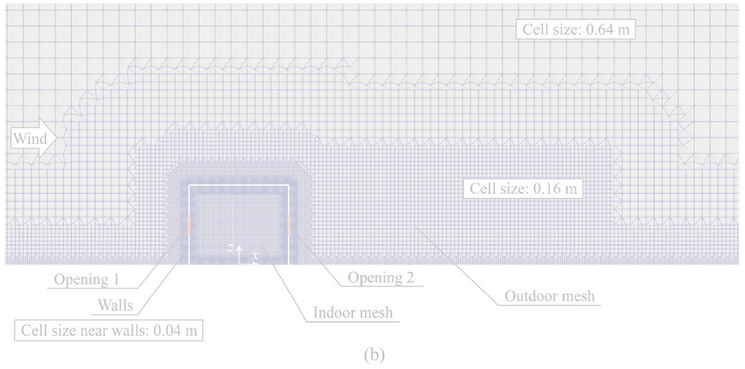

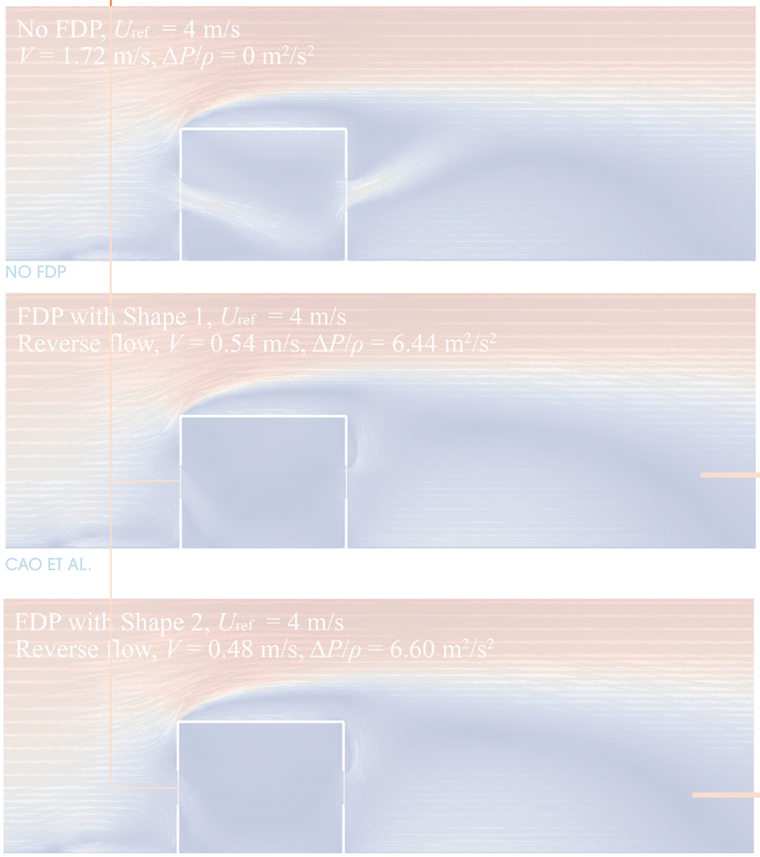

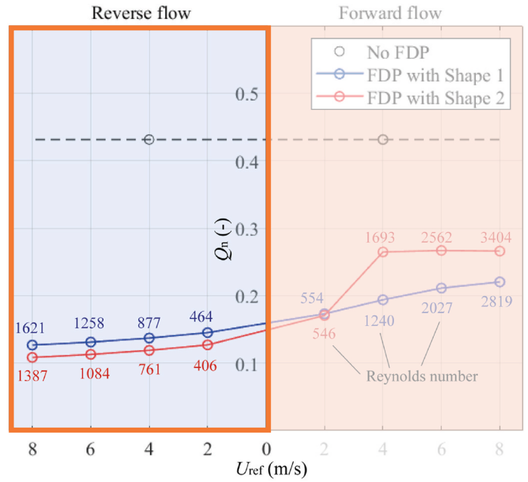

NORMALIZED VENTILATION RATE

$$Q_n = \frac{Q}{whU_{ref}}$$

SIMULATION SET UP

SIMULATION

NORMALIZED VENTILATION RATE

SLIGHT ISSUE:

SLOW AND COMPUTATIONALLY EXPENSIVE

SPEED IT UP

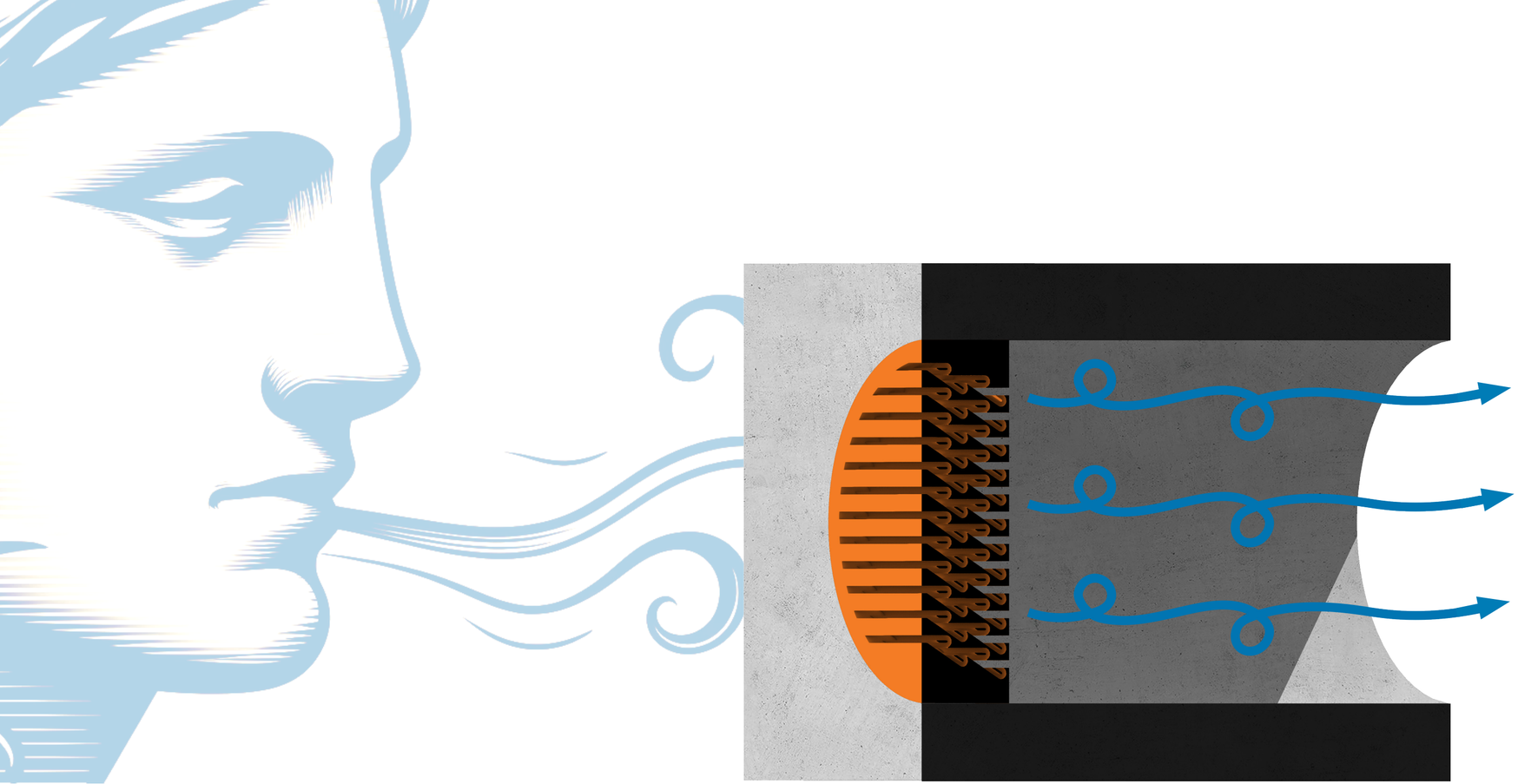

PHYSICS CALCULATIONS

```python
def get_A_Dh(shape: str, dim_1: float, dim_2: float = None) -> tuple[float]:

  """
  Calculates an inlet's area (A) and hydrolic dimater (Dh) based on its diameter(!)

  A = pi * r^2
  Dh = 4A / circumference

  Parameters:
  diameter (float): diameter of the inlet. This value should represent the diameter which air can flow through.
  shape (str): shape of the inlet: circle, sqaure or rectangle. The circle assumes the diameter as input!

  Returns:
  area (A) and hydrolic diameter (Dh) as a tuple (tuple(K, Dh)).

  Source:
  Kennisbank bouwfysica: Meerzone luchtstroommodellen, p.4.

  """

  pi = np.pi

  match shape:

    case "circle":
      #dim_1 assumed to be the diamtere of the circle!
      A = pi * (dim_1 / 2) ** 2
      circumference = dim_1 * pi
      Dh = dim_1

    case "square":
      #In case of a sqaure channel, dim_1 is defined as the length of one side
      A = dim_1 ** 2
      circumference = dim_1 * 4
      Dh = 4 * A / circumference

    case "rectangle":
      if dim_2 == None: raise ValueError("rectangle requires two dimensions")
      A = dim_1 * dim_2
      circumference = 2 * dim_1 + 2 * dim_2
      Dh = 4 * A / circumference

    case other: raise ValueError("shape not valid. Choose circle or square")

  return A, Dh

def get_wind_speed(V: np.ndarray[np.float64], inlet_height: float, terrain_case: str) -> np.ndarray[np.float64]:

  K,a = get_K_a_constants(terrain_case)

  return V * K * inlet_height ** a

def calculate_wind_pressure(v: np.ndarray, Cp: float, p: float = 1.225) -> np.ndarray[np.float64]:
    """
    Calculate wind pressure for given wind speeds.

    Parameters:
        v (np.ndarray): Array of wind speeds working on facade in meters per second.
        Cp (float): Wind pressure coefficient

    Returns:
        np.ndarray: Array of wind pressures corresponding to the input wind speeds.
    """
    # Constants
    p = 1.225  # Air density in kg/m^3 (typical value at sea level)

    # Calculate wind pressure using the formula dP = 0.5 * p * Cp * v^2
    dP = 0.5 * p * Cp * v**2

    return dP

def calculate_channel_capacity(A, P_dif, density, wall_friction_coef, channel_length, Dh, loss_coef, secondary_losses=0):

    C_v = A * (np.sqrt(2 / density)) / (1 + np.sqrt((wall_friction_coef * channel_length / Dh) + loss_coef + secondary_losses))

    Q = C_v * P_dif ** (1/2)

    V_inlet = Q / A

    return C_v, Q, Q * 3600, V_inlet

def calculate_reynolds_number(V: np.ndarray[np.float64], Dh: float, v: float = 1.5e-5,  a: float = 1.0):
    """
    Calculate the Reynolds number for a fluid flow using:

    Re = Vc * D / v where Vc = V / a

    Parameters:
    - V (float): velocity of the fluid [m/s].
    - D (float): diameter of main channel [m].
    - v (float): viscosity of the fluid [Pa*s].
    - a (float): porosity of the FDP (ratio open to closed surface of FDP)

    Returns:
    - Reynolds number (float): Dimensionless quantity representing the flow regime.

    based on Cao et al., and Hu et al.
    """

    Vc = V / a

    return Vc * Dh  / v

def Hu_performance_curve(Re: np.ndarray[np.float64], data_of: str) -> np.ndarray[np.float64]:

  """
  There are some apparent mistakes in the paper of Hu et al. when explaining their parameters of their fitting curves
  I have corrected them based on their plots of the curves:

  - In formula (9): a H1 / v should be H1 / a * v, as it is everywhere else throughout the paper
  - Parameter A: seems too low when compared to the plotted curve. I changed 149.1 to 170.0, which seems to correspond better to the final c
  - Parameter B: should be -8.46e-3 instead of -8.46e1

  Formula:

  S(V) = A + (D - A) / (1 + np.exp(B * Re + C)) ** s
  """

  match data_of:
    case "Cao et al.": A,B,C,D,s = 68.0, 1.93e-3, 0.399, 12.91, 0.4654
    case "Hu et al.": A,B,C,D,s = 170.0, 8.46e-3, 6.314, 8.17, 0.0416
    case other: raise ValueError("Name not valid, data is available from research by 'Hu et al' or 'Cao et al.'")

  return A + (D - A) / ((1 + np.exp(B * Re + C)) ** s)
```

$$\Delta P_w = \frac{1}{2} \cdot \rho \cdot C_p \cdot v^2$$

$$Re = \frac{V_c \cdot H_1}{v}$$

$$C_v = \frac{A \cdot \sqrt{\frac{2}{\rho}}}{1 + \sqrt{\lambda \cdot l / D_h + \Sigma \zeta_i}}$$

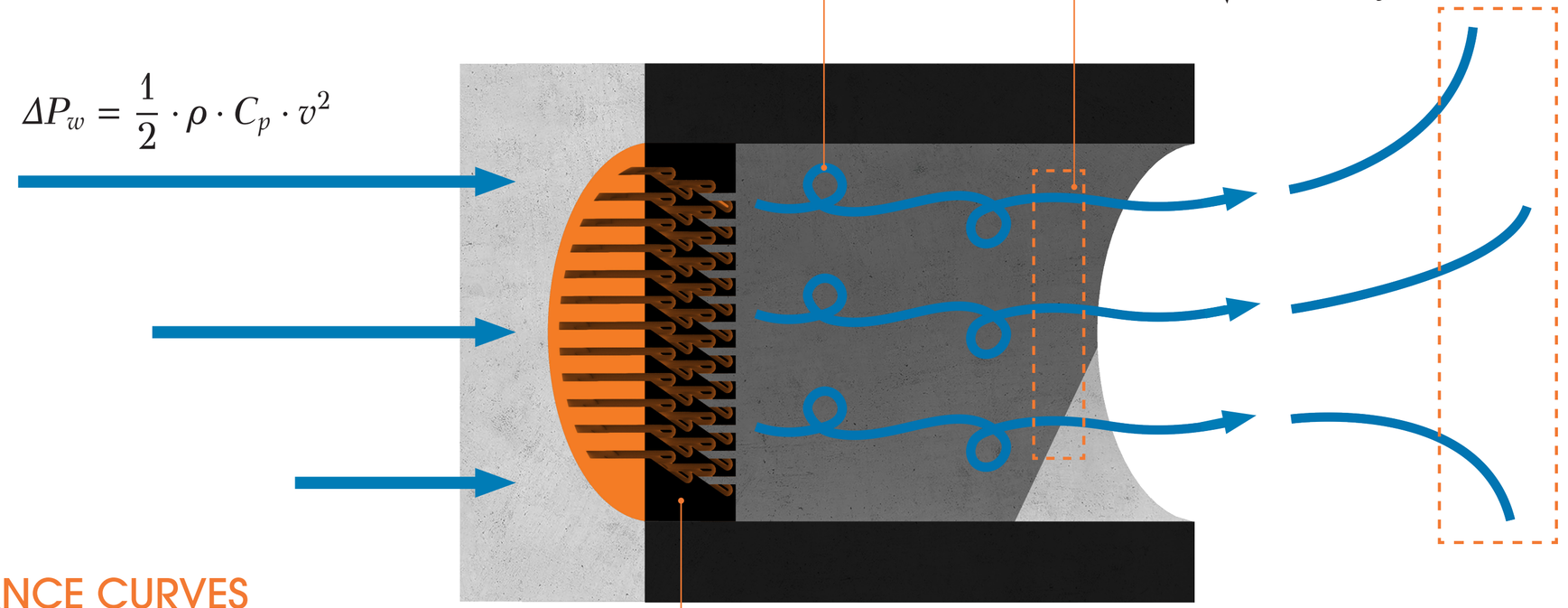

$$Q = C_v \cdot (\Delta P)^{\frac{1}{n}}$$

PERFORMANCE CURVES

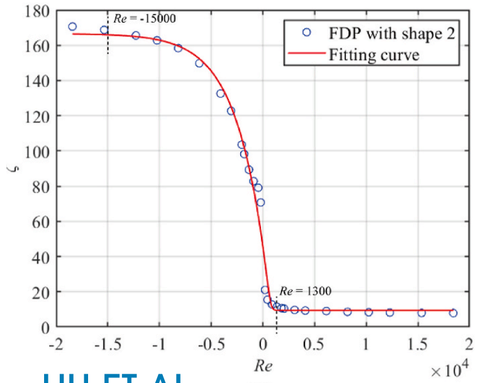

HU ET AL. (b)

$$\zeta = f(Re) = A + \frac{D - A}{(1 + \exp(B \cdot Re + C))^s}$$

$$\Delta P_w = \frac{1}{2} \cdot \rho \cdot C_p \cdot v^2$$

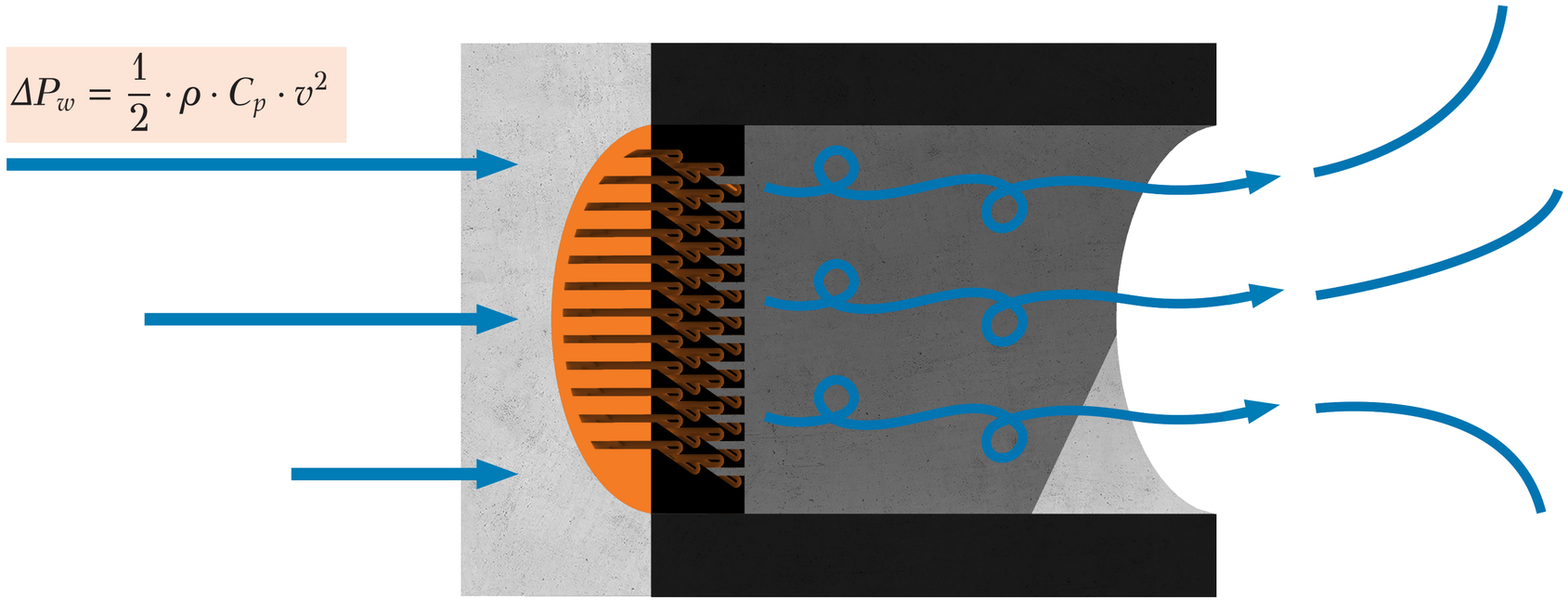

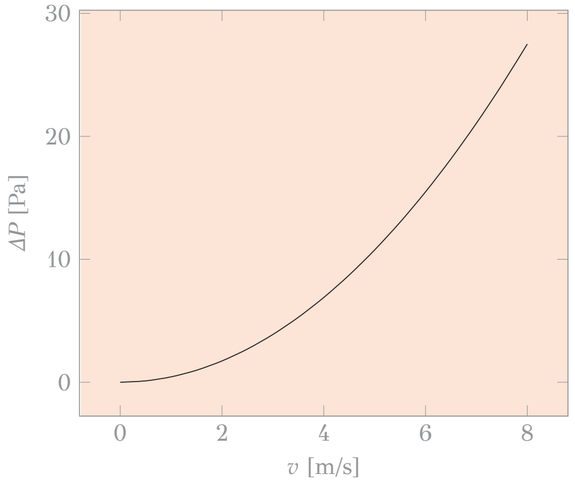

$$\Delta P_w = \frac{1}{2} \cdot \rho \cdot C_p \cdot v^2$$

$$Re = \frac{V_c \cdot H_1}{v}$$

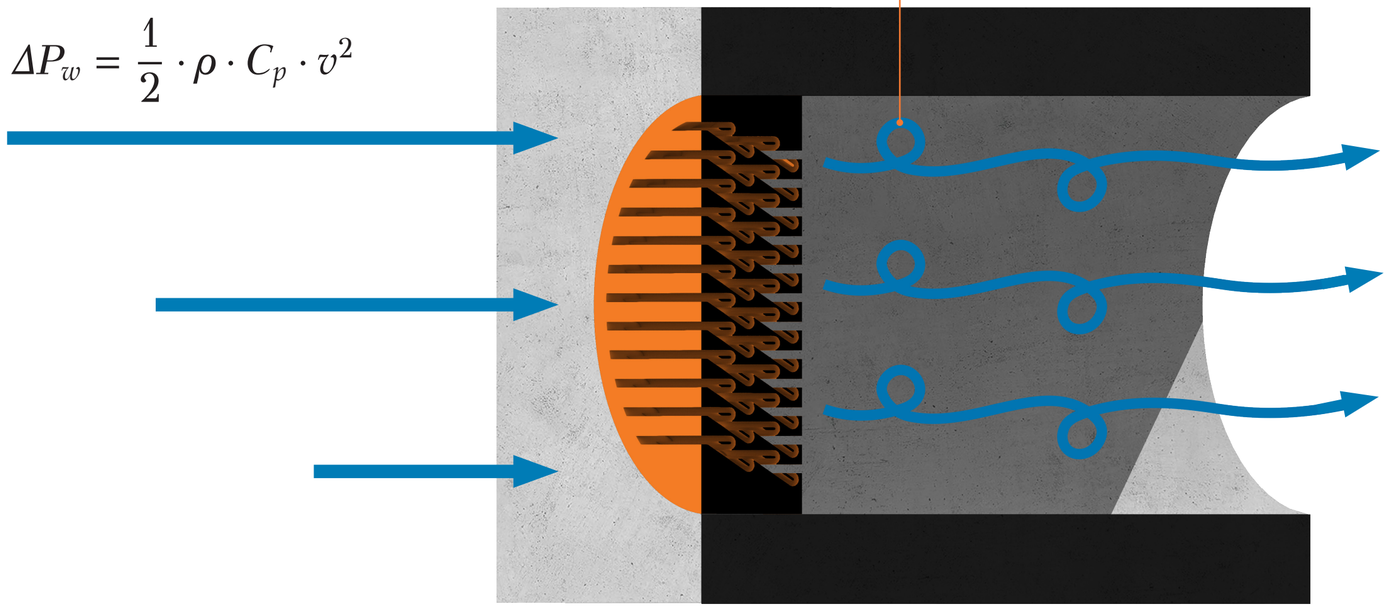

$$V_c = \frac{V}{a} \tag{11}$$

Re = Reynolds number [–]
H_1 = Height of the main channel [m]
v = Kinematic viscosity of air (1.510^{-5}[m^2/s])
V_c = Average speed in main channel [m/s]
V = Air speed [m/s]
a = Porosity [–]

However, as we have seen in formula 8, in the case of circular valves D_h equals its diameter. Therefore Re is expressed as:

$$Re = \frac{V_c \cdot H_1}{v} \tag{12}$$

When Re is low ($Re < 2300$ for air in a pipe system (Engineeringtoolbox, 2024b)), viscous forces are relatively dominant. leading to laminar flow characterized by smooth, predictable streamlines. On the other hand, at high Reynolds numbers ($Re > 4000$ for air in a pipe system (Engineeringtoolbox, 2024b)), inertial forces predominate, resulting in a turbulent flow marked by chaotic fluctuations and mixing. When passing through an FDP, large Reynolds number will be introduced into the flow due to its low porosity and the structure of the Tesla valves. This effect increases when wind speeds increase (Cao et al., 2020).

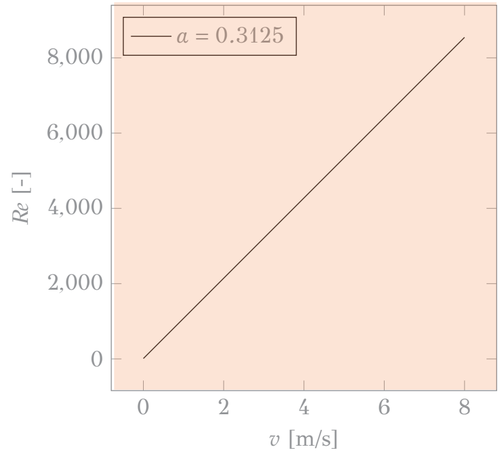

Figure 2: Reynold numbers according to formula 12 with $a = 0.3125$

$$Re = \frac{V_c \cdot H_1}{v}$$

$$\Delta P_w = \frac{1}{2} \cdot \rho \cdot C_p \cdot v^2$$

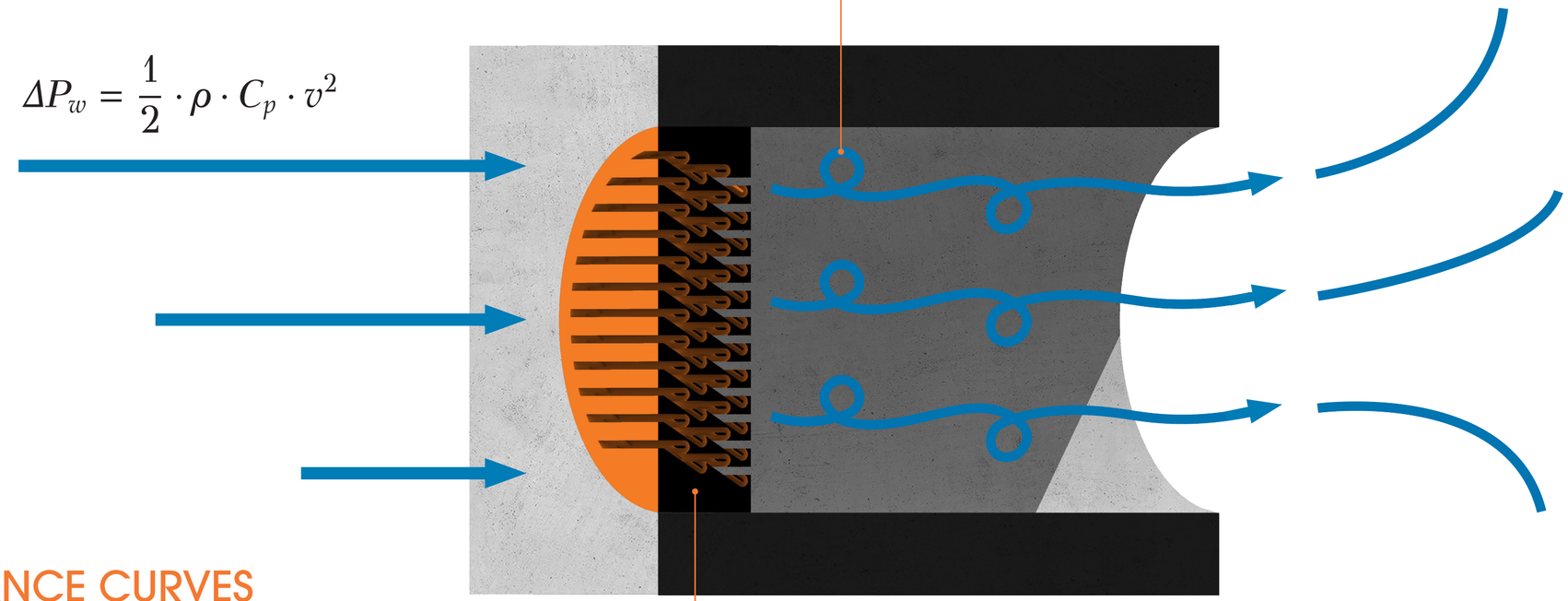

PERFORMANCE CURVES

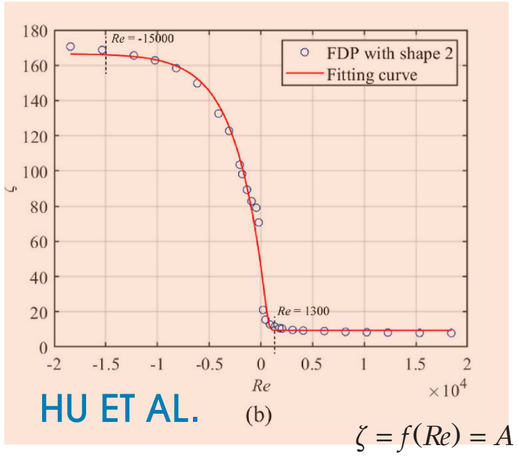

HU ET AL. (b)

$$\zeta = f(Re) = A + \frac{D - A}{(1 + \exp(B \cdot Re + C))^s}$$

$$\Delta P_w = \frac{1}{2} \cdot \rho \cdot C_p \cdot v^2$$

$$Re = \frac{V_c \cdot H_1}{v}$$

$$C_v = \frac{A \cdot \sqrt{\frac{2}{\rho}}}{1 + \sqrt{\lambda \cdot l/D_h + \Sigma \zeta_i}}$$

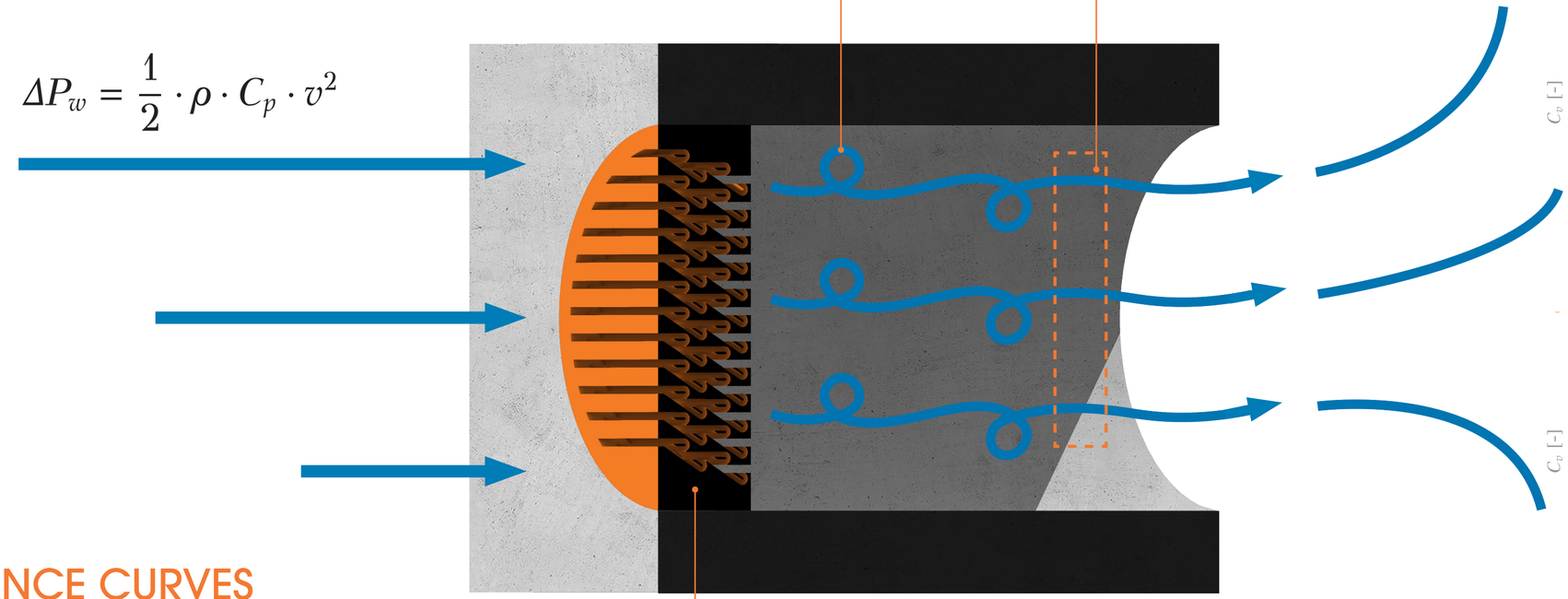

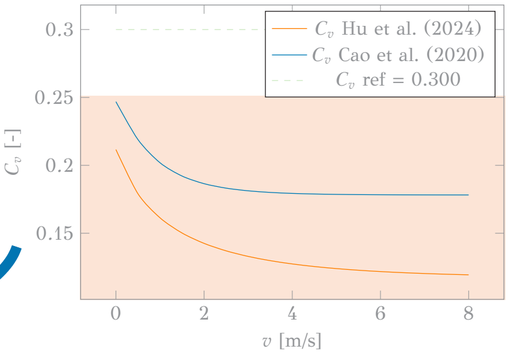

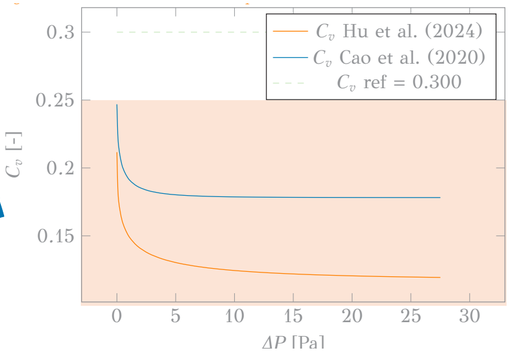

PERFORMANCE CURVES

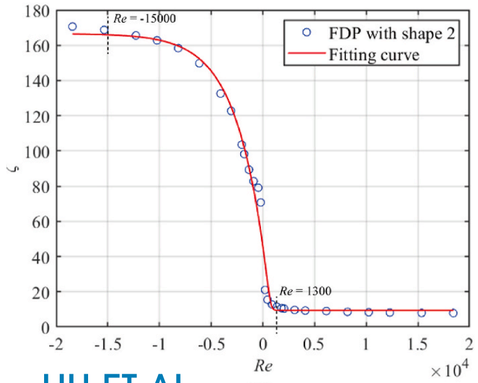

HU ET AL. (b)

$$\zeta = f(Re) = A + \frac{D - A}{(1 + \exp(B \cdot Re + C))^s}$$

$$\Delta P_w = \frac{1}{2} \cdot \rho \cdot C_p \cdot v^2$$

$$Re = \frac{V_c \cdot H_1}{v}$$

$$C_v = \frac{A \cdot \sqrt{\frac{2}{\rho}}}{1 + \sqrt{\lambda \cdot l / D_h + \Sigma \zeta_i}}$$

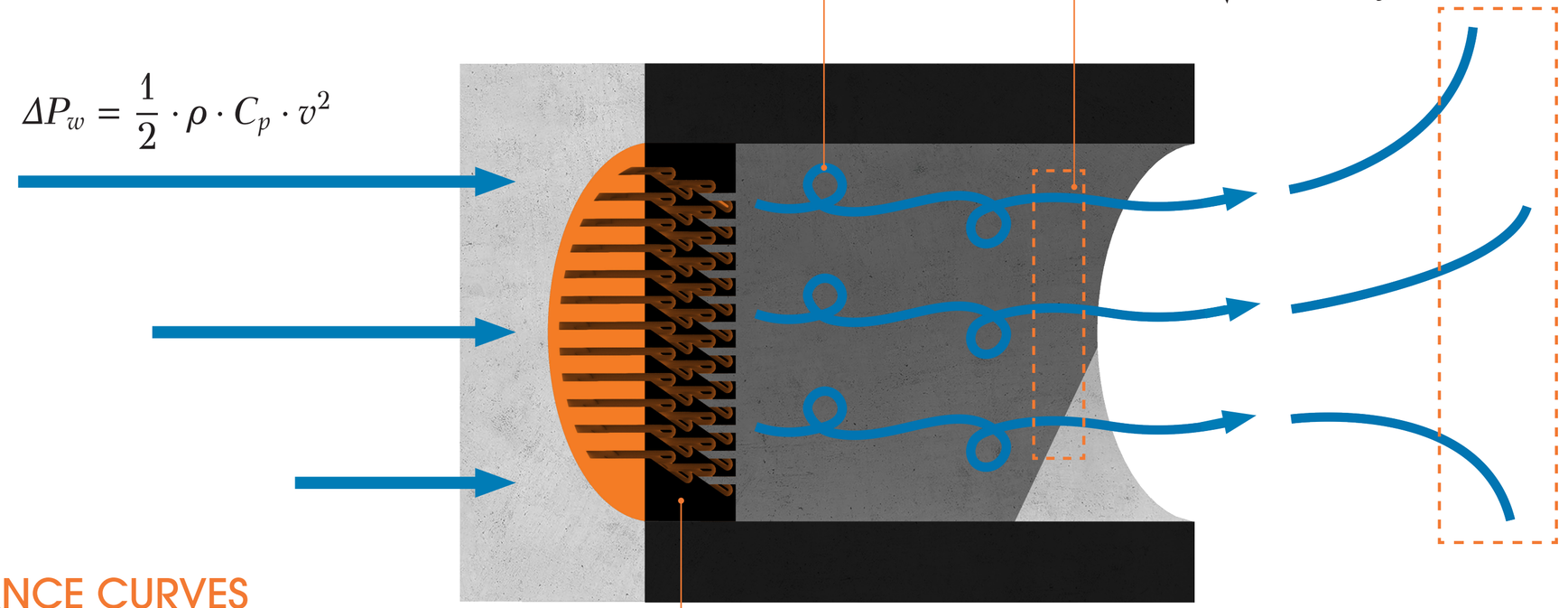

$$Q = C_v \cdot (\Delta P)^{\frac{1}{n}}$$

VENTILATION RATE

PERFORMANCE CURVES

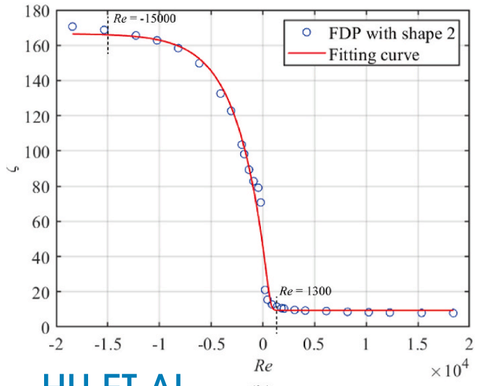

HU ET AL.

(b)

$$\zeta = f(Re) = A + \frac{D - A}{(1 + \exp(B \cdot Re + C))^s}$$

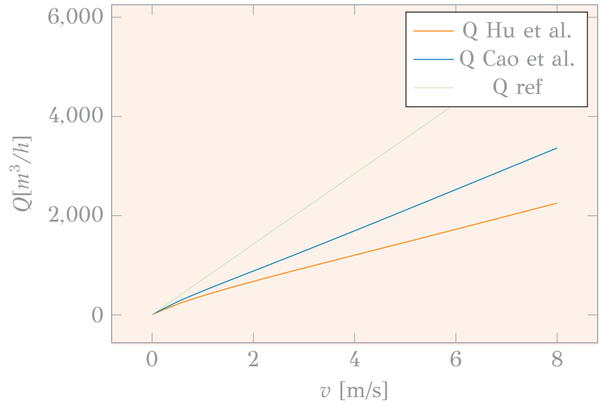

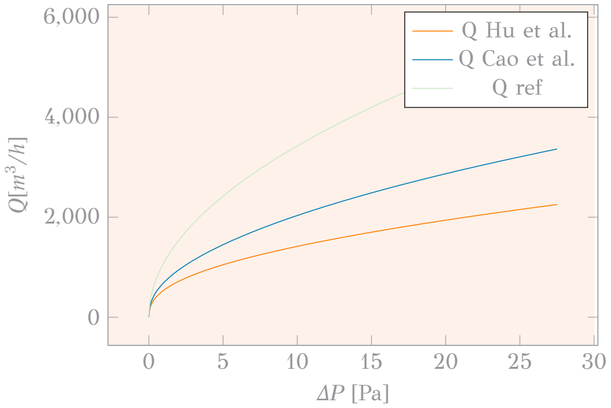

NORMALIZED VENTILATION RATE

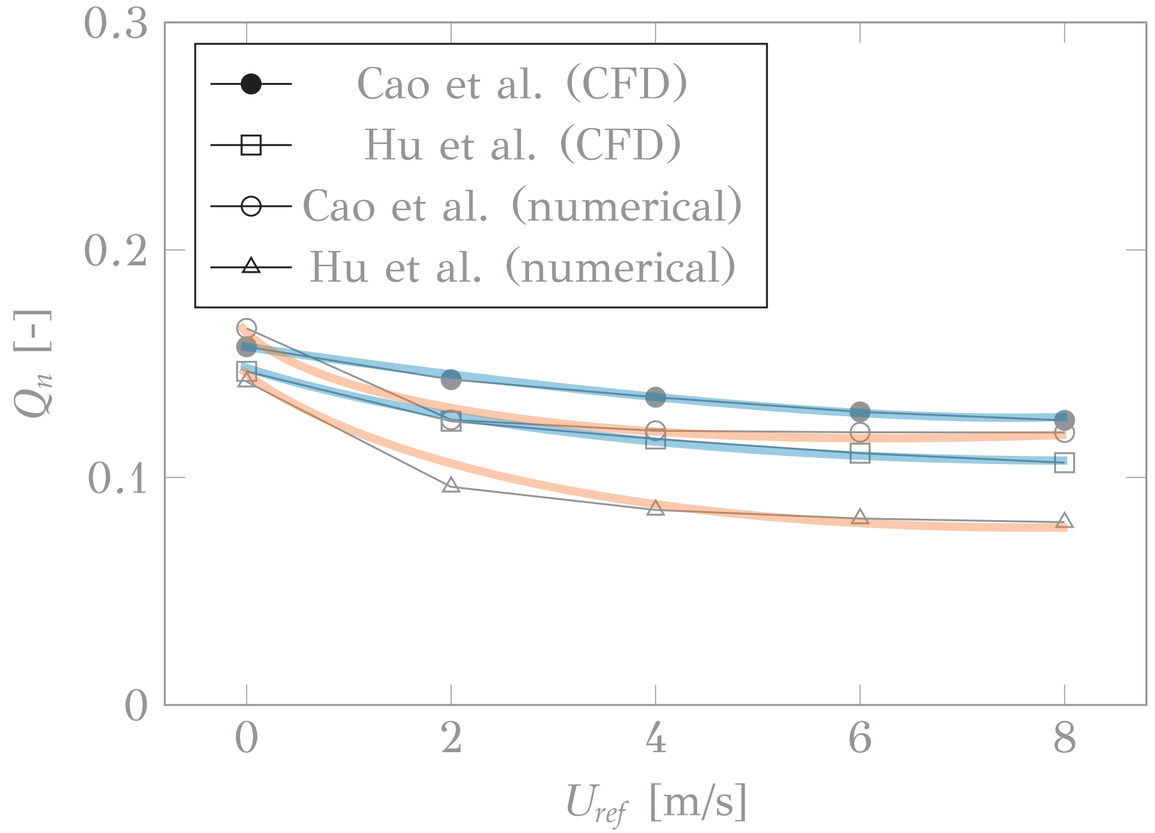

C_p = 1.2

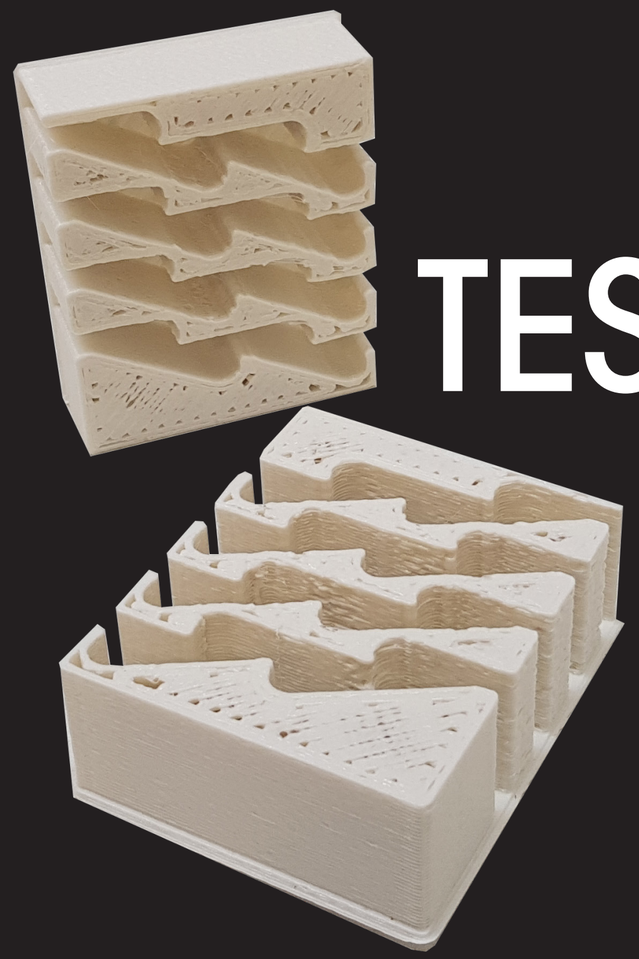

TESTING

PRINTING TRIALS

RESIN PRINT

PLA PRINT I

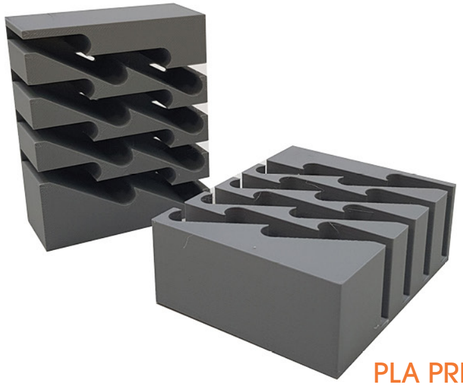

PLA PRINT II

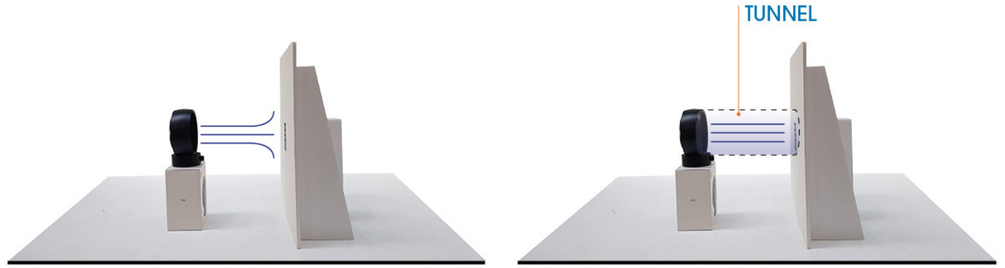
SET UP 1

TUNNEL
SET UP 2


REFERENCE GRILLE


TEST FDP


EXTECH SDL350
TESTO 400


VENTILATOR

?

UNPREDICTABLE
BEHAVIOR

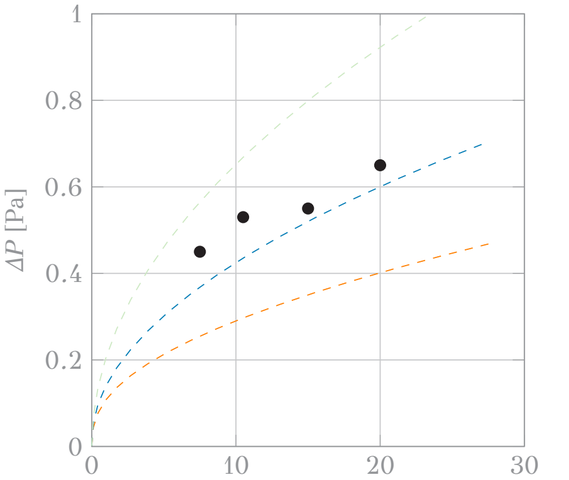

LOWEST MEASURED SPEEDS
STILL UNRELIABLE

TUNNEL

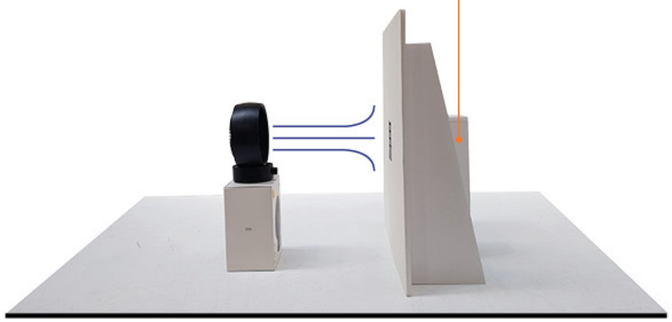

SET UP 1

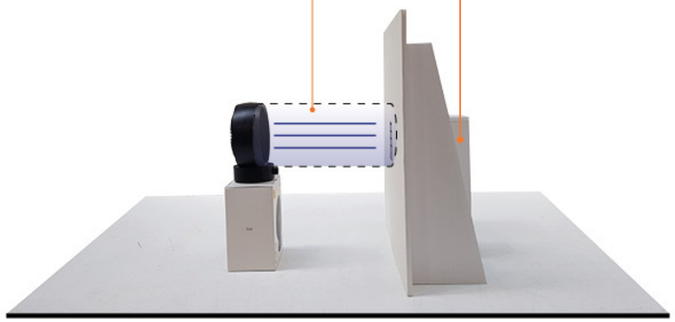

SET UP 2

REQUIREMENTS

$$\Delta P_w = \frac{1}{2} \cdot \rho \cdot C_p \cdot v^2$$

$$Re = \frac{V_c \cdot H_1}{v}$$

$$C_v = \frac{A \cdot \sqrt{\frac{2}{\rho}}}{1 + \sqrt{\lambda \cdot l/D_h + \Sigma\zeta_i}}$$

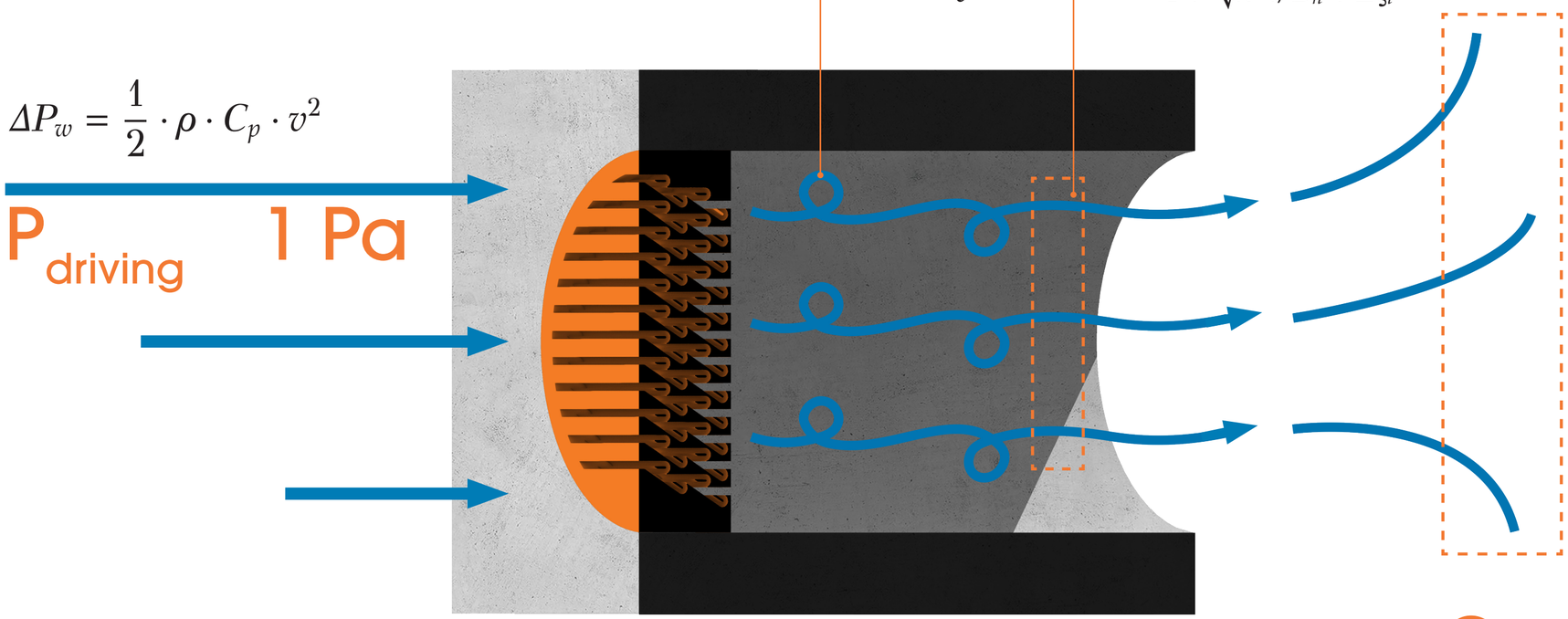

$$Q = C_v \cdot (\Delta P)^{\frac{1}{n}}$$

$P_{driving}$ 1 Pa

Q_{min} 50 m^3/s

V_{max} 0.2 m/s

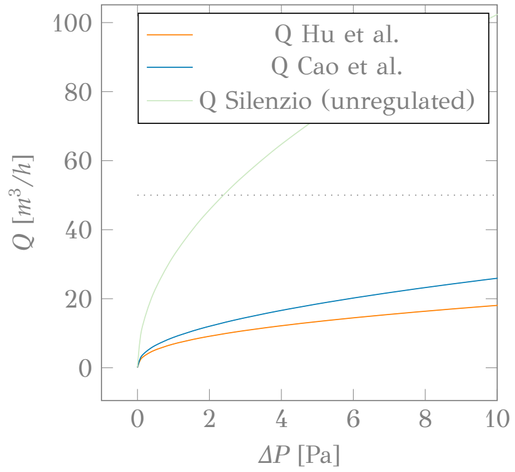
Q Hu et al.
Q Cao et al.
Q Silenzio (unregulated)
Q [m³/h]
ΔP [Pa]
0
20
40
60
80
100
0
2
4
6
8
10

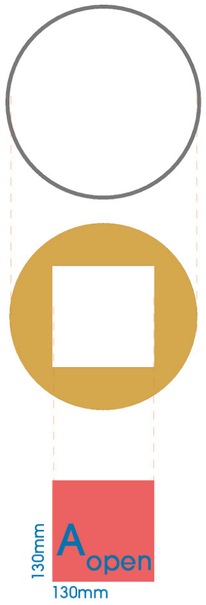
130mm
A open
130mm

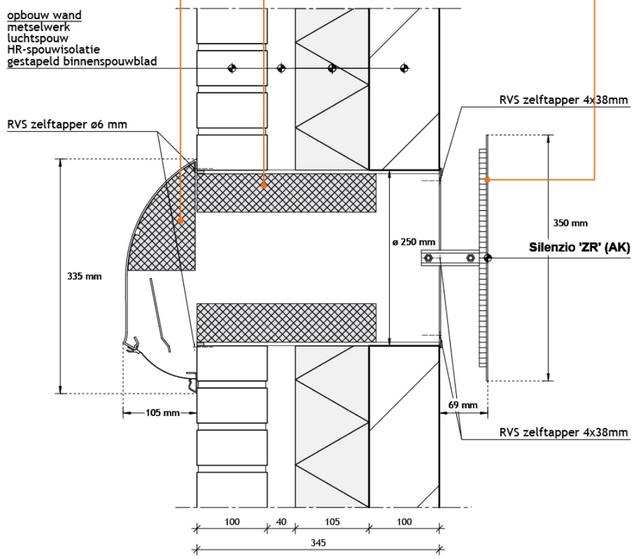
opbouw wand
metselwerk
luchtspouw
HR-spouwisolatie
gestapeld binnenspouwblad
RVS zelftapper ø6 mm
RVS zelftapper 4x38mm
335 mm
ø 250 mm
350 mm
Silenzio 'ZR' (AK)
105 mm
69 mm
RVS zelftapper 4x38mm
100
40
105
100
345

A DUCO SILENZIO

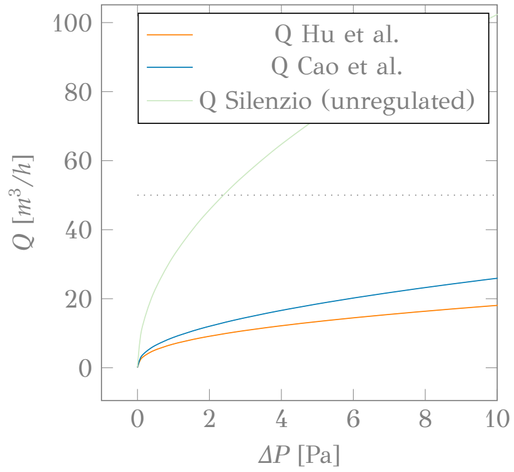

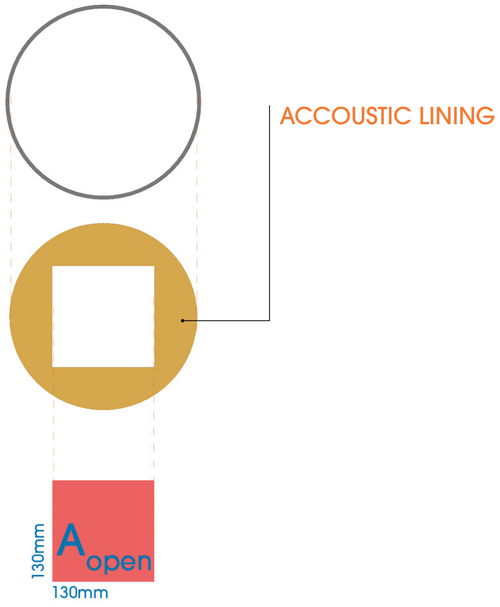

DUCO SILENZIO

A REQUIRED

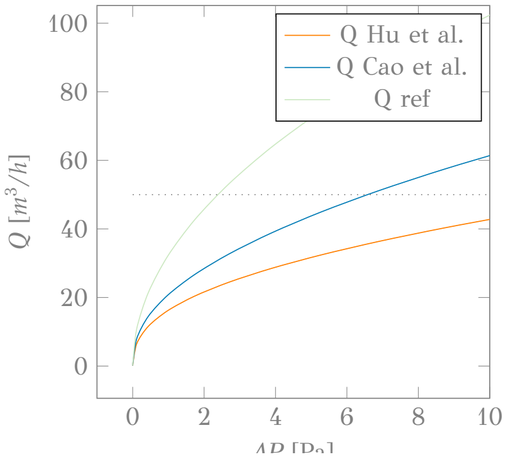

Q

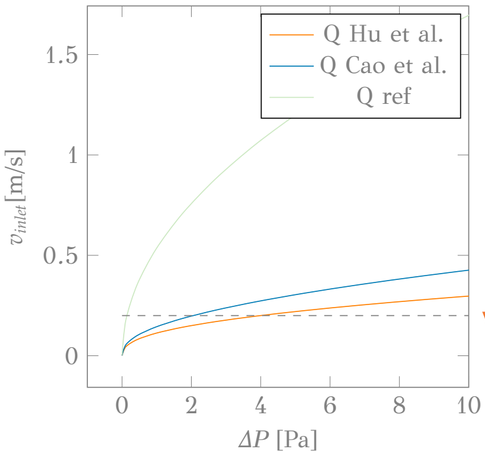

V

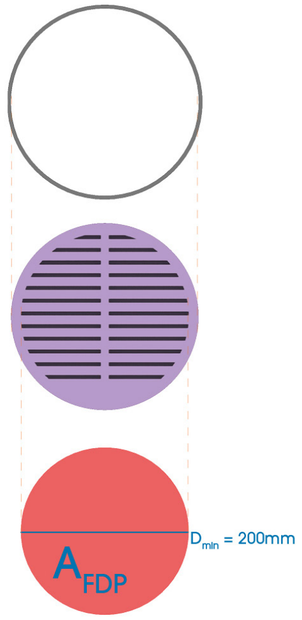

FDP

OPTIMIZATION AND CUSTOMIZATION

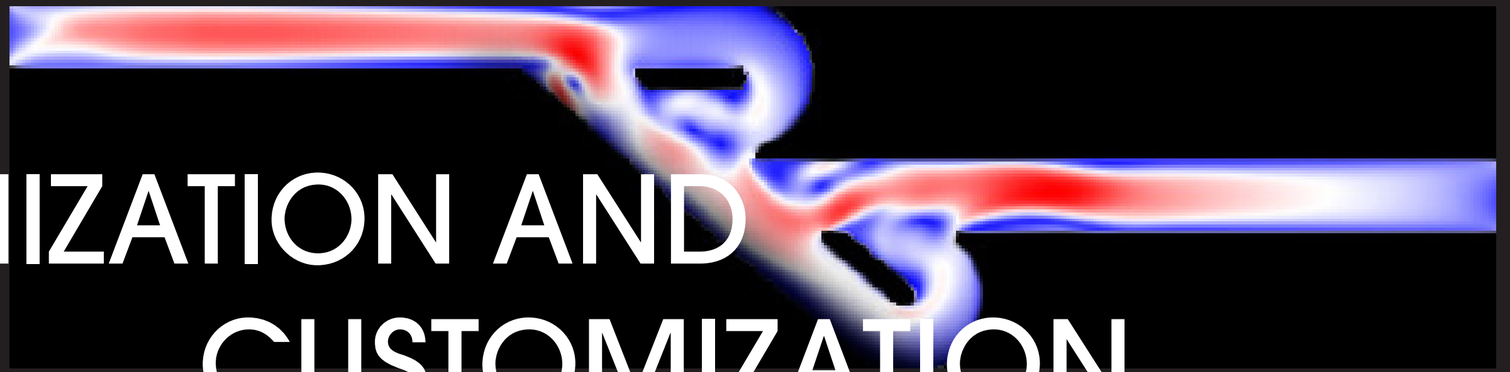

OPTIMIZE TOWARDS DESIRED BEHAVIOUR

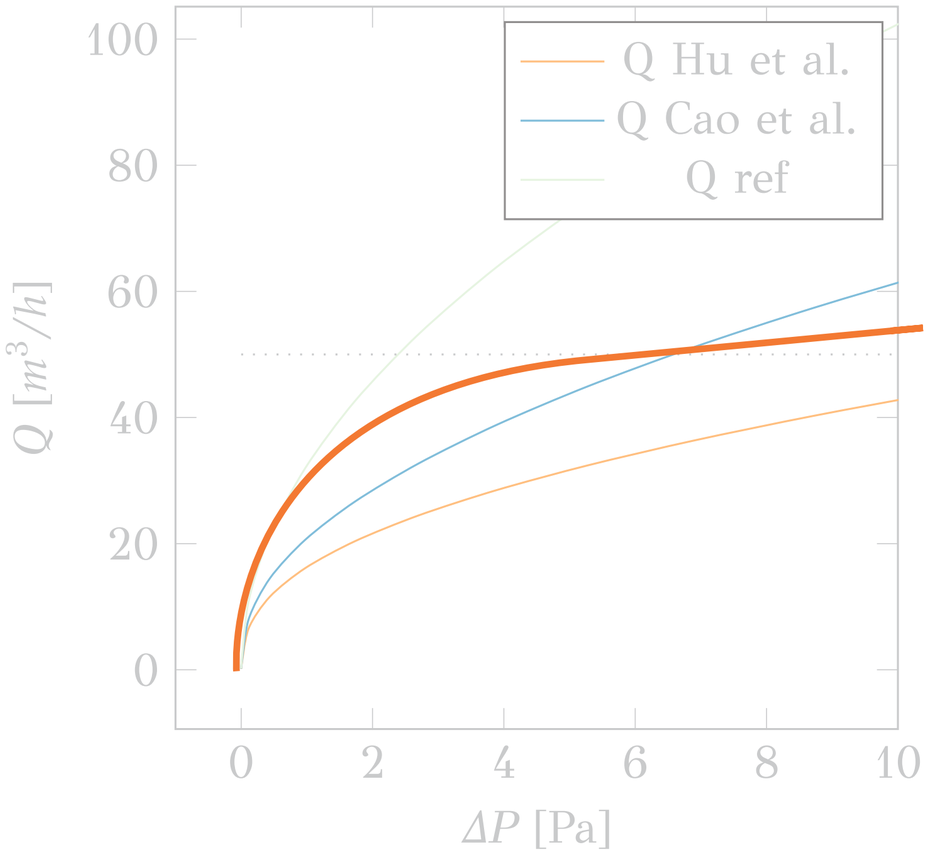

```
private void RunScript(Point3d O, int N, double H1, double H3, double L, double Theta, int rows, double extend, double boarderThickness, ref object V, ref ob
{
  //set up data containers
  DataTree<Plane> valvePlane = new DataTree<Plane>();
  DataTree<Point3d> valveSpinePoints = new DataTree<Point3d>();
  DataTree<Curve> valveGeometry = new DataTree<Curve>();

  List<Curve> channelUpperCurves = new List<Curve>();
  List<Curve> channelLowerCurves = new List<Curve>();
  List<Curve> baffleCurves = new List<Curve>();
  List < List < Curve >> channelBoundaryCurves = new List<List<Curve>>(channelUpperCurves, channelLowerCurves);


  List<Brep> innerSolids = new List<Brep>();
  DataTree<Brep> baffles = new DataTree<Brep>();

  //convert input angle to calculating values
  double A1 = 270 - Theta;
  double A1Rad = toRad(A1);

  double A2 = 90 - A1;
  double A2Rad = toRad(A2);

  double A3 = 90 - A2;
  double A3Rad = toRad(A3);

  //get planes
  Plane spawnPlane;
  Plane[] OPlanes;

  getPlanes(O, -A2Rad, out spawnPlane, out OPlanes);

  //get valve points
  double h1;
  List<Point3d> valveSpinePoints = getValveSpinePoints(N, H1, H3, L, A1Rad, A3Rad, out h1);

  //get valve geometry
  double radius;
  double width;
  List<Curve> singleValveGeometry = getValveGeometry(valveSpinePoints, A1Rad, H3, out radius, out width);

  double h2 = Math.Sin(A2Rad) * width;


  List<Curve> channelCurves;
  //List<Curve> baffleCurves;

  extend = Math.Max(radius, extend);

  double externalBoarderWidth;

  createValveRow(N, valveSpinePoints, singleValveGeometry, spawnPlane, OPlanes, extend, out channelCurves, out baffleCurves, out externalBoarderWidth);

  double arrayHeight = width / Math.Tan(A1Rad) + H1;

  externalBoarderWidth += boarderThickness;

  arrayValves(channelCurves, baffleCurves, rows, arrayHeight, externalBoarderWidth, radius, ref innerSolids, ref baffles);

  V = innerSolids;
  B = baffles;

}
[...]

double toRad(double A)
{
  return A * Math.PI / 180.0;
}

Curve joinCurves (params Curve[] curves)
{
  return Curve.JoinCurves(curves)[0];
}

Curve closeCurves(Curve curve1, Curve curve2)
{
  Point3d curve1Start = curve1.PointAtStart;
  Point3d curve1End = curve1.PointAtEnd;
  Point3d curve2Start = curve2.PointAtStart;
  Point3d curve2End = curve2.PointAtEnd;

  // Create lines between the endpoints
  Line connection1 = new Line(curve1Start, curve2Start);
  Line connection2 = new Line(curve1End, curve2End);

  return joinCurves(curve1, connection2.ToNurbsCurve(), curve2, connection1.ToNurbsCurve());
}

List<Curve> closeOuterCurves(double rimSize, double radius, params Curve[] outerCurves)
{

  List<Curve> boarderCurves = new List<Curve>();

  int[] dir = new int[]{-1,1};
  double[] rimSizes = new double[]{rimSize - radius * 2, rimSize};
  for(int i = 0; i < 2; i++)
  {

    double d = rimSizes[i];

    Curve curve = outerCurves[i];

    Point3d P1 = curve.PointAtStart;
    Point3d P2 = curve.PointAtEnd;
    Point3d P3 = new Point3d(P2.X, P2.Y + d * dir[i], 0);
    Point3d P4 = new Point3d(P1.X, P3.Y, 0);

    Polyline outerBoarder = new Polyline(new Point3d[]{P2, P3, P4, P1});


    Curve boarderCurve = joinCurves(curve, outerBoarder.ToNurbsCurve());
    boarderCurves.Add(boarderCurve);
  }

  return boarderCurves;
}

List<Curve> joinExtendBoundaryCurves(List<List<Curve>> channelBoundaryCurves, double extend)
{
  int[] dir = new int[]{-1,1};
  List<Curve> finalBoundaryCurves = new List<Curve>();

  foreach(List<Curve> OCurves in channelBoundaryCurves)
  {

    Curve JCurve = Curve.JoinCurves(OCurves)[0];
    Curve[] extensions = new Curve[2];

    for(int i = 0; i < 2; i++)
    {
      Point3d startPoint = JCurve.PointAtNormalizedLength(i);
      Line extension = new Line(startPoint, Vector3d.XAxis * dir[i], extend);
      extensions[i] = extension.ToNurbsCurve();
    }

    finalBoundaryCurves.Add(joinCurves(extensions[0], JCurve, extensions[1]));
  }

  return finalBoundaryCurves;
}

List<Point3d> getValveSpinePoints(int N, double H1, double H3, double L, double A1, double A2, out double h1)
{
  //create valve geometry world XY
  //this will then be translated to the planes
  double y1 = Math.Cos(A1) * L;
  double x1 = Math.Sin(A1) * L;

  double y2 = Math.Sin(A2) * H1;
  double x2 = Math.Cos(A2) * H1;

  Point3d P0 = Plane.WorldXY.Origin;
  Point3d P1 = new Point3d(P0.X, P0.Y + H1, 0);
  Point3d P2 = new Point3d(P0.X + x1, P0.Y - y1, 0);
  Point3d P3 = new Point3d(P0.X + x1 + x2, P0.Y - (y1 - y2), 0);
  Point3d P4 = new Point3d(P3.X, P1.Y, 0);

  //List < Point3d > valveSpinePoints = new List<Point3d>(P1, P2, P3, P4);
  List<Point3d> valveSpinePoints = new List<Point3d> (P1, P0, P2, P3, P4);

  h1 = Math.Abs(P0.Y - P2.Y) + H1;

  return valveSpinePoints;
```

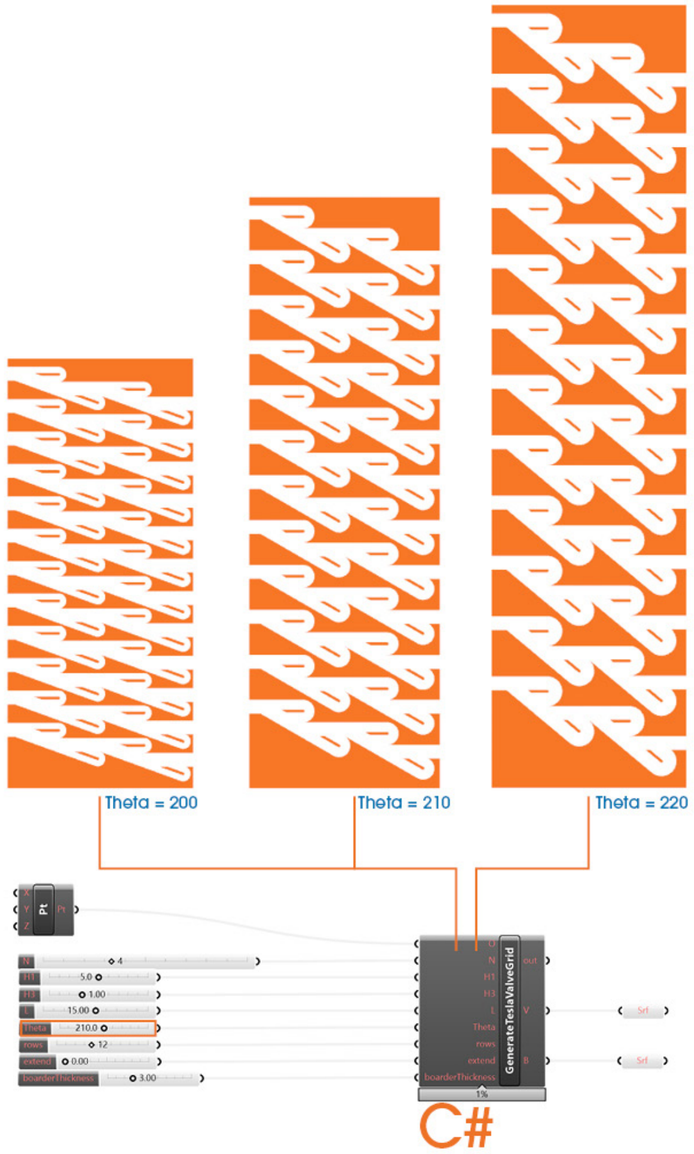

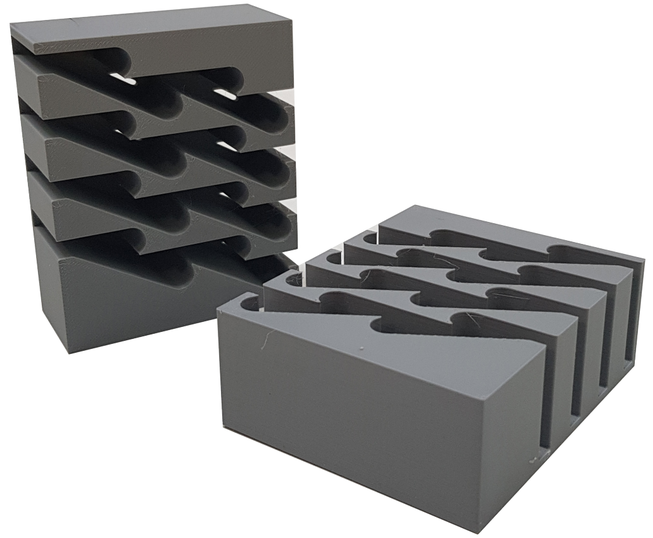

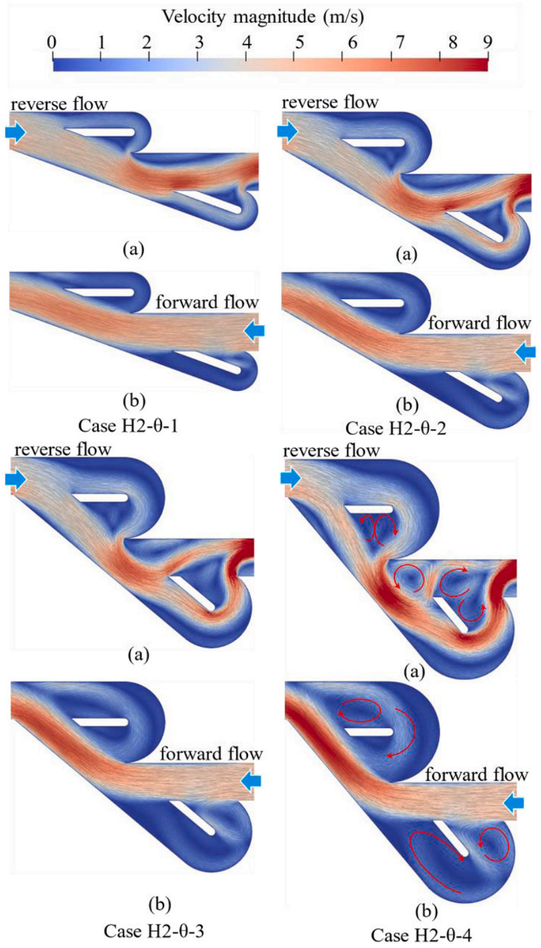

HU et al.

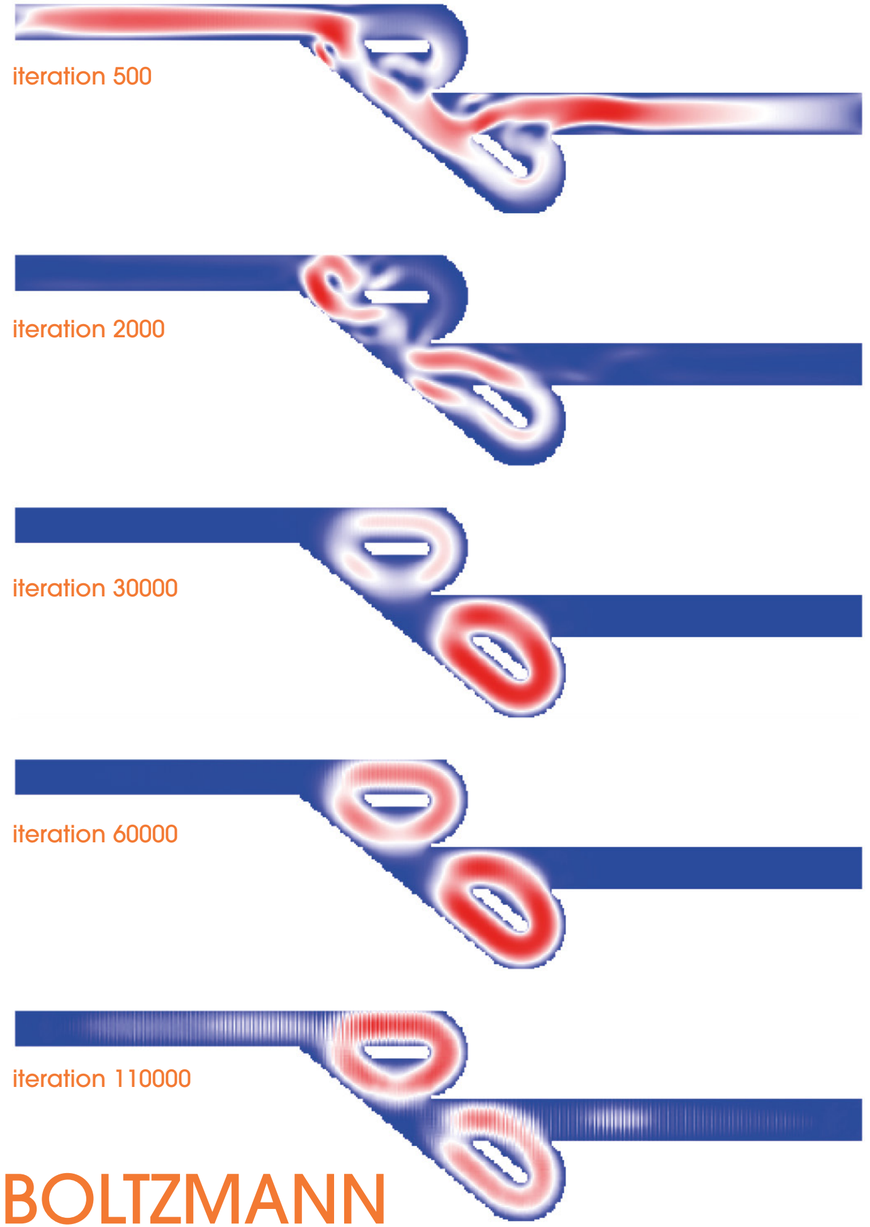

BOLTZMANN METHOD

```python
def main():

  plot_every = 500

  Nx = 400 #cells in x direction
  Ny = 100 #cells in y direction

  tau = 0.53 #viscosity and time step(?)
  Nt = 200000 #nr of iterations

  NL = 9 #lattice size
  cxs = np.array([0,0,1,1,1,0,-1,-1,-1]) #discrete velocities in x direction
  cys = np.array([0,1,1,0,-1,-1,-1,0,1]) #discrete velocities in y direction
  weights = np.array([4/9, 1/9, 1/36, 1/9, 1/36, 1/9, 1/36, 1/9, 1/36]) #can be interpreted


  F = np.ones((Ny, Nx, NL)) + .01 * np.random.randn(Ny, Nx, NL) #misoscopic velocities
  F[:,:,3] = 2.3

  context = data_array#((Ny, Nx), False) #create context for simulation, where False means

  print(context)

  #main loop
  for it in range(Nt):

    #F[:, -1, [6,7,8]] = F[:, -2, [6,7,8]]
    #F[:, 0, [2,3,4]] = F[:, 1, [2,3,4]]

    for i, cx, cy in zip(range(NL), cxs, cys):
      F[:,:,i] = np.roll(F[:,:,i], cx, axis=1)
      F[:,:,i] = np.roll(F[:,:,i], cy, axis=0)


    bndryF = F[context, :]
    bndryF = bndryF[:, [0,5,6,7,8,1,2,3,4]] #assigning opposite directions to particals col

    rho = np.sum(F,2)
    ux = np.sum(F * cxs, 2) / rho #macroscopic velocities
    uy[context] = 0

    Feq = np.zeros(F.shape)

    for i, cx, cy, w, in zip(range(NL), cxs, cys, weights):
      Feq[:,:,i] = \
      rho * w * (1 + 3 * (cx * ux + cy * uy) + 9 * (cx * ux + cy * uy)**2 / 2 - 3 * (ux**2 -

    F = F + -(1/tau) * (F - Feq)

    #calculate speed
    v = np.sqrt(ux**2 + uy**2)

    #calculate swirl
    dfydx = ux[2:, 1:-1] - ux[0:-2, 1:-1]
    dfxdy = uy[1:-1, 2:] - uy[1:-1, 0:-2]
    curl = dfydx - dfxdy

    if(it % plot_every == 0):

      print(it)

      data = v

      plt.cla()
      ux[context] = 0
      uy[context] = 0
      data[context] = np.nan
      data = np.ma.array(data, mask=context)
      plt.imshow(data, cmap='bwr')
      plt.imshow(~context, cmap='gray', alpha=0.0)
      plt.clim(-.1, .1)
      ax = plt.gca()
      ax.invert_yaxis()
      ax.get_xaxis().set_visible(False)
      ax.get_yaxis().set_visible(False)
      ax.set_aspect('equal')
      plt.pause(0.001)


if __name__ == "__main__":
  main()
```

VAFERI et al. (2023)

In the present study, the segregated approach, a pressure-based solver, was used to solve the governing equations. As implemented in COMSOL Multiphysics, this approach solves the velocity and pressure in one step. In contrast, other variables, such as temperature, are solved separately in other steps. This solver configuration allows for the decoupling and independent solution of different variables, which can help improve computational efficiency and convergence [43]. This research used a parallel direct sparse solver (PARDISO) in numerical simulations. The PARDISO solver is a state-of-the-art direct sparse solver in computational science and engineering. This solver is known for its efficiency, scalability, and ability to handle large-scale linear systems from various numerical simulations. It employs advanced algorithms and parallel computing techniques to efficiently handle the matrix factorization and solve the system of equations [44–46].

Diodicity is an essential factor that evaluates the Tesla valve's hydraulic performance. This parameter highlights the effectiveness of the valve based on the ratio of ΔP in reverse flow to forward flow in an identical flow rate [1]. By increasing diodicity, the performance of this device as a check valve will be improved. On the other hand, if this device is used in thermal applications, the thermal parameters of this device should be improved. The hydraulic and thermal diodicity of the Tesla valve were presented as PDR (pressure drop ratio) and TDR (thermal difference ratio), respectively, which were calculated as follows:

$$PDR = \frac{\Delta P_r}{\Delta P_f} = \frac{(P_{in} - P_{out})_r}{(P_{in} - P_{out})_f} \quad (8)$$

$$TDR = \frac{\Delta T_r}{\Delta T_f} = \frac{(T_{out} - T_{in})_r}{(T_{out} - T_{in})_f} \quad (9)$$

2.4. Mesh Independency

COMSOL Multiphysics was used to develop a two-dimensional triangular mesh type, as seen in Figure 3. In this simulation, the average mesh quality is 0.93. According to the statistics in Table 3, the thermal and hydraulic results of the numerical simulation with the number of 50.44 elements per 1 mm^2 are independent of the mesh. As can be seen, by increasing the mesh elements number to 88.58 per 1 mm^2, the time to solve the simulation increases by 56%, while the results related to the temperature difference and pressure drop change by 1.23% and 0.44%, respectively.

Figure 3. (**a**) Overview and (**b**) refined mesh near the divider baffle for the computational domain.

Table 3. Mesh independence validation for tesla valve with six-stage and reverse flow at conditions V = 0.2 m/s, T_{in} = 274.15 K, and T_w = 368.15 K.

Number of Elements per 1 mm^2	Solve Time	ΔT_r		ΔP_r	
		Value (K)	Difference (%)	Value (Pa)	Difference (%)
3.89	00:00:48	24.210	21.45	1905	7.15
22.68	00:03:38	29.320	4.87	1835	0.83
50.44	00:25:13	30.440	1.23	1828	0.44
88.58	00:39:27	30.820	-	1820	-

2.7. Artificial Neural Network Approach

One way to reduce computational time and save financial resources is by using black-box methods, which deal with input and output data without considering the possible physical processes. A practical approach in this field is the artificial neural network (ANN), inspired by the human nervous system. Neurons are the fundamental processors in neural networks, and each neuron may receive multiple inputs from other neurons and have one or more outputs based on its activity [33].

In this study, a separate three-layer structure was designed for each response (TDR and PDR), consisting of input, hidden, and output layers, as shown in Figure 5a. The input layer has three neurons that serve as the network's inputs. The hidden layer has four neurons, and the output layer contains one neuron. Based on the investigations conducted, it was observed that prediction models with fewer than four neurons in the hidden layer did not have satisfactory performance. Conversely, an excessive increase in neurons in this layer led to overfitting in the model's results. The activation functions must be derivable to perform the backpropagation function in model training. Therefore, the tangent-sigmoid activation function was used in hidden layer neurons, and the linear activation function was used in the output layer neuron to obtain the response value. To better understand the performance of each neuron in the hidden and output layers, Figure 5b was presented, which shows the performed calculations.

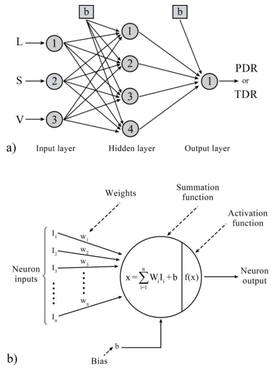

Figure 5. (**a**) The three-layer structure of the ANN network was used in the present work, (**b**) calculations performed in neurons of the hidden and output layers.

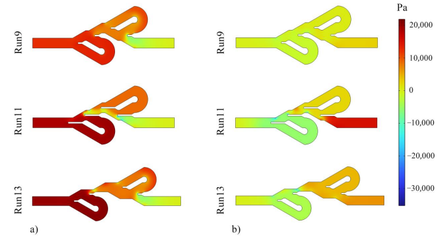

Figure 6. Pressure contours for (**a**) Tesla valves with fluid flow in the reverse direction and (**b**) Tesla valves with fluid flow in the forward direction.

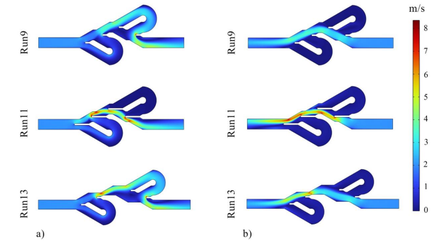

Figure 7. Velocity contours for (**a**) Tesla valves with fluid flow in the reverse direction and (**b**) Tesla valves with fluid flow in the forward direction.

Table 8. Nonlinear error functions for prediction models obtained by ANN method.

Error Function	Mathematical Form	ANN	
		TDR	PDR
R^2	$1 - \frac{\sum_{i=1}^{m}(r_{num} - r_{pred})_i}{\sum_{i=1}^{m}(r_{num} - \overline{r_{pred}})_i}$	0.991	0.992
MAE	$\frac{1}{m}\sum_{i=1}^{m}\left\lvert r_{pred} - r_{num}\right\rvert$	0.009	0.034
RMSE	$\sqrt{\frac{1}{m}\sum_{i=1}^{m}\left(r_{pred} - r_{num}\right)^2}$	0.021	0.095

In the following, the two-by-two effects of the variables on the responses were investigated according to Figure 10. Figure 10a shows that as L increases, the TDR value remains somewhat stable and then decreases, and the effect of this decrease is more significant at lower S. Figure 10b confirms this observation and shows that the effect of the L parameter on TDR is more pronounced at higher inlet velocities. Figure 10c reveals that the heat transfer capability of the Tesla valve increases with the increase of the inlet velocity (V), and this increase is more significant at lower S values. Furthermore, it can be seen that increasing S leads to a decrease in TDR. Turning to the three-dimensional plots for PDR response, Figure 10d shows that increasing L reduces PDR, and this effect is more pronounced at smaller S values. Figure 10e,f demonstrate that increasing the inlet velocity increases PDR, which is more prominent at smaller L and S values. It is worth mentioning that increasing the L parameter leads to a decrease in the diodicity of the Tesla valve.

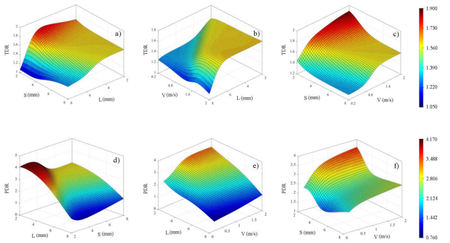

Figure 10. The relationship between (**a**) TDR, L, and S, (**b**) TDR, L, and V, (**c**) TDR, S, and V, (**d**) PDR, L, and S, (**e**) PDR, L, and V, (**f**) PDR, S, and V was illustrated in these 3D plots.

This section discusses the influence of variables on the performance of the Tesla valve and the analysis of these effects using streamlines (Figure 11). In this figure, the primary issue that can be noticed is that in the direction of forward movement, compression of the lines in the main channel is greater than bent channels, indicating a large fluid flow through this path. While in the reverse flow direction, the fluid flow is spread in all the channels of the Tesla valve. The effect of changing the divider baffle length on PDR can be observed

TO PRINT

OR

NOT TO PRINT?

TO PRINT
OR
NOT TO PRINT?

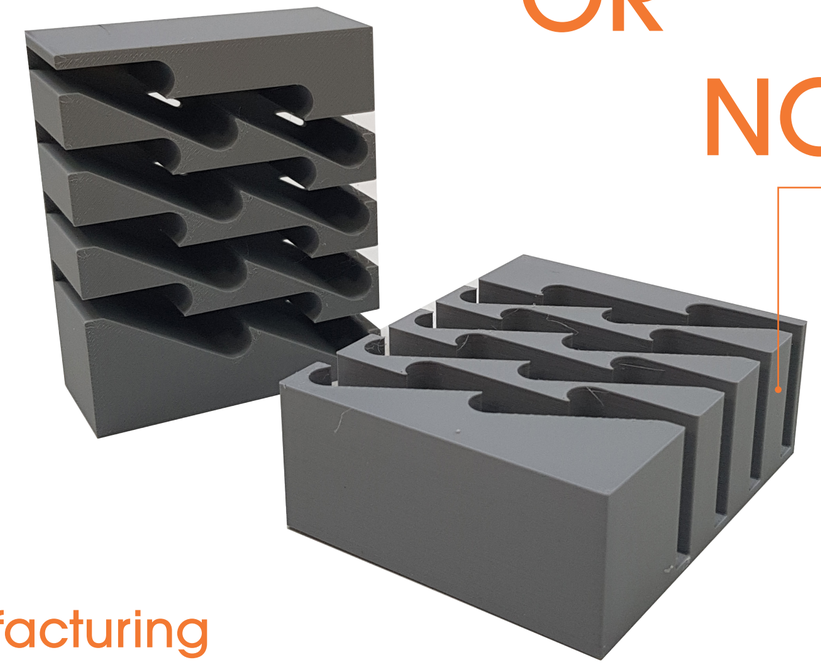

OBJECTIVES FOR 3DP

I Mass Customization
II Inherent Complexity
III Consolidated Manufacturing

1) IDENTIFY MULTI-FACETED ISSUES
2) IDENTIFY EXISTING SOLUTIONS
3) OPTIMIZE FOR 3D PRINTING?
4) INTEGRATE INTO HOLISTIC DESIGN

TO PRINT
OR
NOT TO PRINT?

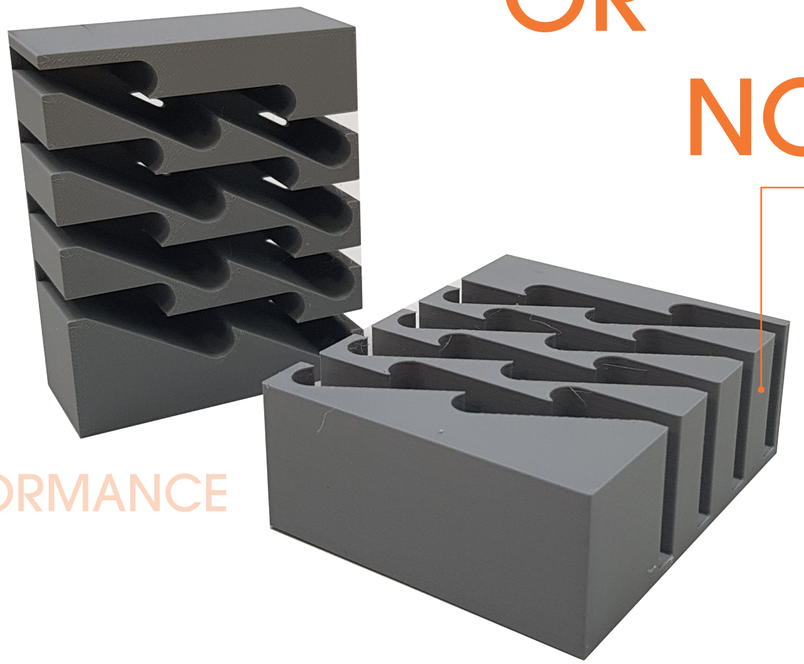

GENERAL OBJECTIVES

I HIGH ENERGY PERFORMANCE
II PASSIVE
III RESILIENT
IV AFFORDABLE
V SCALABLE
VI HOLLISTIC

1) IDENTIFY MULTI-FACETED ISSUES
2) IDENTIFY EXISTING SOLUTIONS
4) OPTIMIZE FOR 3D PRINTING?
4) INTEGRATE INTO HOLISTIC DESIGN

DIE CUTTING FROM FOAM

SUBTRACTIVE INSTEAD OF ADDITIVE

1) IDENTIFY MULTI-FACETED ISSUES
2) IDENTIFY EXISTING SOLUTIONS
3) OPTIMIZE FOR 3D PRINTING
4) INTEGRATE INTO HOLISTIC DESIGN

1) IDENTIFY MULTI-FACETED ISSUES

2) IDENTIFY EXISTING SOLUTIONS

3) OPTIMIZE FOR 3D PRINTING

4) INTEGRATE INTO HOLISTIC DESIGN

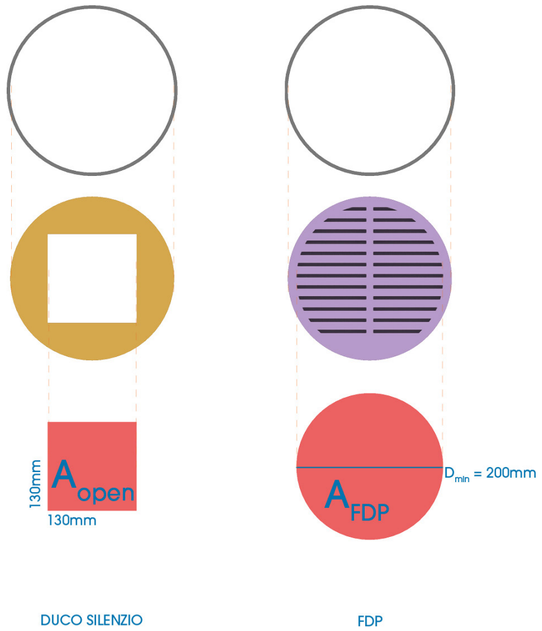

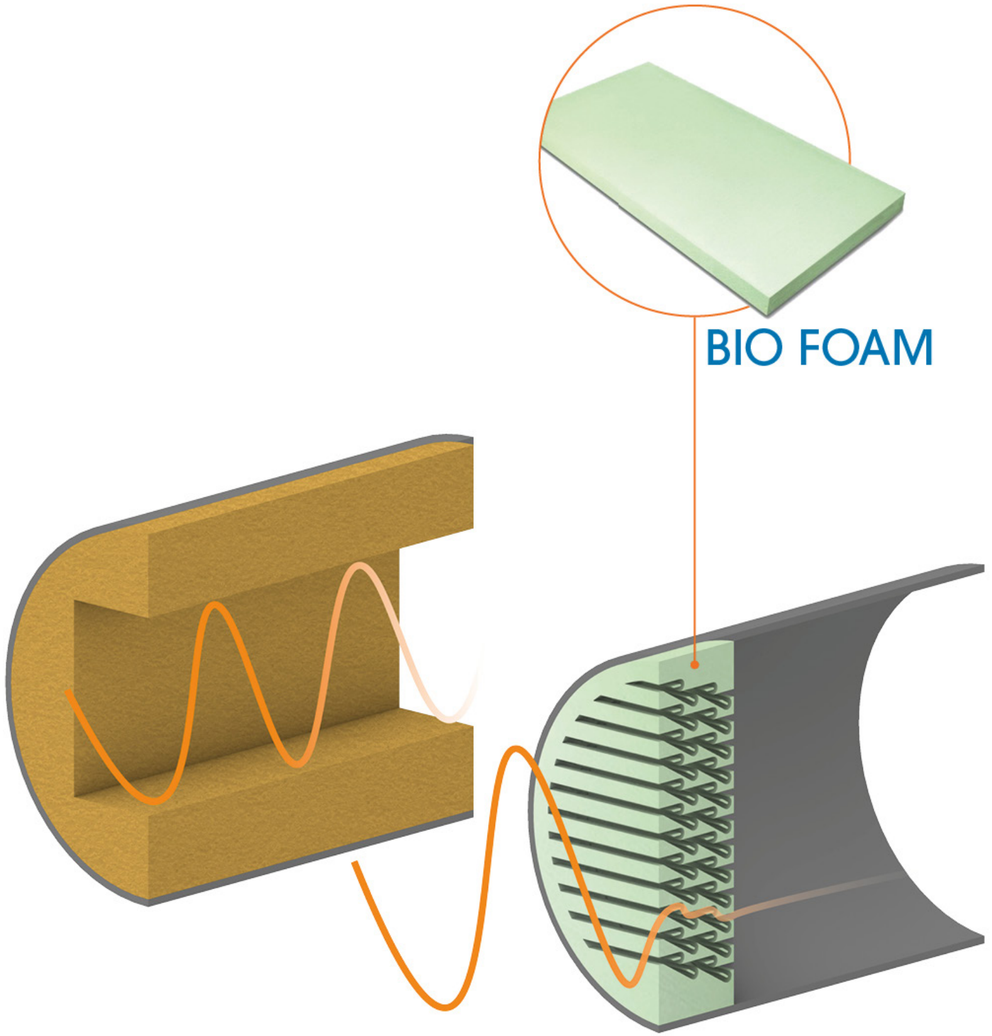

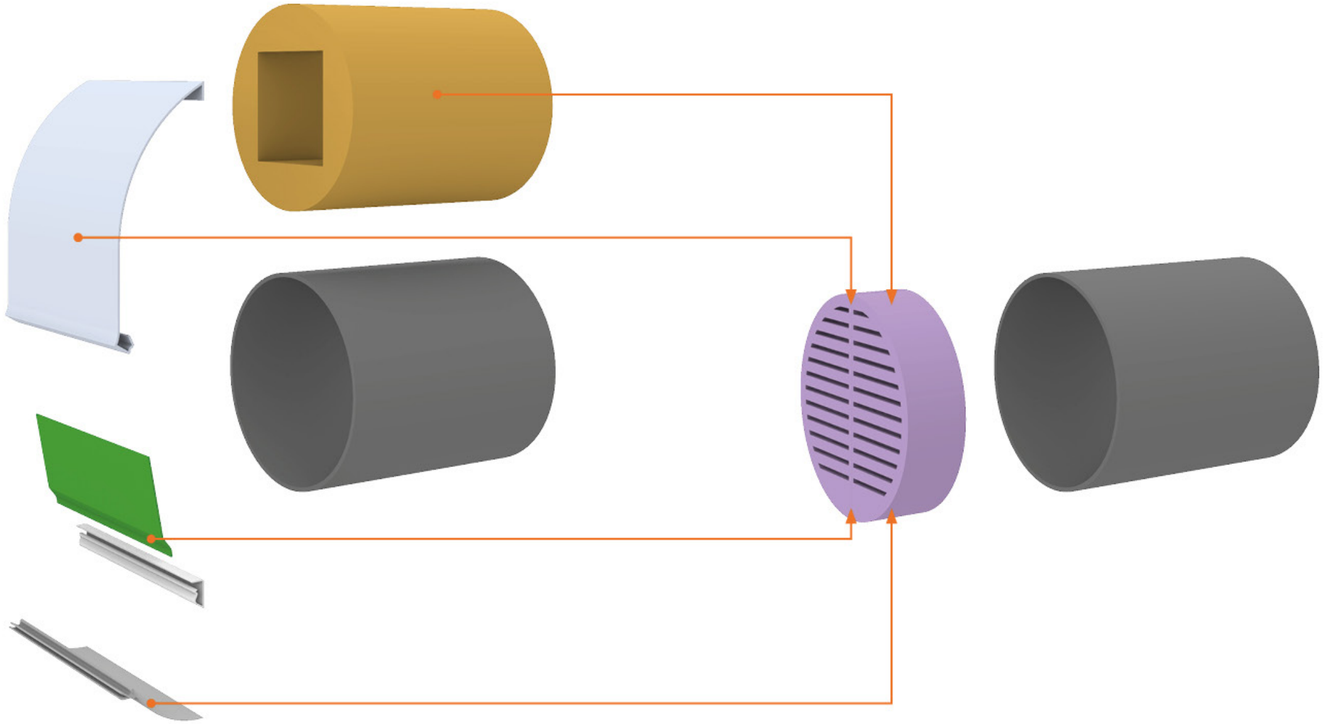

1) IDENTIFY MULTI-FACETED ISSUES

2) IDENTIFY EXISTING SOLUTIONS

3) OPTIMIZE FOR 3D PRINTING

4) INTEGRATE INTO HOLISTIC DESIGN

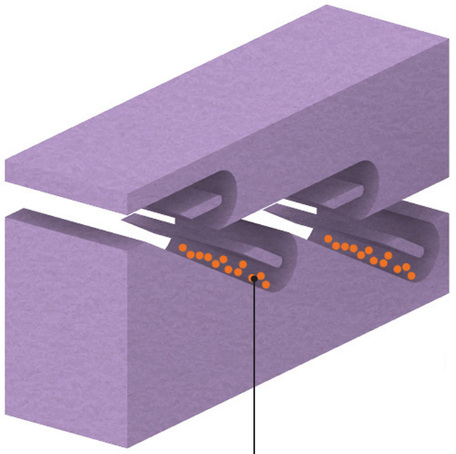

DIRT & PARTICLES

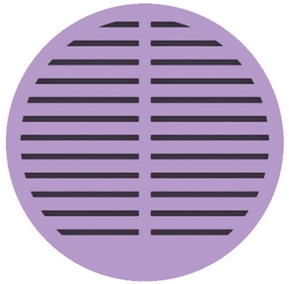

1) IDENTIFY MULTI-FACETED ISSUES

2) IDENTIFY EXISTING SOLUTIONS

3) OPTIMIZE FOR 3D PRINTING

4) INTEGRATE INTO HOLISTIC DESIGN

1) IDENTIFY MULTI-FACETED ISSUES

2) IDENTIFY EXISTING SOLUTIONS

3) OPTIMIZE FOR 3D PRINTING

4) INTEGRATE INTO HOLISTIC DESIGN

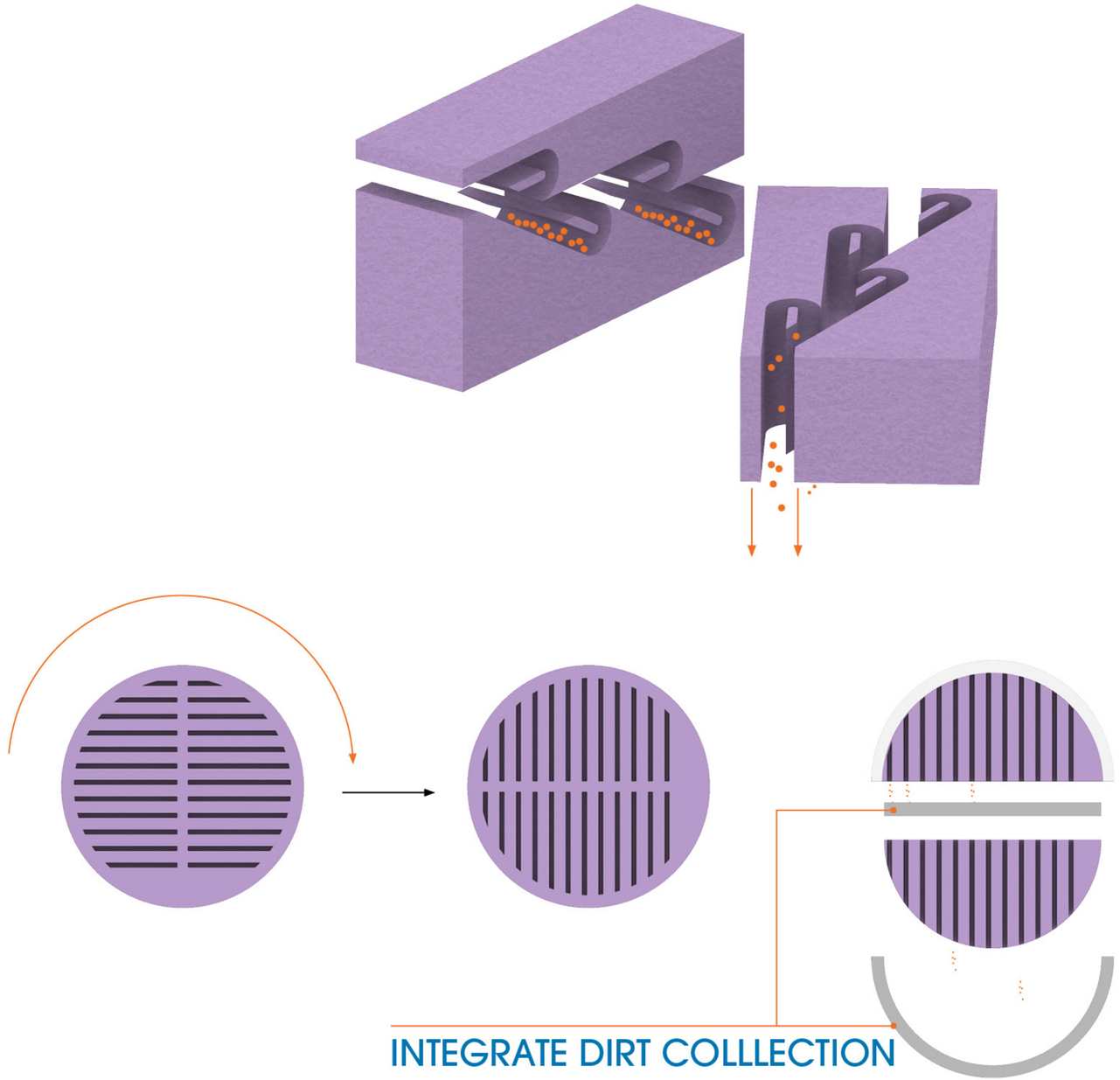

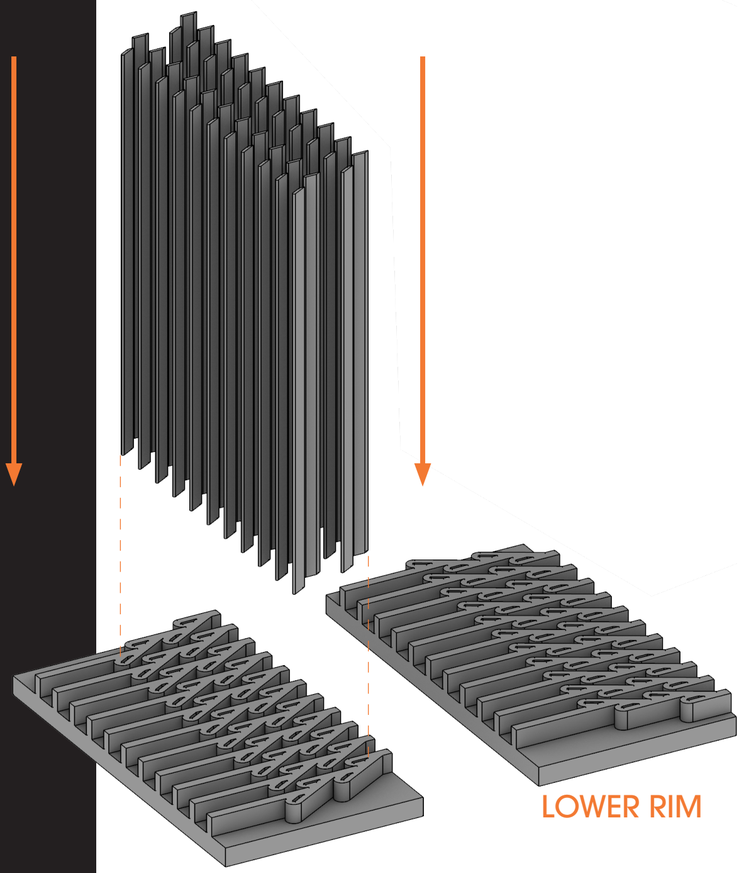

3D PRINTED RIMS AND BAFFLES

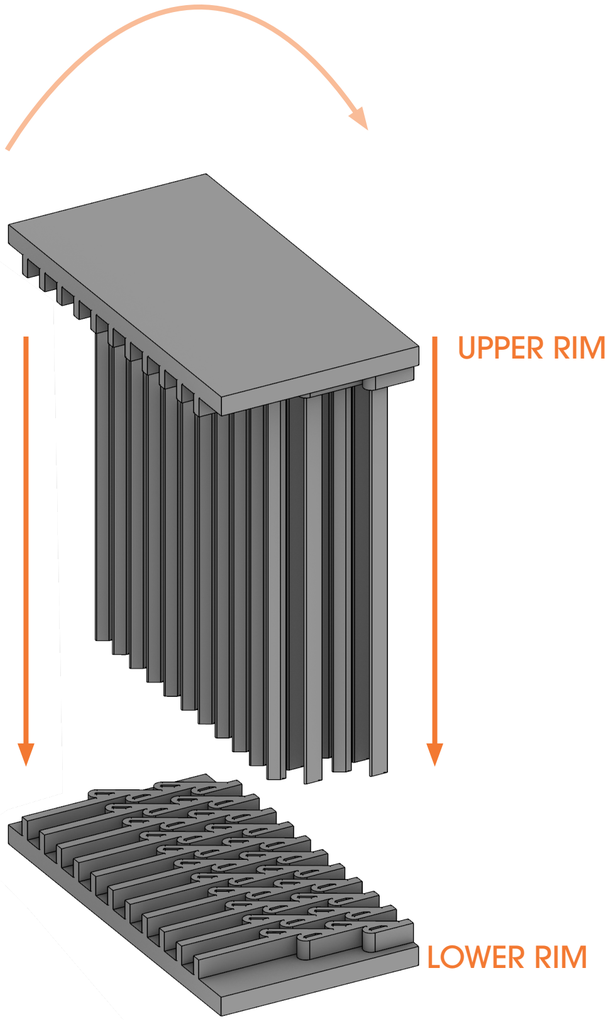

1) IDENTIFY MULTI-FACETED ISSUES
2) IDENTIFY EXISTING SOLUTIONS
3) OPTIMIZE FOR 3D PRINTING
4) INTEGRATE INTO HOLISTIC DESIGN

OBJECTIVES FOR 3DP

I Mass Customization
II Inherent Complexity
III Consolidated Manufacturing

GENERAL OBJECTIVES

I HIGH ENERGY PERFORMANCE
II PASSIVE
III RESILIENT
IV AFFORDABLE
V SCALABLE
VI HOLLISTIC

1) IDENTIFY MULTI-FACETED ISSUES
2) IDENTIFY EXISTING SOLUTIONS
3) OPTIMIZE FOR 3D PRINTING
4) INTEGRATE INTO HOLISTIC DESIGN

OBJECTIVES FOR 3DP

I Mass Customization
II Inherent Complexity
III Consolidated Manufacturing

GENERAL OBJECTIVES

I HIGH ENERGY PERFORMANCE
II PASSIVE
III RESILIENT
IV AFFORDABLE
V SCALABLE
VI HOLLISTIC

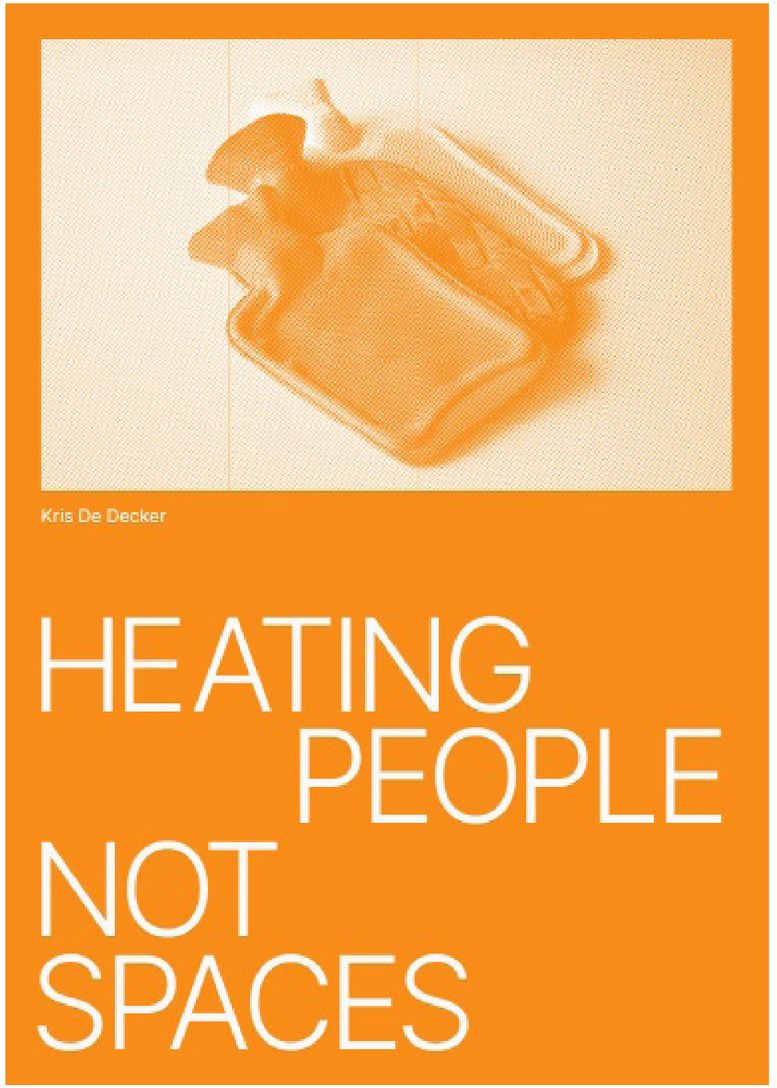

1) IDENTIFY MULTI-FACETED ISSUES
2) IDENTIFY EXISTING SOLUTIONS
3) OPTIMIZE FOR 3D PRINTING
4) INTEGRATE INTO HOLISTIC DESIGN

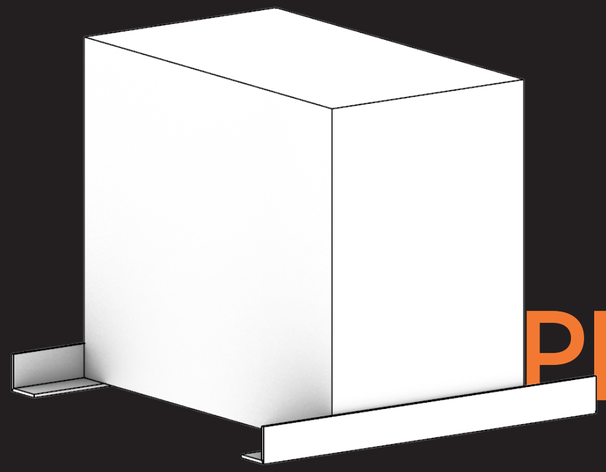

PRODUCTION

FOAM BLOCK

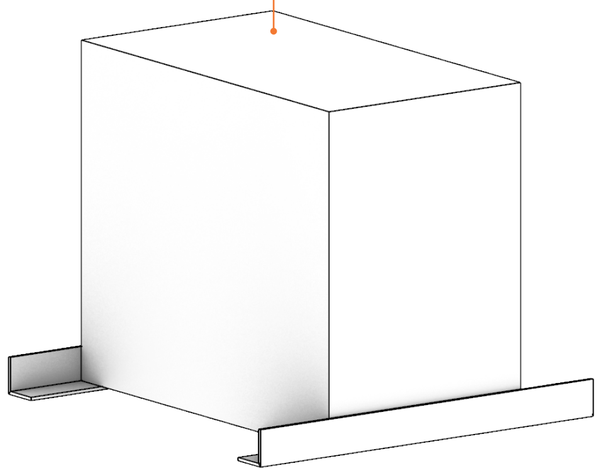

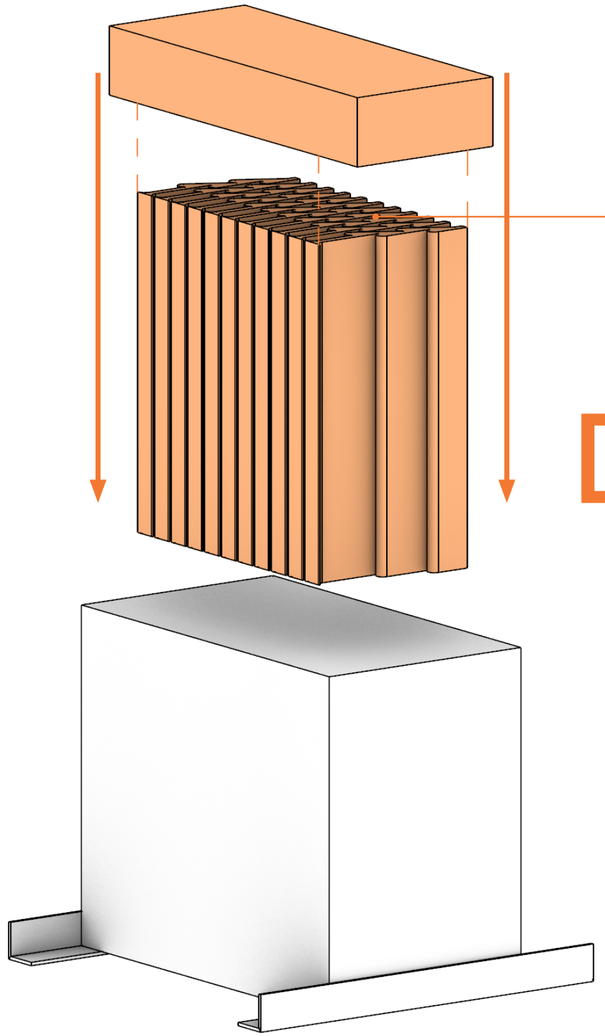

DIE CUTTER

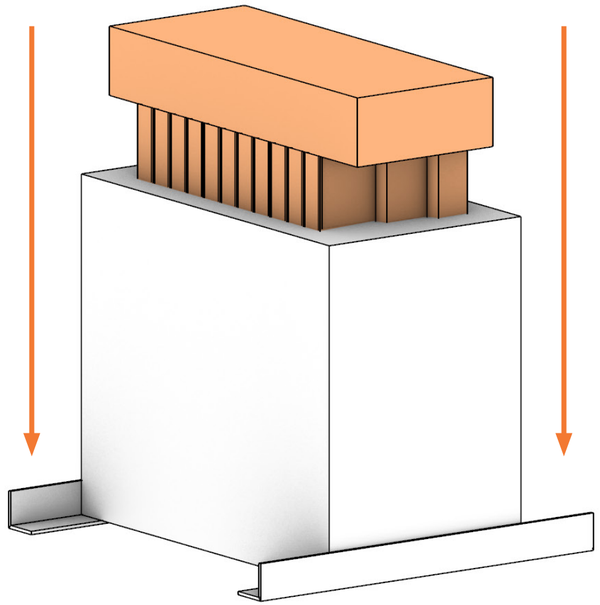

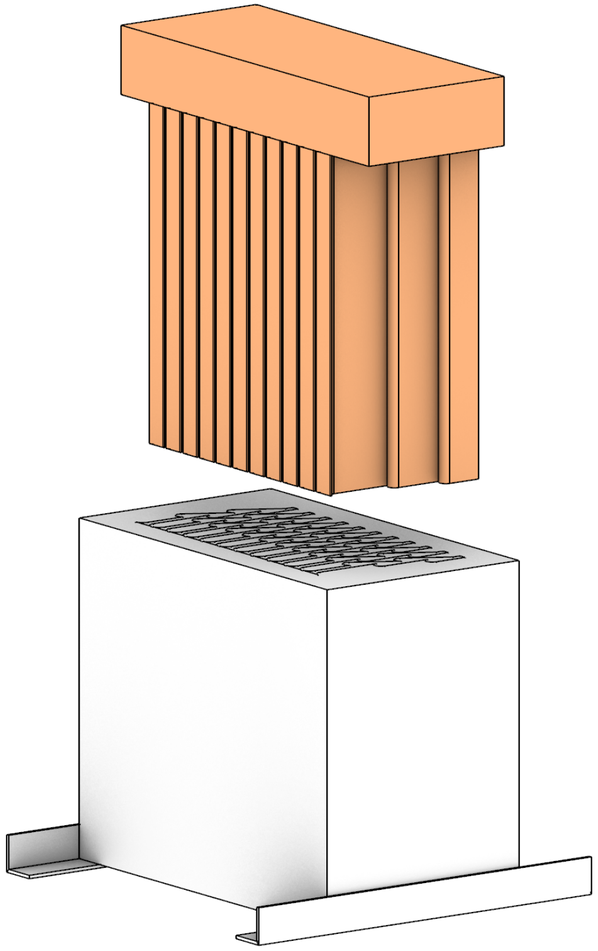

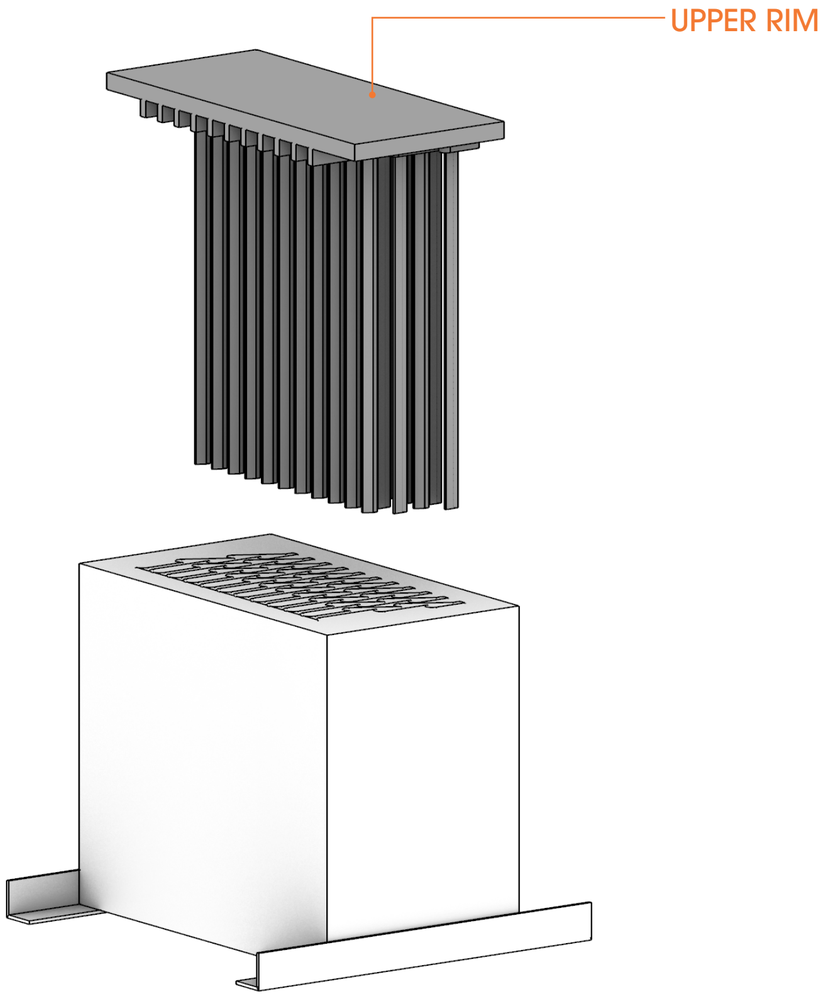
UPPER RIM

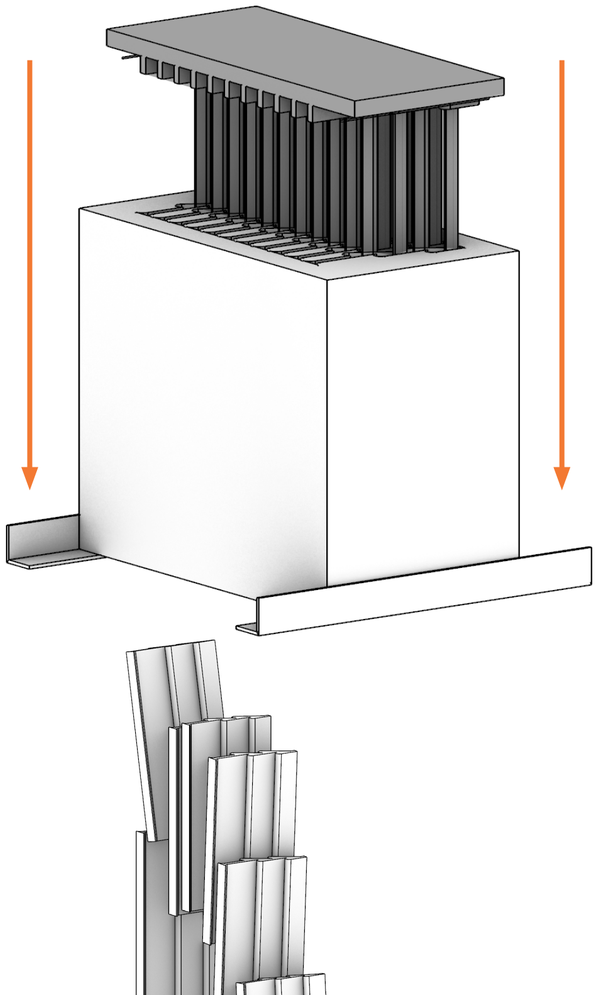

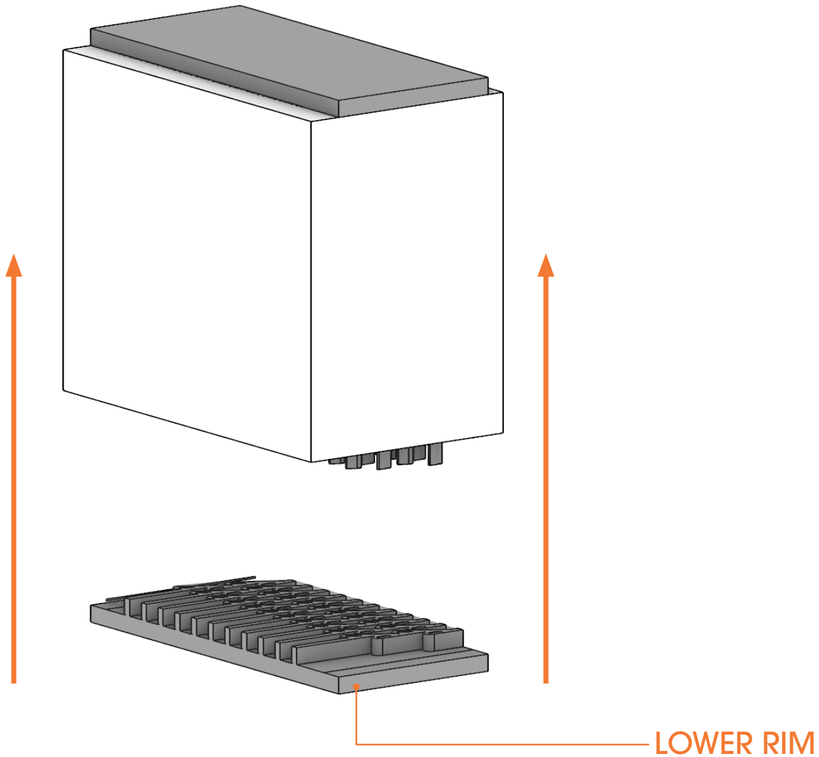
LOWER RIM

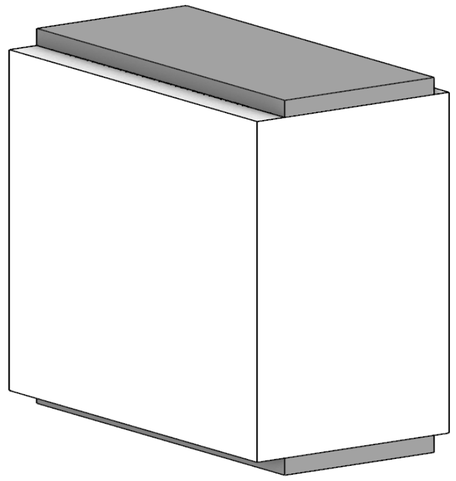

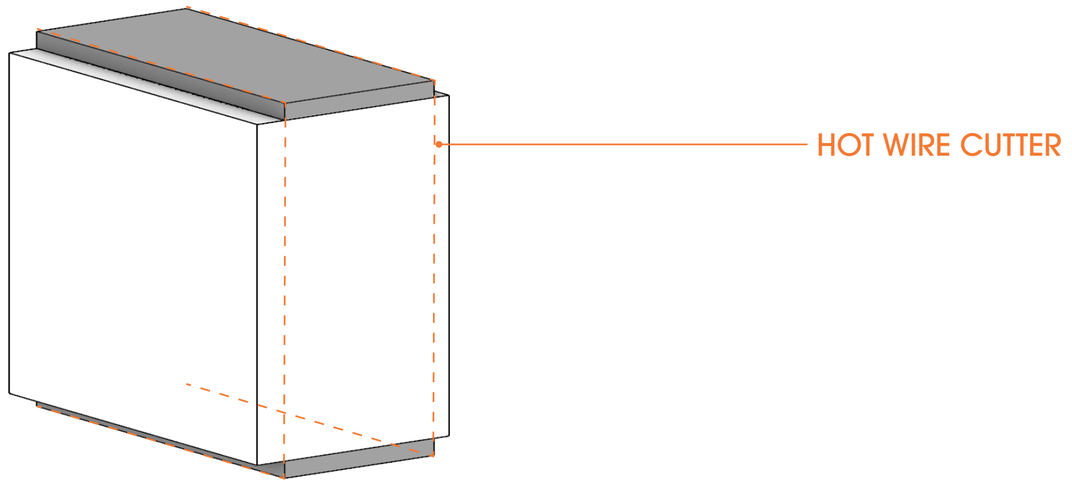
HOT WIRE CUTTER

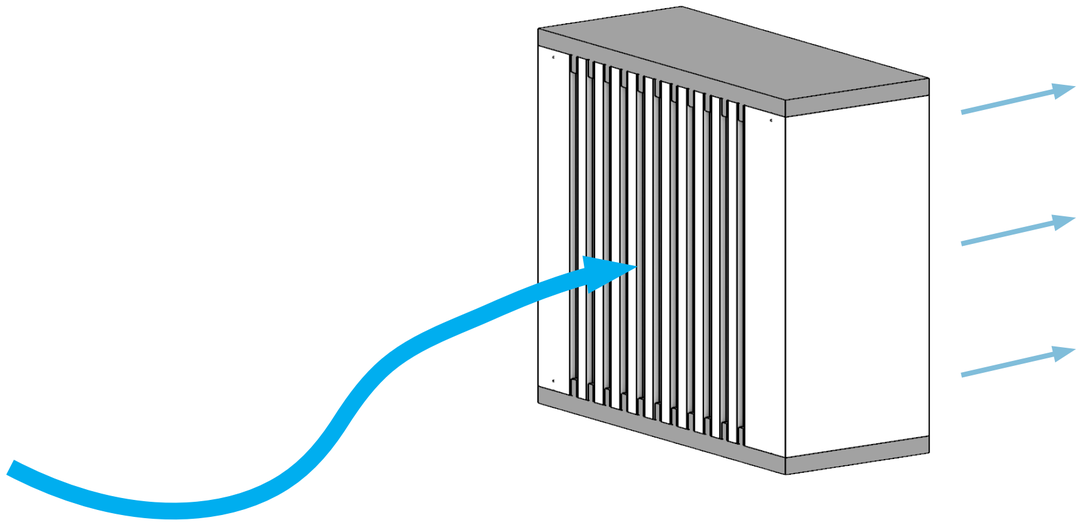

INTEGRATED 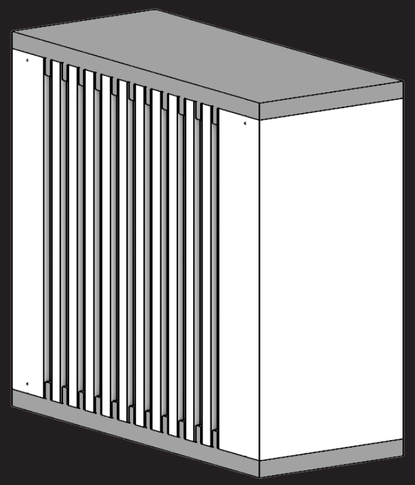 DESIGN

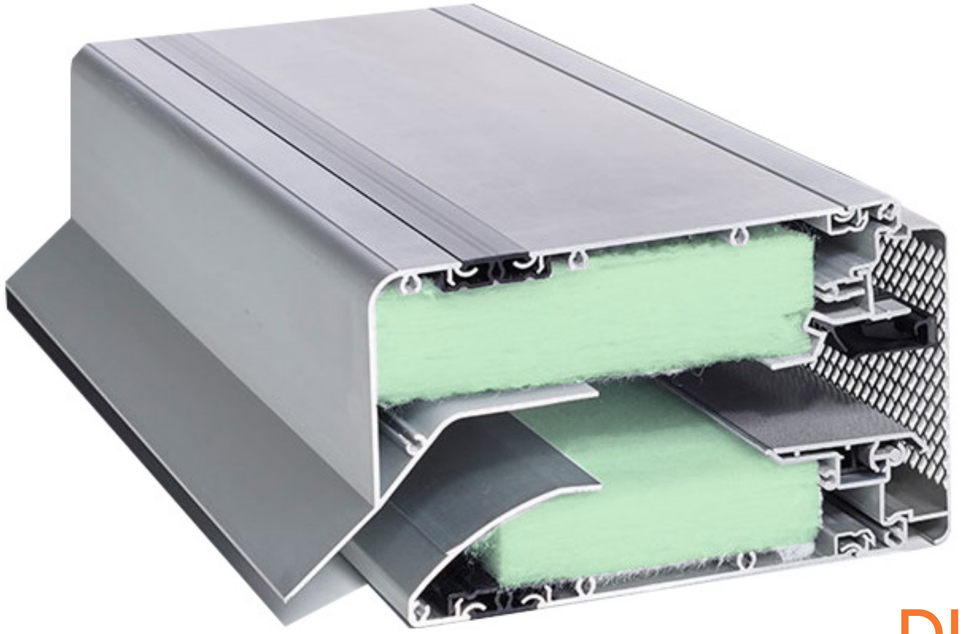

DUCO SKYMAX

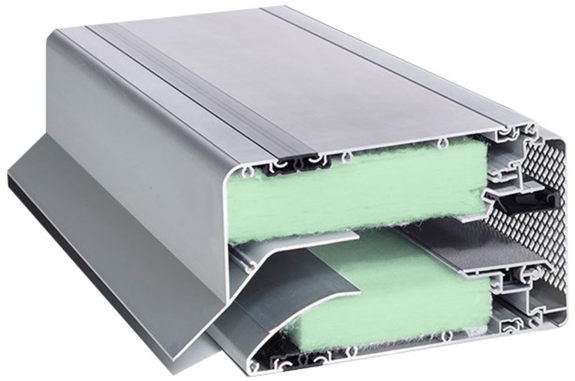

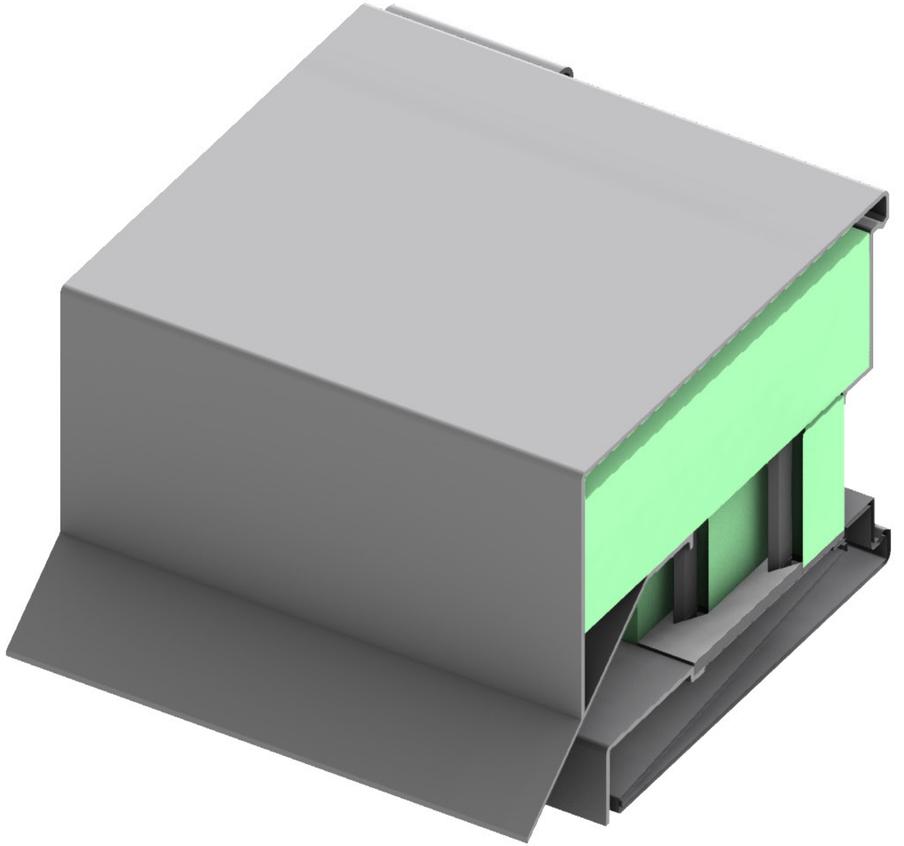

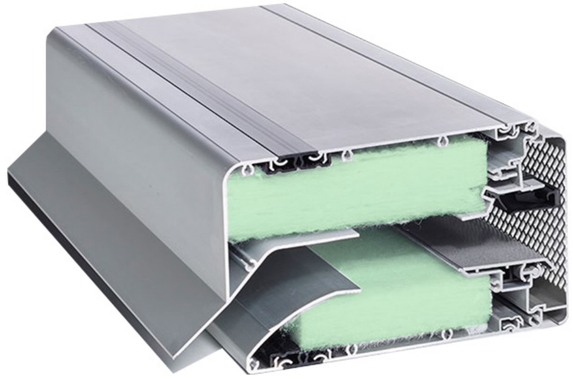

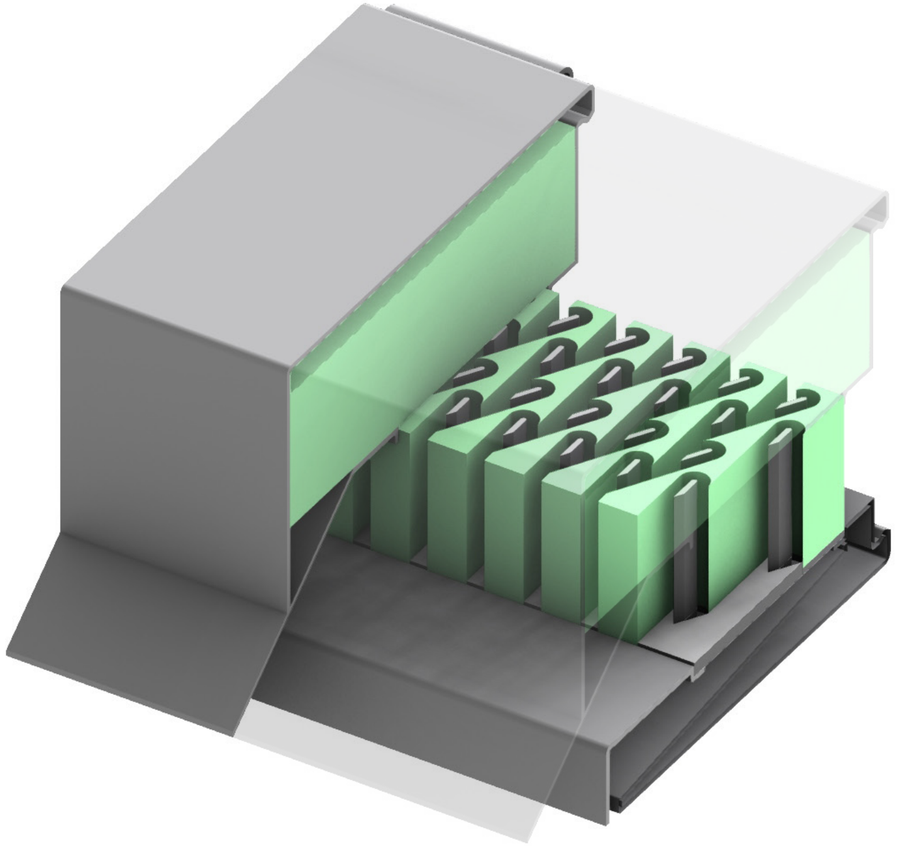

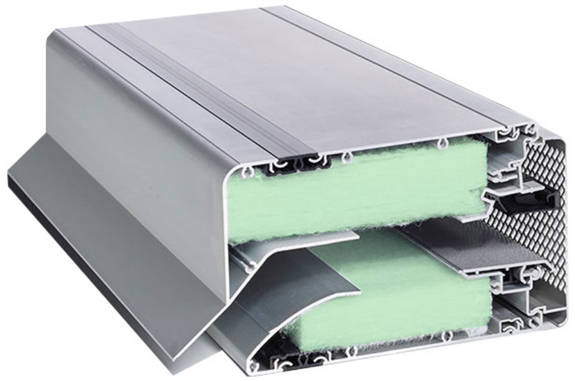

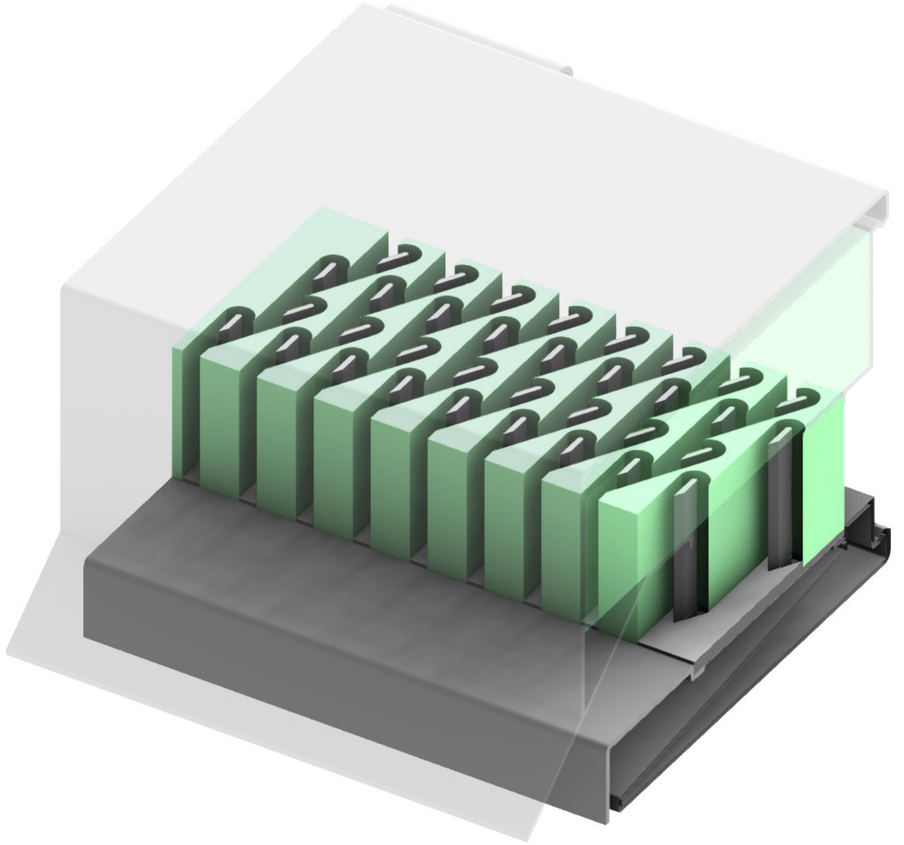

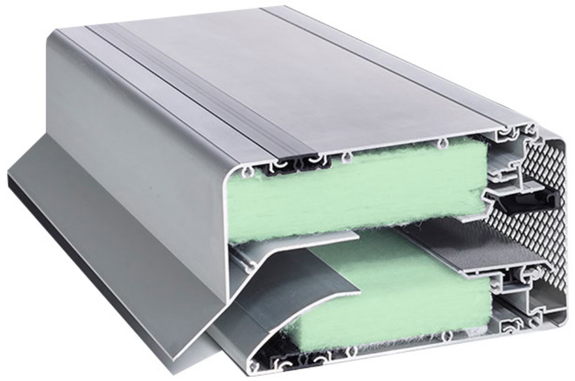

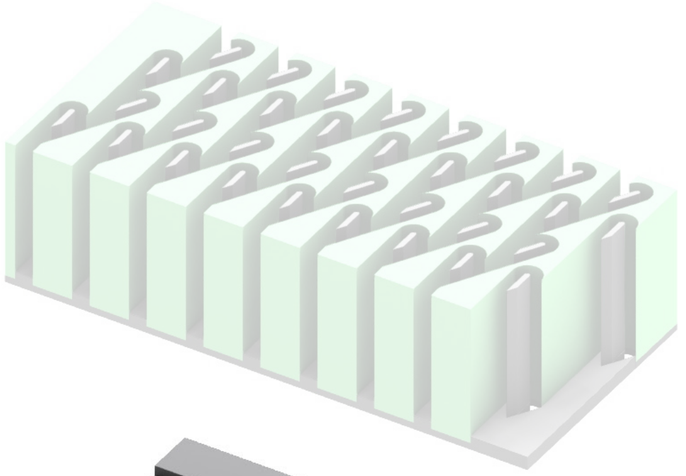

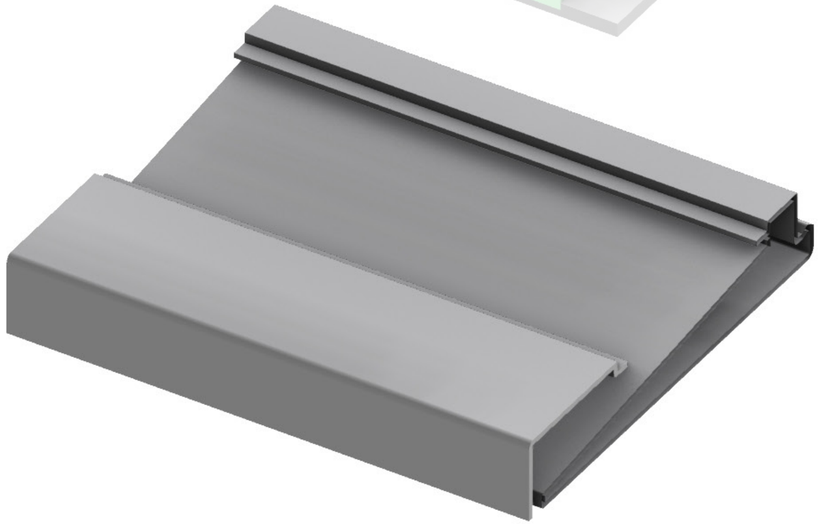

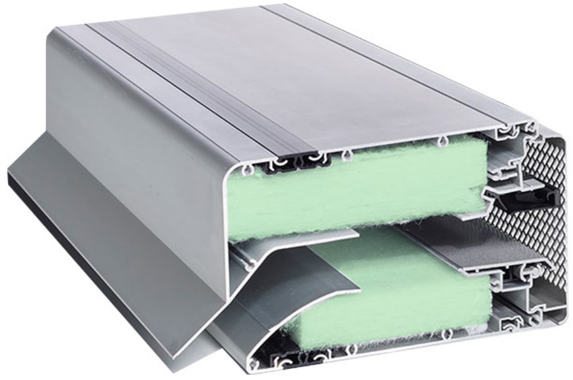

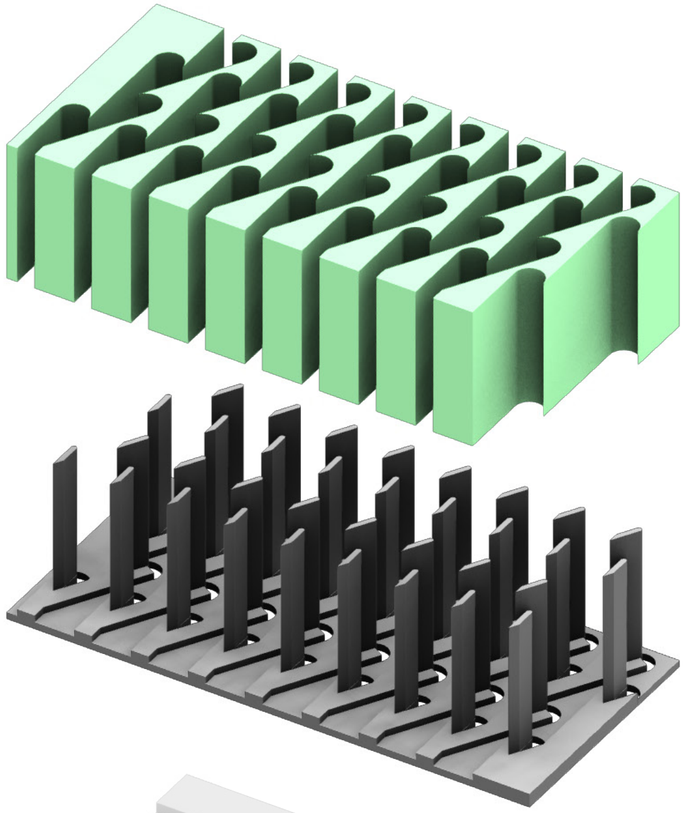

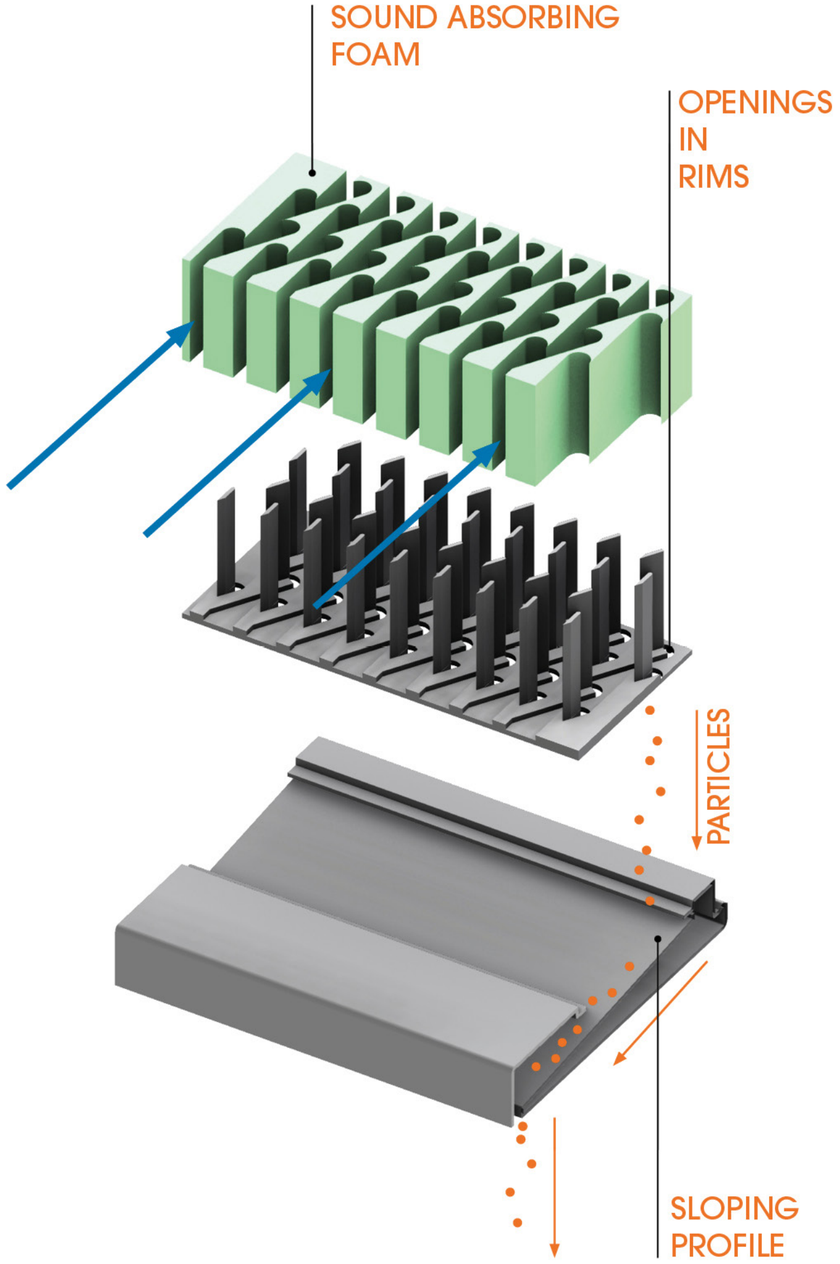
SOUND ABSORBING FOAM
OPENINGS IN RIMS
PARTICLES
SLOPING PROFILE

PRE HEATING?

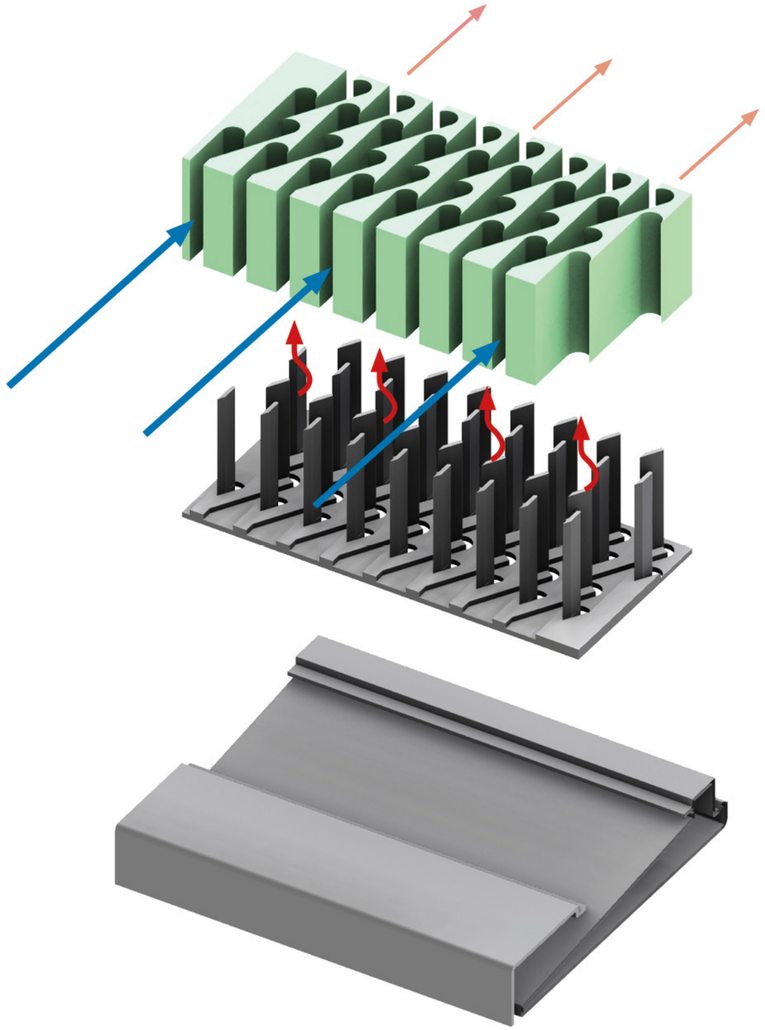

References

Acoustics & Noise Consultants. (2020). *Acoustics, ventilation and overheating residential design guide*. Retrieved January 22, 2024, from https://www.association-of-noise-consultants.co.uk/wp-content/uploads/2019/12/ANC-AVO-Residential-Design-Guide-January-2020-v1.1-1.pdf

Albanes, E., Biskos, G., Costi, M., & Biskos, G. (2022). Performance evaluation of a 3d-printed sharp-cut cyclone. *Environmental Science. Processes & Impacts*, *24*(8), 1173–1180. https://doi.org/10.1039/d2em00089j

Amfg. (2020, October 14). *10 of the biggest challenges in scaling additive manufacturing for production in 2020 [expert roundup]*. https://amfg.ai/2019/10/08/10-of-the-biggest-challenges-in-scaling-additive-manufacturing-for-production-expert-roundup/

Bao, Y., & Wang, H. (2022). Numerical study on flow and heat transfer characteristics of a novel tesla valve with improved evaluation method. *International Journal of Heat and Mass Transfer*, *187*, 122540. https://doi.org/10.1016/j.ijheatmasstransfer.2022.122540

Barnett, N., Costenaro, D., & Rohmund, I. (2017). *Direct and indirect impacts of robots on future electricity load* (tech. rep.). ACEEE.

Berardi, U., & Iannace, G. (2015). Acoustic characterization of natural fibers for sound absorption applications. *Building and Environment*, *94*, 840–852. https://doi.org/10.1016/j.buildenv.2015.05.029

Biler, A., Tavil, A., Su, Y., & Khan, N. (2018). A review of performance specifications and studies of trickle vents. *Buildings*, *8*(11), 152. https://doi.org/10.3390/buildings8110152

Böhm, S., Phi, H. B., Moriyama, A., Runge, E., Strehle, S., König, J., Cierpka, C., & Dittrich, L. (2022). Highly efficient passive tesla valves for microfluidic applications. *Microsystems & Nanoengineering*, *8*(1). https://doi.org/10.1038/s41378-022-00437-4

Buswell, R., Soar, R., Gibb, A., & Thorpe, T. (2005). The potential of freeform construction processes. *ResearchGate*. https://www.researchgate.net/publication/265994659_The_potential_of_freeform_construction_processes

Buswell, R. A., Soar, R., Gibb, A. G., & Thorpe, T. (2007). Freeform construction: Mega-scale rapid manufacturing for construction. *Automation in Construction*, *16*(2), 224–231. https://doi.org/10.1016/j.autcon.2006.05.002

Cambonie, T., Mbailassem, F., & Gourdon, E. (2018). Bending a quarter wavelength resonator: Curvature effects on sound absorption properties. *Applied Acoustics*, *131*, 87–102. https://doi.org/10.1016/j.apacoust.2017.10.004

Can, A., Leclercq, L., Lelong, J., & Botteldooren, D. (2010). Traffic noise spectrum analysis: Dynamic modeling vs. experimental observations. *Applied Acoustics*, *71*(8), 764–770. https://doi.org/10.1016/j.apacoust.2010.04.002

Cao, Z., Zhao, T., Wang, Y., Wang, H., Zhai, C., & Lv, W. (2020). Novel fluid diode plate for use within ventilation system based on tesla structure. *Building and Environment*, *185*, 107257. https://doi.org/10.1016/j.buildenv.2020.107257

Castaño-Rosa, R., Pelsmakers, S., Järventausta, H., Poutanen, J., Tähtinen, L., Rashidfarokhi, A., & Toivonen, S. (2022). Resilience in the built environment: Key characteristics for solutions to multiple crises. *Sustainable Cities and Society*, *87*, 104259. https://doi.org/10.1016/j.scs.2022.104259

Catapane, G., Petrone, G., Robin, O., & Verdière, K. (2023). Coiled quarter wavelength resonators for low-frequency sound absorption under plane wave and diffuse acoustic field excitations. *Applied Acoustics*, *209*, 109402. https://doi.org/10.1016/j.apacoust.2023.109402

Cauberg, J. (2005, August). *Natuurlijke ventilatie en infiltratie*. https://klimapedia.nl/module/natuurlijke-ventilatie-en-infiltratie/

Cauberg, J. (2013). *Drukverschillen over scheidingsconstructies* (Tech. Report No. Kennisbank Bouwfysica Dictaat ct 4220 Bouwfysica II). TU Delft, Faculteit Civiele Techniek en Geowetenschappen. https://klimapedia.nl/wp-content/uploads/2013/05/LU_11_drukverschillen_over_scheidingsconstructies.pdf

Daniël, D. (2021). *Reducing the indoor exposure to traffic emissions: Study and concept design of air purification systems for the façades of high-rise buildings in industrialized urban environments*. %5Curl%7Bhttps://repository.tudelft.nl/islandora/object/uuid:05813c2b-75dc-4c15-bfae-1dee9075157a?collection=education%7D

De Salis, M. H. F., Oldham, D., & Sharples, S. (2002). Noise control strategies for naturally ventilated buildings. *Building and Environment*, *37*(5), 471–484. https://doi.org/10.1016/s0360-1323(01)00047-6

Du, G., Alsenani, T. R., Kumar, J., Alkhalaf, S., Alkhalifah, T., Alturise, F., Almujibah, H., Znaidia, S., & Deifalla, A. (2023). Improving thermal and hydraulic performances through artificial neural networks: An optimization approach for tesla valve geometrical parameters. *Case Studies in Thermal Engineering*, *52*, 103670. https://doi.org/10.1016/j.csite.2023.103670

Duco. (2024). Silenzio zr (ak).

Eco traject. (2016). *Slimme technieken ventilatiesysteem c*. https://cdn.nimbu.io/s/4tn7vz5/assets/5.2.1%20Technieken%20-%20ventilatiesysteem%20C.pdf

El-Sayegh, S. M., Romdhane, L., & Manjikian, S. (2020). A critical review of 3d printing in construction: Benefits, challenges, and risks. *Archives of Civil and Mechanical Engineering*, *20*(2). https://doi.org/10.1007/s43452-020-00038-w

Engineeringtoolbox. (2024a). Air duct components - minor dynamic loss coefficients. Retrieved April 12, 2024, from https://www.engineeringtoolbox.com/minor-loss-air-ducts-fittings-d_208.html

Engineeringtoolbox. (2024b). Fluid flow - hydraulic diameter. Retrieved April 23, 2024, from https://www.engineeringtoolbox.com/hydraulic-equivalent-diameter-d_458.html

European Parliament. (2023). Energy performance of buildings [Geraadpleegd op 28 januari 2024].

Fadl, A., Zhang, Z., Geller, S., Tölke, J., Krafczyk, M., & Meyer, D. (2009). The effect of the microfluidic diodicity on the efficiency of valve-less rectification micropumps using lattice boltzmann method. *Microsystem Technologies*, *15*(9), 1379–1387. https://doi.org/10.1007/s00542-009-0901-7

Federation of European HVAC associations [REHVA]. (2012). *Existing buildings. building codes, ventilation standards and ventilation in europe* (tech. rep.) (Retrieved January 22, 2024). REHVA. https://www.rehva.eu/fileadmin/EU_projects/HealthVent/HealthVent_WP5_-_Final_Report.pdf

Field, C. (2004–August 25). The latest developments of an attenuator for naturally ventilated buildings. *Proceedings of the 33rd International Congress and Exposition on Noise Control Engineering*. https://www.researchgate.net/publication/308973203_The_Latest_Developments_of_an_Attenuator_For_Naturally_Ventilated_Buildings

Filamentives. (n.d.). How sustainable is pla 3d printer filament?

Formlabs. (n.d.). Guide to resin 3d printers: Sla vs. dlp vs. msla vs. lcd.

Formlabs. (n.d.). 3d printing technology comparison: Fdm vs. sla vs. sls. https://formlabs.com/eu/blog/fdm-vs-sla-vs-sls-how-to-choose-the-right-3d-printing-technology/

Ganji, D., & Kachapi, S. H. H. (2015). Natural, mixed, and forced convection in nanofluid. In *Elsevier ebooks* (pp. 205–269). https://doi.org/10.1016/b978-0-323-35237-6.00006-6

Gebler, M., Uiterkamp, A. J. M. S., & Visser, C. (2014). A global sustainability perspective on 3d printing technologies. *Energy Policy*, *74*, 158–167. https://doi.org/10.1016/j.enpol.2014.08.033

Ghaffar, S. H., Corker, J., & Fan, M. (2018). Additive manufacturing technology and its implementation in construction as an eco-innovative solution. *Automation in Construction*, *93*, 1–11. https://doi.org/10.1016/j.autcon.2018.05.005

Gibson, I., Rosen, D. W., Stucker, B., & Khorasani, M. (2020). Design for additive manufacturing. In *Springer ebooks* (pp. 555–607). https://doi.org/10.1007/978-3-030-56127-7_19

Griffin, M. (2024, February). Is 3d printer resin toxic? all you need to know.

Healthy Buildings Program. (2017). *The 9 foundations of a healthy building* (tech. rep.). HBP. https://forhealth.org/9_Foundations_of_a_Healthy_Building.February_2017.pdf

Hickel, J. (2021). *Less is more*. Windmill Books.

Hinchy, E. P. (2019). Design for additive manufacturing. In *Springer ebooks* (pp. 23–50). https://doi.org/10.1007/978-3-030-24532-0_2

Hu, H., Son, I., Kikumoto, H., Zhang, B., & Hayashi, K. (2024). Improving tesla valve shape within fluid diode plates for building ventilation. *Building and Environment*, *252*, 111259. https://doi.org/10.1016/j.buildenv.2024.111259

Huston, M. (2024). *Architecture and the environmental impact of artificial complexity*. Retrieved May 6, 2024, from https://www.archdaily.com/957549/architecture-and-the-environmental-impact-of-artificial-complexity

International Energy Agency. (2021). Net zero by 2050 [License: CC BY 4.0].

International Energy Agency. (2022, September). Renovation of near 20% of existing building stock to zero-carbon-ready by 2030 is ambitious but necessary – analysis.

International Energy Agency. (2023). *Tracking clean energy progress 2023* (tech. rep.) (License: CC BY 4.0 via: https://www.iea.org/energy-system/buildings). IEA. Paris. https://www.iea.org/reports/tracking-clean-energy-progress-2023

International Energy Agency (IEA). (2022). Technology and innovation pathways for zero-carbon-ready buildings by 2030 [Licence: CC BY 4.0].

Jared, B. H., Aguiló, M. A., Beghini, L. L., Boyce, B., Clark, B. W., Cook, A., Kaehr, B., & Robbins, J. (2017). Additive manufacturing: Toward holistic design. *Scripta Materialia*, *135*, 141–147. https://doi.org/10.1016/j.scriptamat.2017.02.029

Khajavi, S. H., Tetik, M., Mohite, A., Peltokorpi, A., Li, M., Weng, Y., & Holmström, J. (2021). Additive manufacturing in the construction industry: The comparative competitiveness of 3d concrete printing. *Applied Sciences*, *11*(9), 3865. https://doi.org/10.3390/app11093865

Kim, K., Park, K., & Jeon, H.-W. (2022). The impact of design complexity on additive manufacturing performance. *IFIP Advances in Information and Communication Technology*, 227–234. https://doi.org/10.1007/978-3-031-16407-1_27

Leschok, M., Cheibas, I., Piccioni, V., Seshadri, B., Schlueter, A., Gramazio, F., Köhler, M., & Dillenburger, B. (2023). 3d printing facades: Design, fabrication, and assessment methods. *Automation in Construction*, *152*, 104918. https://doi.org/10.1016/j.autcon.2023.104918

Liu, Z., Shao, W., Sun, Y., & Sun, B. (2022). Scaling law of the one-direction flow characteristics of symmetric tesla valve. *Engineering Applications of Computational Fluid Mechanics*, *16*(1), 441–452. https://doi.org/10.1080/19942060.2021.2023648

McNeel. (n.d.). Compute.rhino3d/src/ghhops-server-py [https://github.com/mcneel/compute.rhino3d/tree/8.x/src/ghhops-server-py].

Mocz, P. (2022, November). *Create your own lattice boltzmann simulation (with python)*. Medium. https://medium.com/swlh/create-your-own-lattice-boltzmann-simulation-with-python-8759e8b53b1c

NEN. (2013). *Bouwbesluit ventilatie* (tech. rep.). Nederlands Normalisatie-instituut.

Neutrium. (n.d.). Hydraulic diameter [Neutrium. Accessed on: 23/04/2024]. https://neutrium.net/fluid-flow/hydraulic-diameter/

Niaki, M. K., Torabi, S. A., & Nonino, F. (2019). Why manufacturers adopt additive manufacturing technologies: The role of sustainability. *Journal of Cleaner Production*, *222*, 381–392. https://doi.org/10.1016/j.jclepro.2019.03.019

Nijeboer & Hage. (n.d.). *Drukverschillen bij natuurlijke ventilatie, type c* (Tech Report). https://www.duco.eu/Wes/CDN/1/Attachments/Notitie%20drukverschil%20bij%20natuurlijk%20ventileren_3_635984962745408705.pdf

Ortiz, M. (2022, April). Simple lattice-boltzmann simulator in python | computational fluid dynamics for beginners. https://www.youtube.com/watch?v=JFWqCQHg-Hs

Peels, J. (2023, October). RIP 3D Printing: 1987 2023, Complexity is Expensive [3DPrint.com | the Voice of 3D Printing / Additive Manufacturing].

Peng, C., Xu, J., Kumar, J., Almujibah, H., Ali, H., Alkhalifah, T., Alkhalaf, S., Alturise, F., & Ghandour, R. (2023). Improving efficiency and optimizing heat transfer in a novel tesla valve through multi-layer perceptron models. *Case Studies in Thermal Engineering*, *49*, 103391. https://doi.org/10.1016/j.csite.2023.103391

Pleysier, I. A., & Vos, M. (2017). Luchttransport door constructies. %5Curl%7Bhttps://klimapedia.nl/wp-content/uploads/2017/07/WV952-H6-Luchttransport-2016-2017-v1.0.pdf%7D

Pradel, P., Bibb, R., Zhu, Z., & Moultrie, J. (2017). Complexity is not for free: The impact of component complexity on additive manufacturing build time. *ResearchGate*. https://www.researchgate.net/publication/327424268_Complexity_is_not_for_free_the_impact_of_component_complexity_on_additive_manufacturing_build_time

Purwidyantri, A., & Prabowo, B. A. (2023). Tesla valve microfluidics: The rise of forgotten technology. *Chemosensors*, *11*(4), 256. https://doi.org/10.3390/chemosensors11040256

Rashid, A. A., Al-Ghamdi, S. G., & Koç, M. (2020). Additive manufacturing: Technology, applications, markets, and opportunities for the built environment. *Automation in Construction*, *118*, 103268. https://doi.org/10.1016/j.autcon.2020.103268

Rijksgebouwendienst, Bureau Bouwfysica, Afdeling Onderzoek en Ontwikkeling. (1984, February). *Uitgangspunten bij de vaststelling van de aan de luchtdoorlatendheid van gevels te stellen eisen* (Internal Report). Rijksgebouwendienst. 's-Gravenhage.

Schork, T., Titchkosky, N., Bickerton, C., Reinhardt, D., Bennett, M., Pigram, D., & Makki, M. (2021). The geometry of air: Large-scale multi-colour robotic additive fabrication for air-diffusion systems. *Construction Robotics*, *5*(1), 49–61. https://doi.org/10.1007/s41693-021-00054-z

Setaki, F., Tian, F., Turrin, M., Tenpierik, M., Nijs, L., & Van Timmeren, A. (2023). 3d-printed sound absorbers: Compact and customisable at broadband frequencies. *Architecture, Structures and Construction*, *3*(2), 205–215. https://doi.org/10.1007/s44150-023-00086-9

SimScale. (2023, November). The lattice boltzmann method (lbm) in cfd | simwiki | simscale [Retrieved on January 22, 2024].

Solidator. (2023, December). Msla - what are the advantages of msla over sla? solidator resin 3d printer. https://solidator.com/en/msla-sla-comparison/

Strau, H. (2017). Am envelope. the potential of additive manufacturing for facade constructions. *DOAJ (DOAJ: Directory of Open Access Journals)*. https://doi.org/10.7480/abe.2013.1

Tang, S. K. (2017). A review on natural ventilation-enabling façade noise control devices for congested high-rise cities. *Applied Sciences*, *7*(2), 175. https://doi.org/10.3390/app7020175

TCPoly. (2021). PANELTM FOR HEAT RECOVERY IN COMMERCIAL BUILDINGS.

Tedeschi, A. (2014). *Aad algorithms-aided design | parametric strategies using grasshopper®*. Edizioni Le Penseur - Le Penseur Publisher. https://www.lepenseur.it/books-and-training/aad-algorithms-aided-design-parametric-strategies-using-grasshopper/

Vaferi, K., Vajdi, M., Shadian, A., Ahadnejad, H., Moghanlou, F. S., Nami, H., & Jafarzadeh, H. (2023). Modeling and optimization of hydraulic and thermal performance of a tesla valve using a numerical method and artificial neural network. *Entropy*, *25*(7), 967. https://doi.org/10.3390/e25070967

van Herpen, R. (2005, August). Meerzone luchtstroommodellen.

Volkshuisvesting en Ruimtelijke Ordening. (2022). Beleidsprogramma versnelling verduurzaming gebouwde omgeving [Geraadpleegd op 28 januari 2024].

Weger, D., Gehlen, C., Korte, W., Meyer-Brötz, F., Scheydt, J. C., & Stengel, T. (2021). Building rethought 3d concrete printing in building practice. *Construction Robotics*, *5*(3–4), 203–210. https://doi.org/10.1007/s41693-022-00064-5

World Green Building Council. (2023). *Global policy principles for a sustainable built environment* (tech. rep.). World Green Building Council. https://worldgbc.org/wp-content/uploads/2023/04/WorldGBC-Global-Policy-Principles_FINAL.pdf

Wu, P., Wang, J., & Wang, X. (2016). A critical review of the use of 3-d printing in the construction industry. *Automation in Construction*, *68*, 21–31. https://doi.org/10.1016/j.autcon.2016.04.005

Yin, H., Qu, M., Zhang, H., & Lim, Y. (2018). 3d printing and buildings: A technology review and future outlook. *Technology Architecture + Design*, *2*(1), 94–111. https://doi.org/10.1080/24751448.2018.1420968

Zhang, Y., Tong, J., & Zhu, Z. (2023). Numerical calculation of forward and reverse flow in tesla valves with different longitudinal width-to-narrow ratios. *Scientific Reports*, *13*(1). https://doi.org/10.1038/s41598-023-39758-3

Zhu, J., Zhou, H., Wang, C., Lü, Z., Yuan, S., & Zhang, W. (2021). A review of topology optimization for additive manufacturing: Status and challenges. *Chinese Journal of Aeronautics*, *34*(1), 91–110. https://doi.org/10.1016/j.cja.2020.09.020

THANK YOU

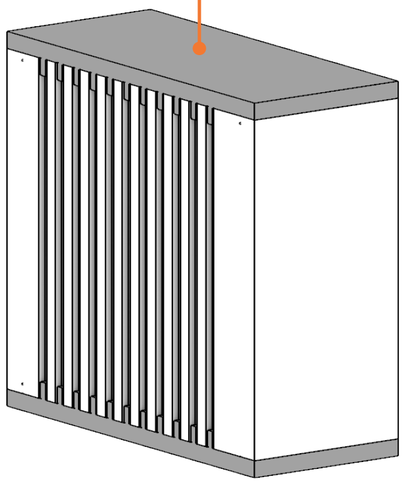

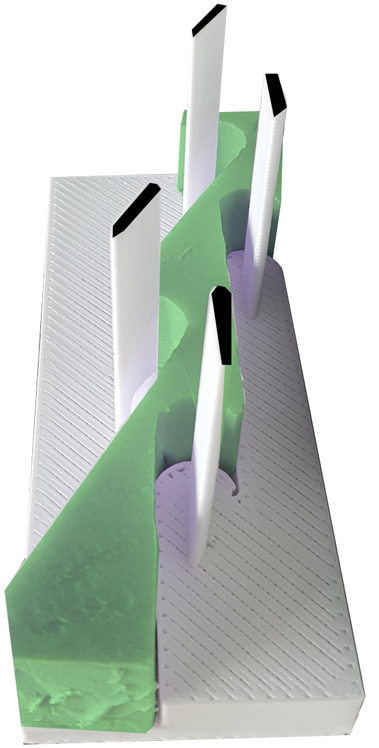

FUNCTIONAL PROTO TYPE

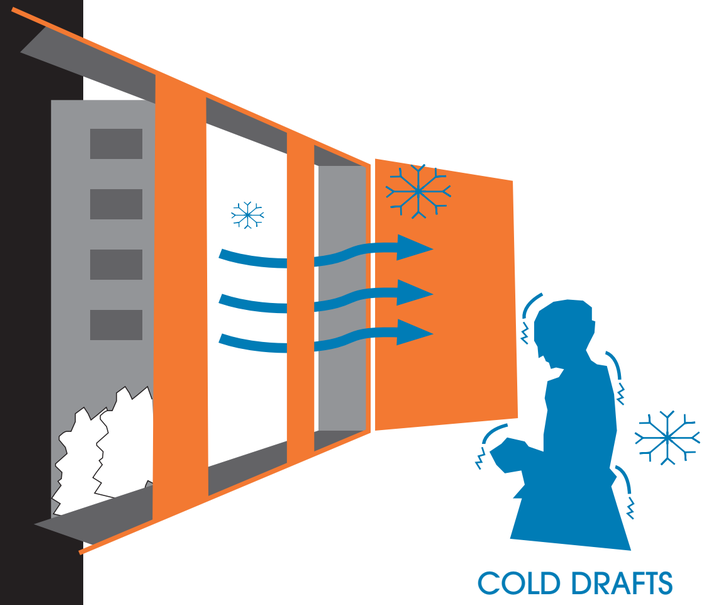

COLD DRAFTS

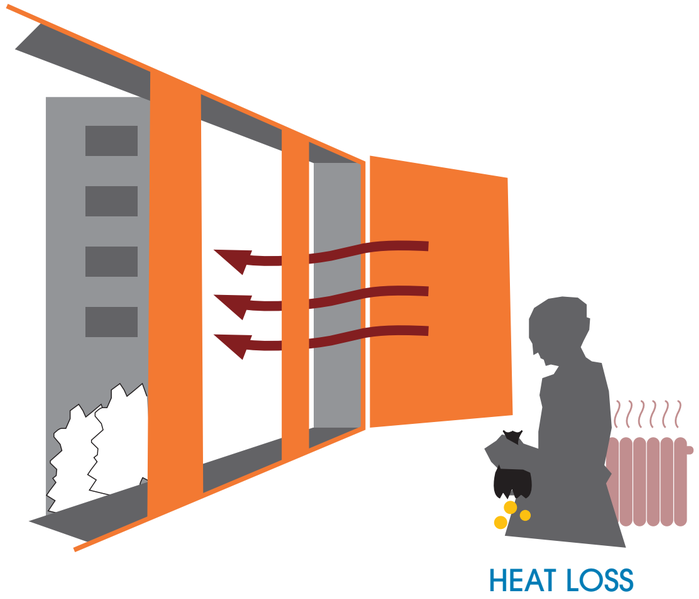

HEAT LOSS

FLUIDICS

REPRODUCE SELF REGULATING BEHAVIOUR

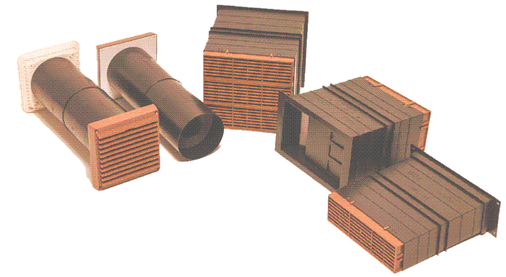

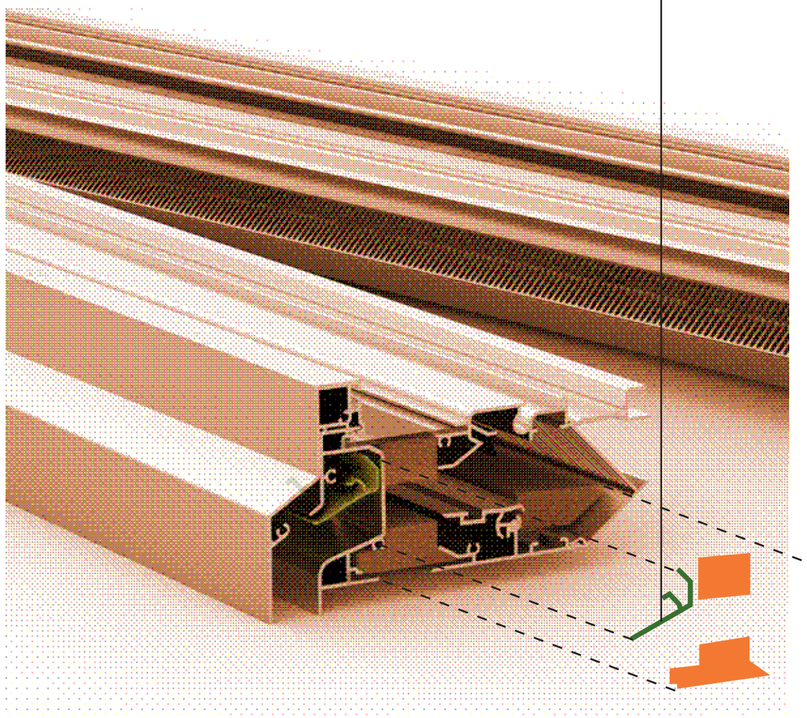

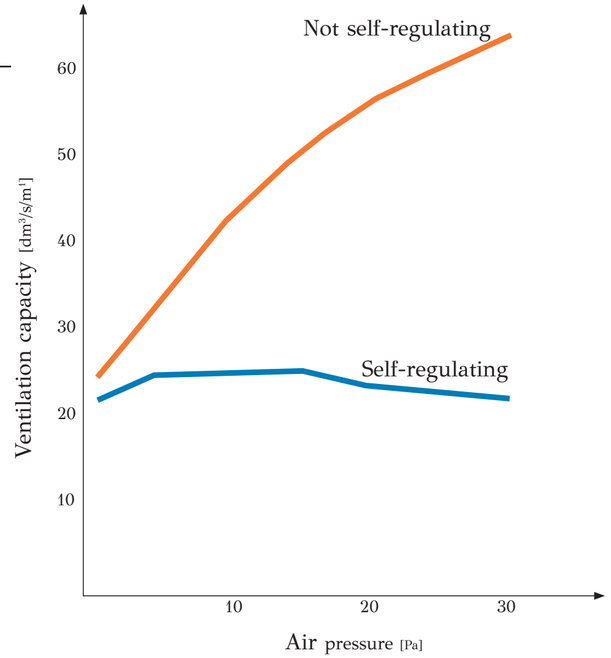

FLUIDICS

TESLA VALVE

FLUIDICS

FLUIDICS

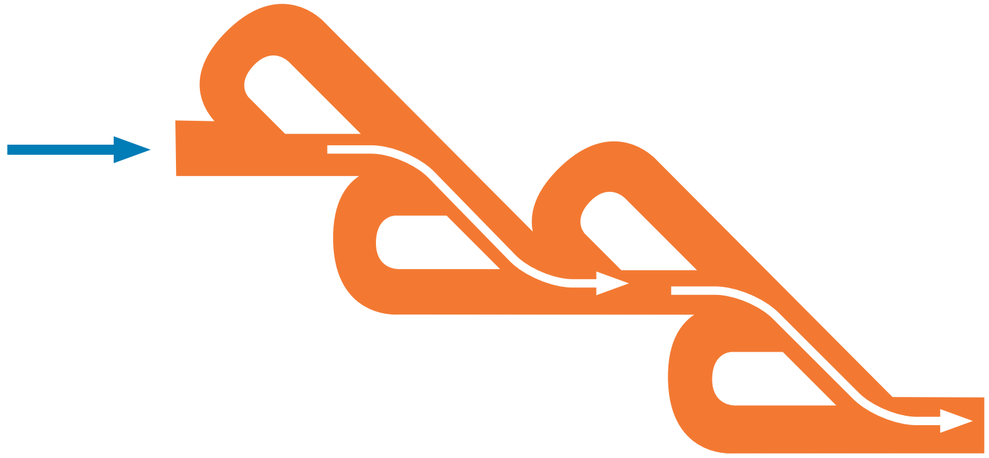

FORWARD FLOW

NO RESISTANCE

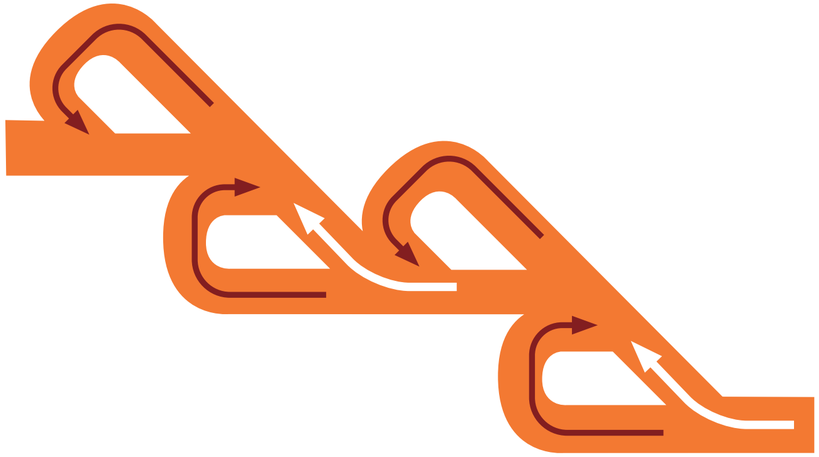

BACKWARD FLOW

HIGH RESISTANCE

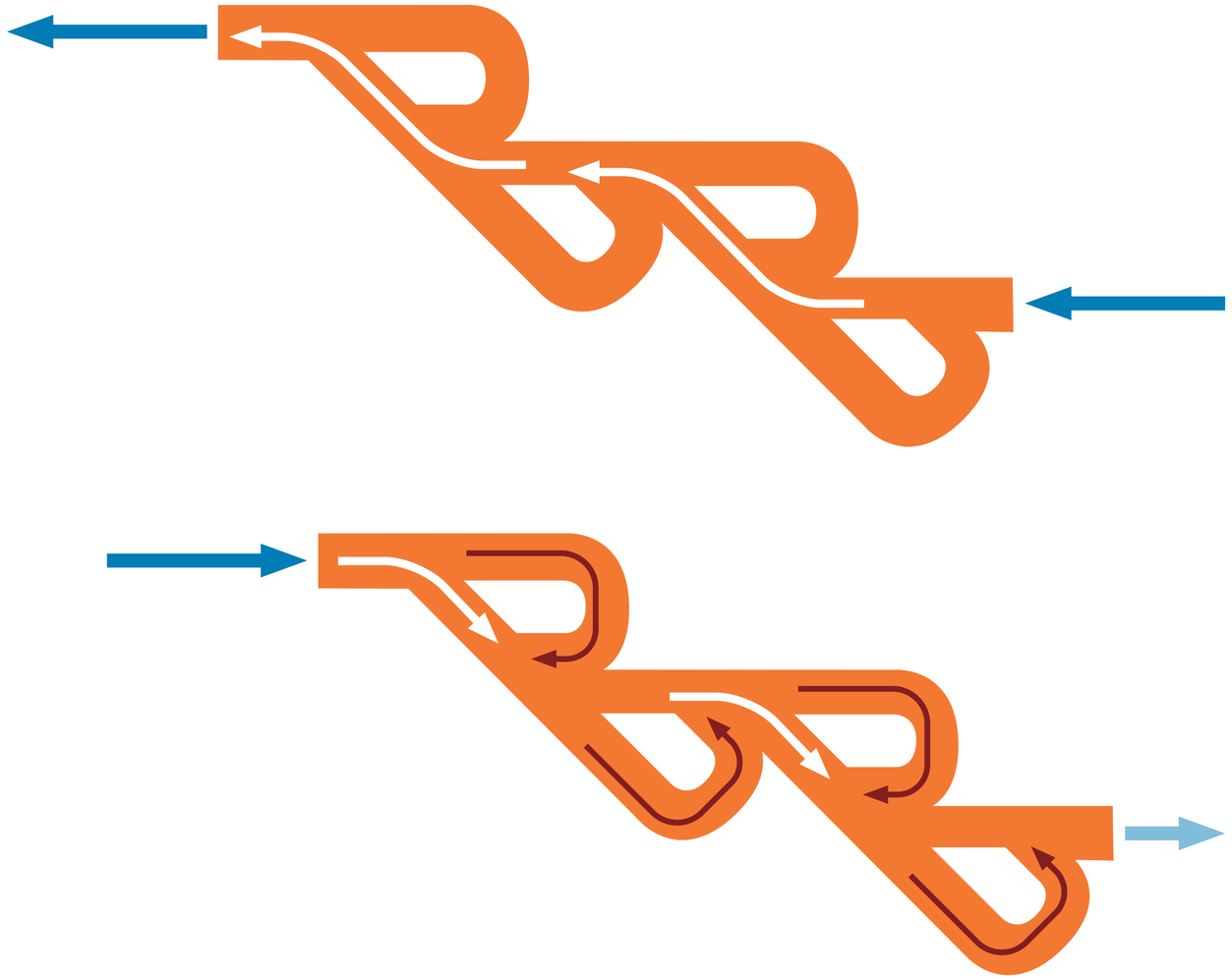

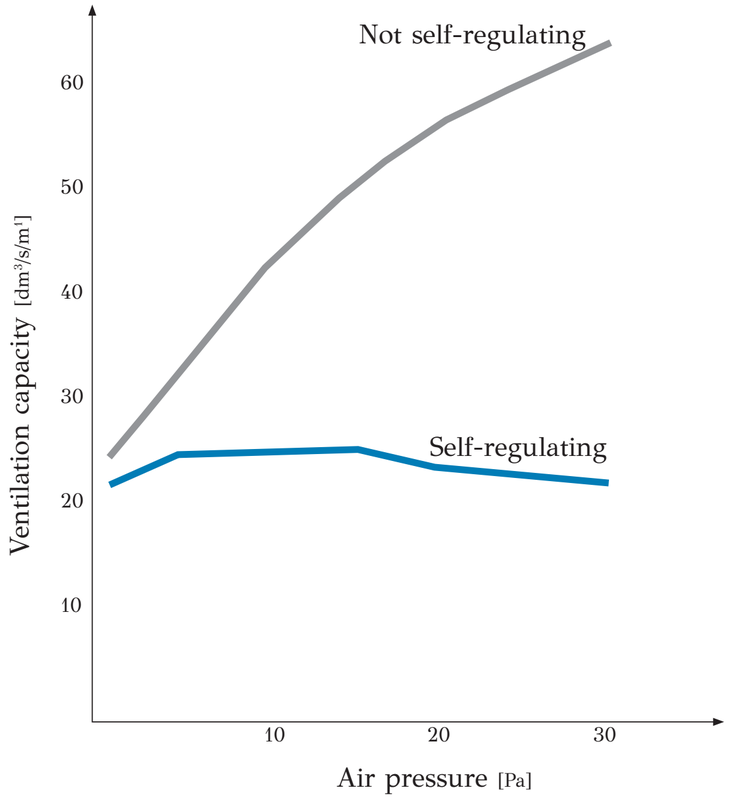

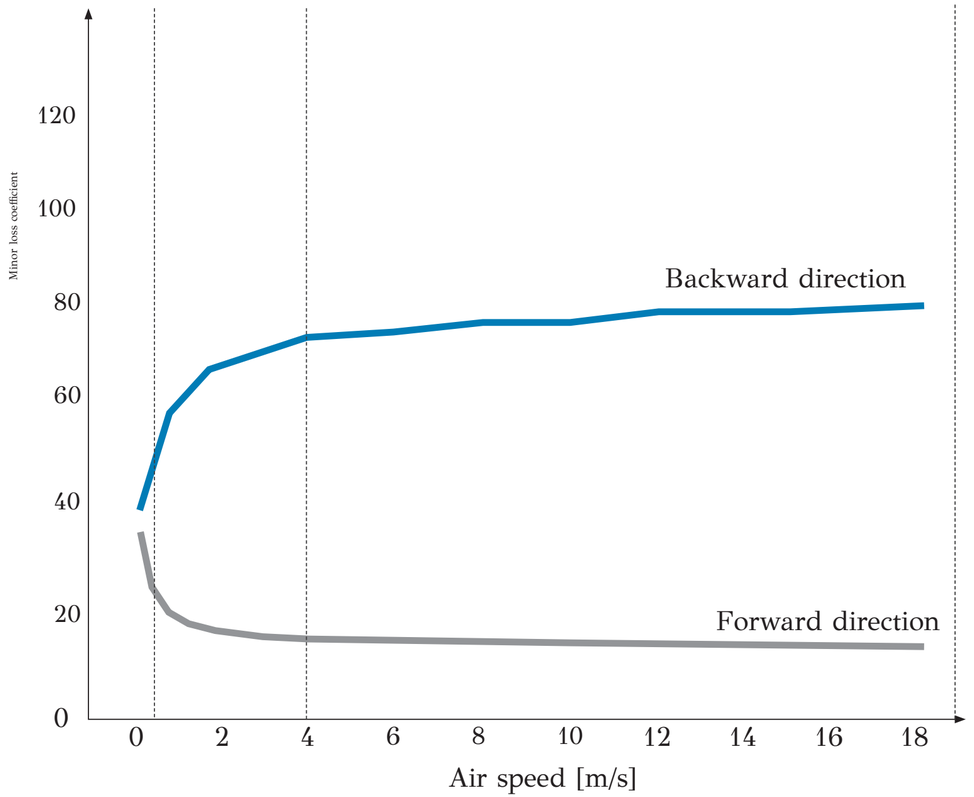

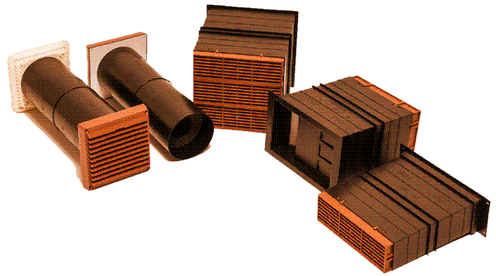

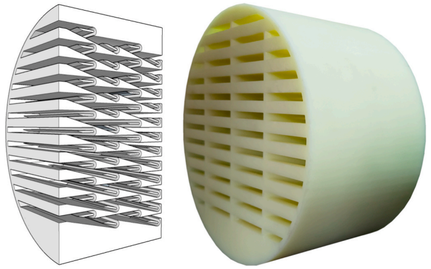

SOURCE: CAO ET AL. (2020)

FLUIDICS

ACOUSTICS

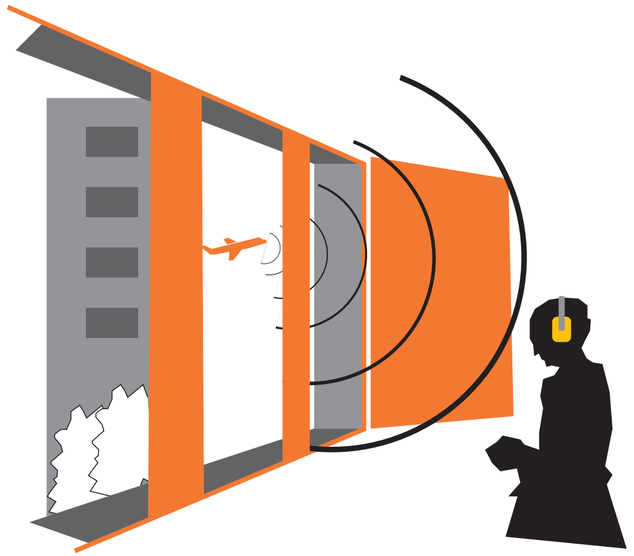

ACOUSTIC DISCOMFORT

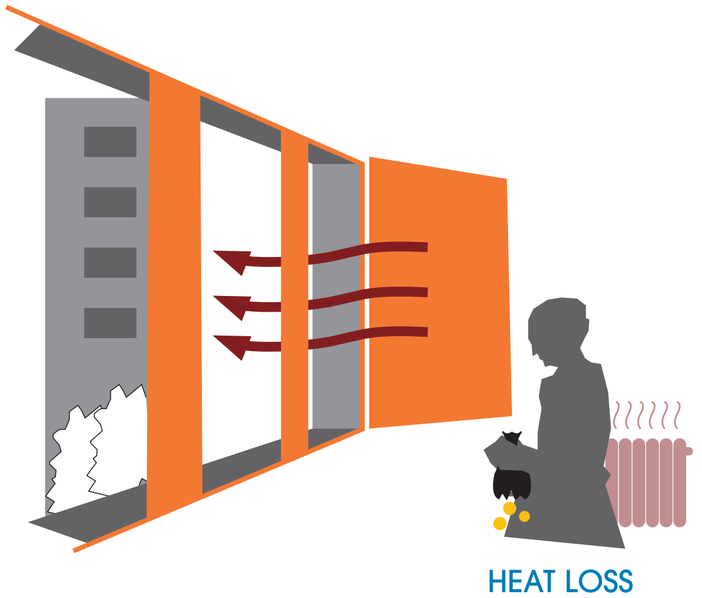

HEAT LOSS

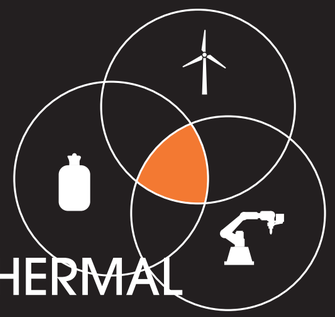

THERMAL

DYNAMIC INSULATION

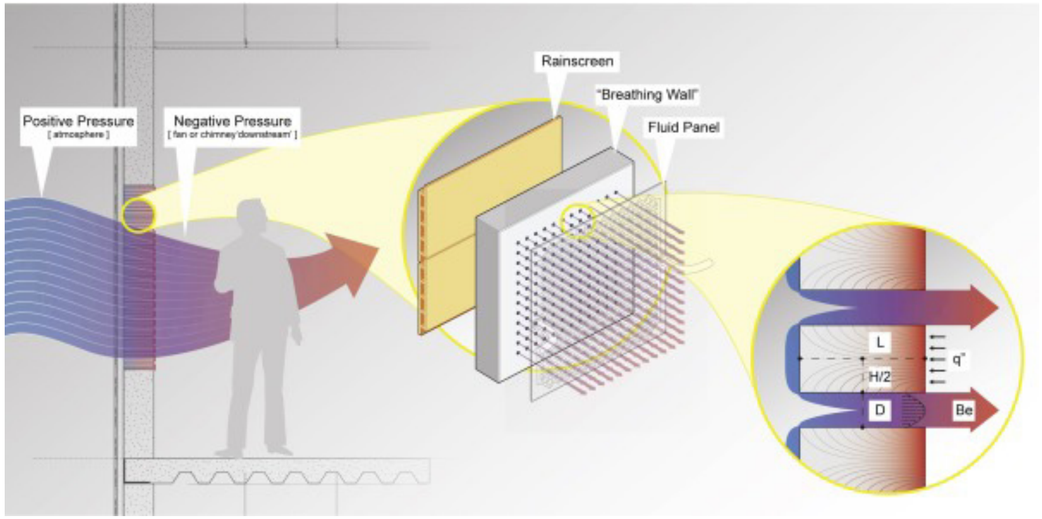

SOURCE: (Craig & Grinham, 2017)

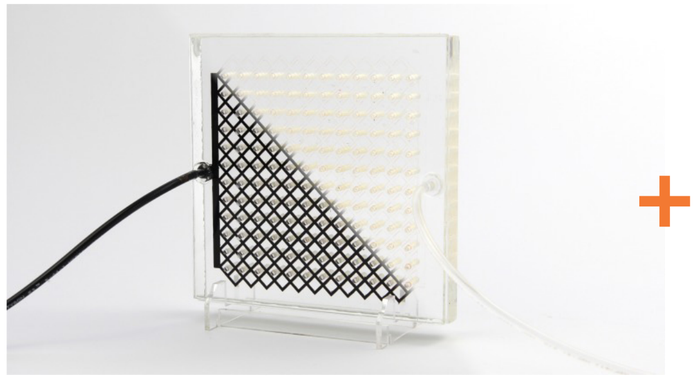

+

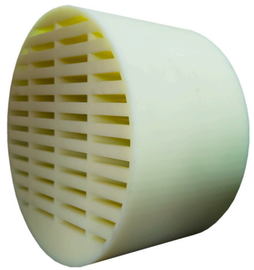

RESILIENT?

SOURCE: (Craig & Grinham, 2017)

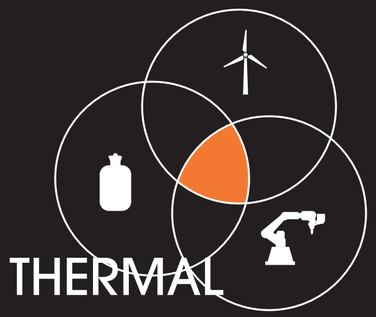

Kris De Decker

HEATING PEOPLE NOT SPACES

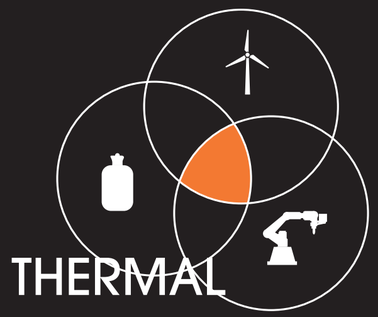

DESIGN

PROPOSAL

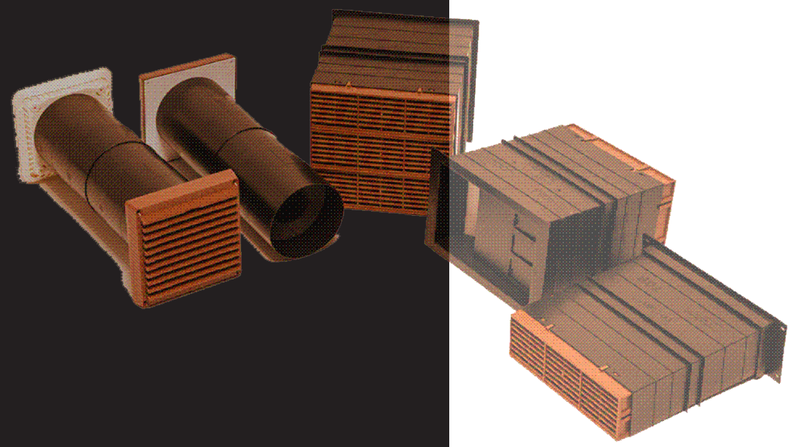

DESIGN PROPOSAL

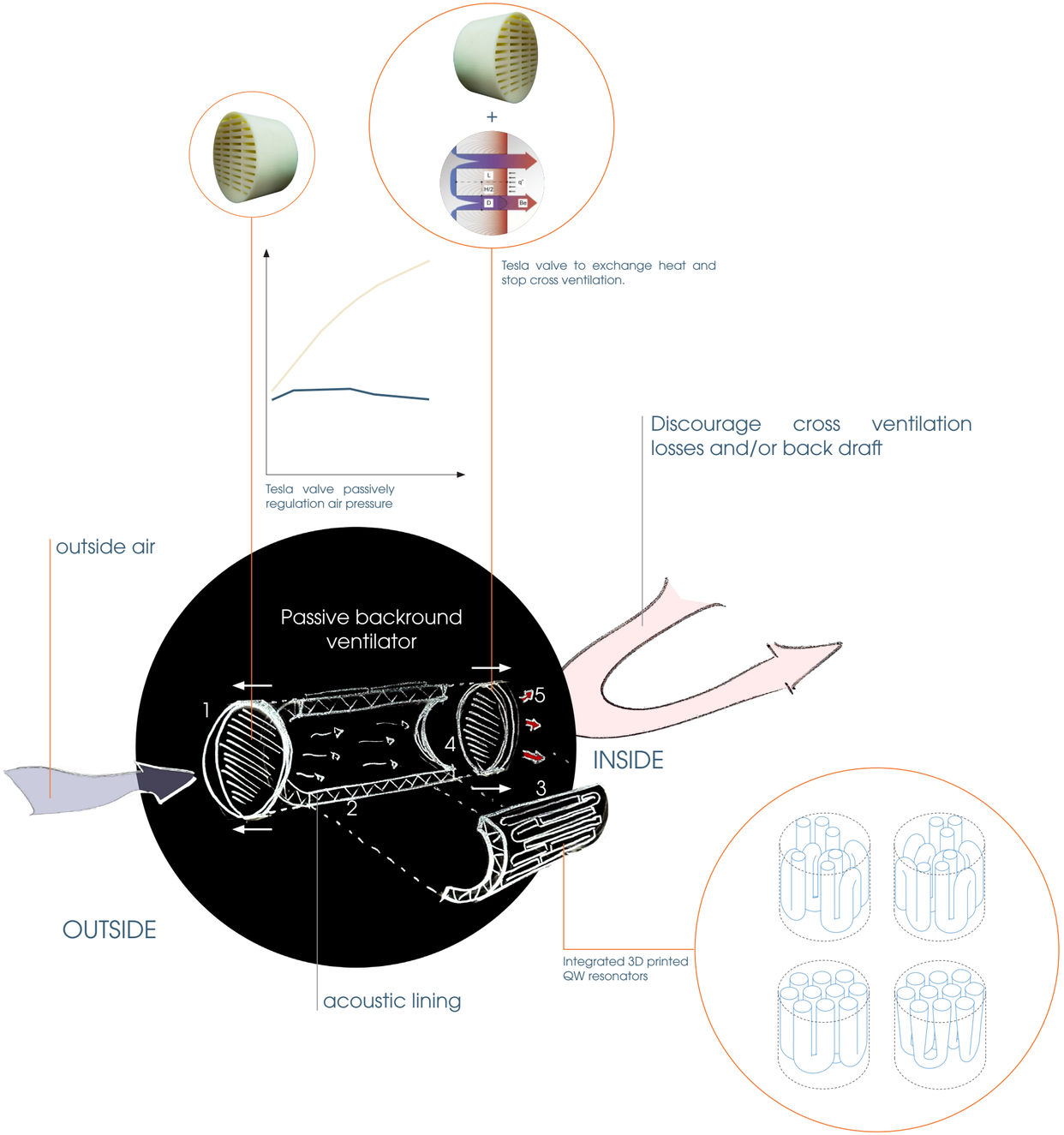

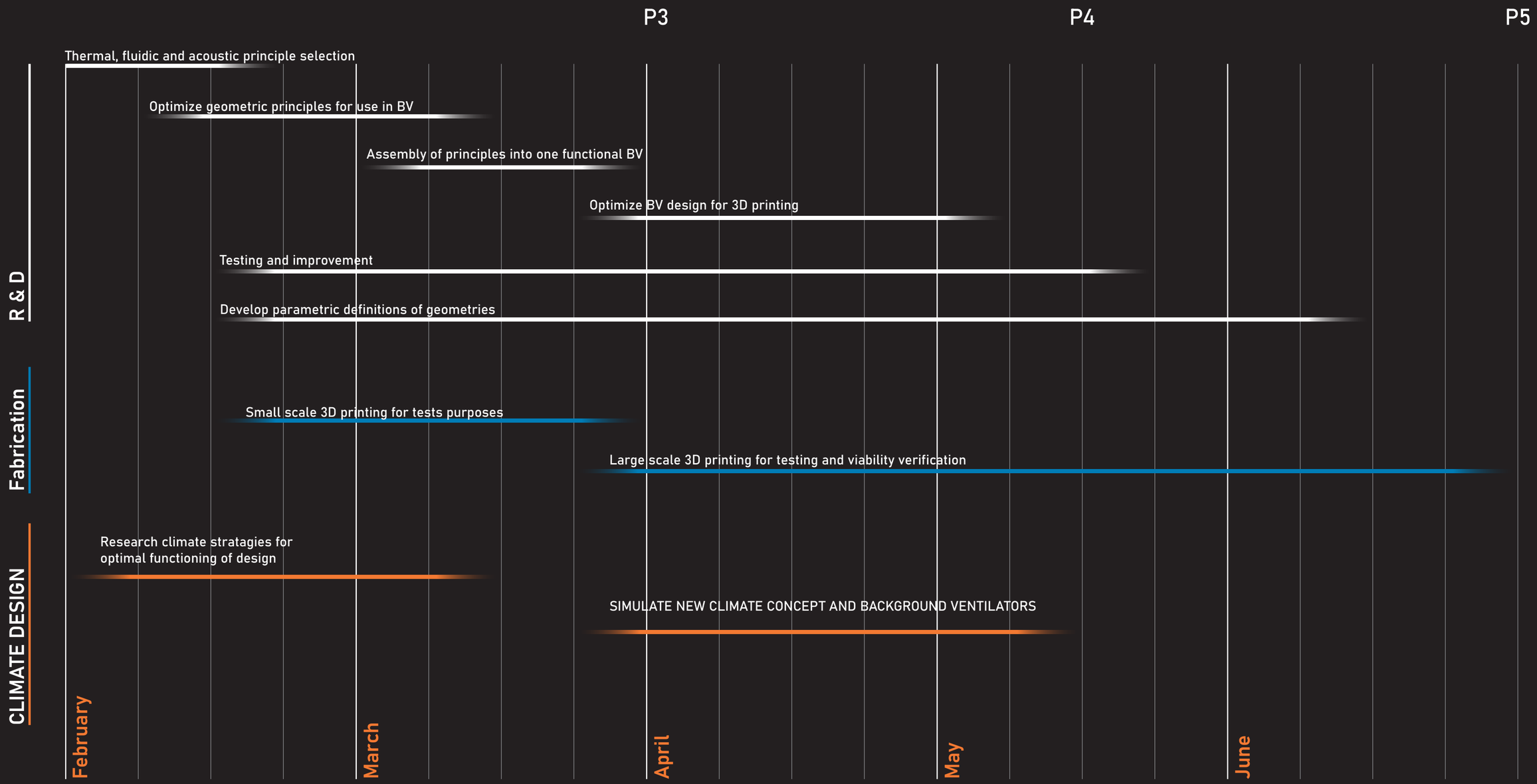
P3
P4
P5
Thermal, fluidic and acoustic principle selection
Optimize geometric principles for use in BV
Assembly of principles into one functional BV
Optimize BV design for 3D printing
Testing and improvement
Develop parametric definitions of geometries
R & D
Small scale 3D printing for tests purposes
Large scale 3D printing for testing and viability verification
Fabrication
Research climate stratagies for
optimal functioning of design
SIMULATE NEW CLIMATE CONCEPT AND BACKGROUND VENTILATORS
CLIMATE DESIGN
February
March
April
May
June

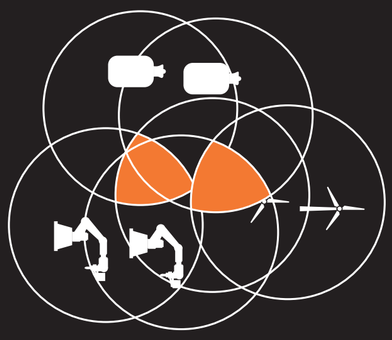

WINDOWS OPEN

GOOD IAQ

HIGH HEAT LOSS

POOR THERMAL COMFORT

POOR ACCOUSTIC COMFORT

WINDOWS CLOSED

POOR IAQ

LOW HEAT LOSS

GOOD THERMAL COMFORT

GOOD ACCOUSTIC COMFORT

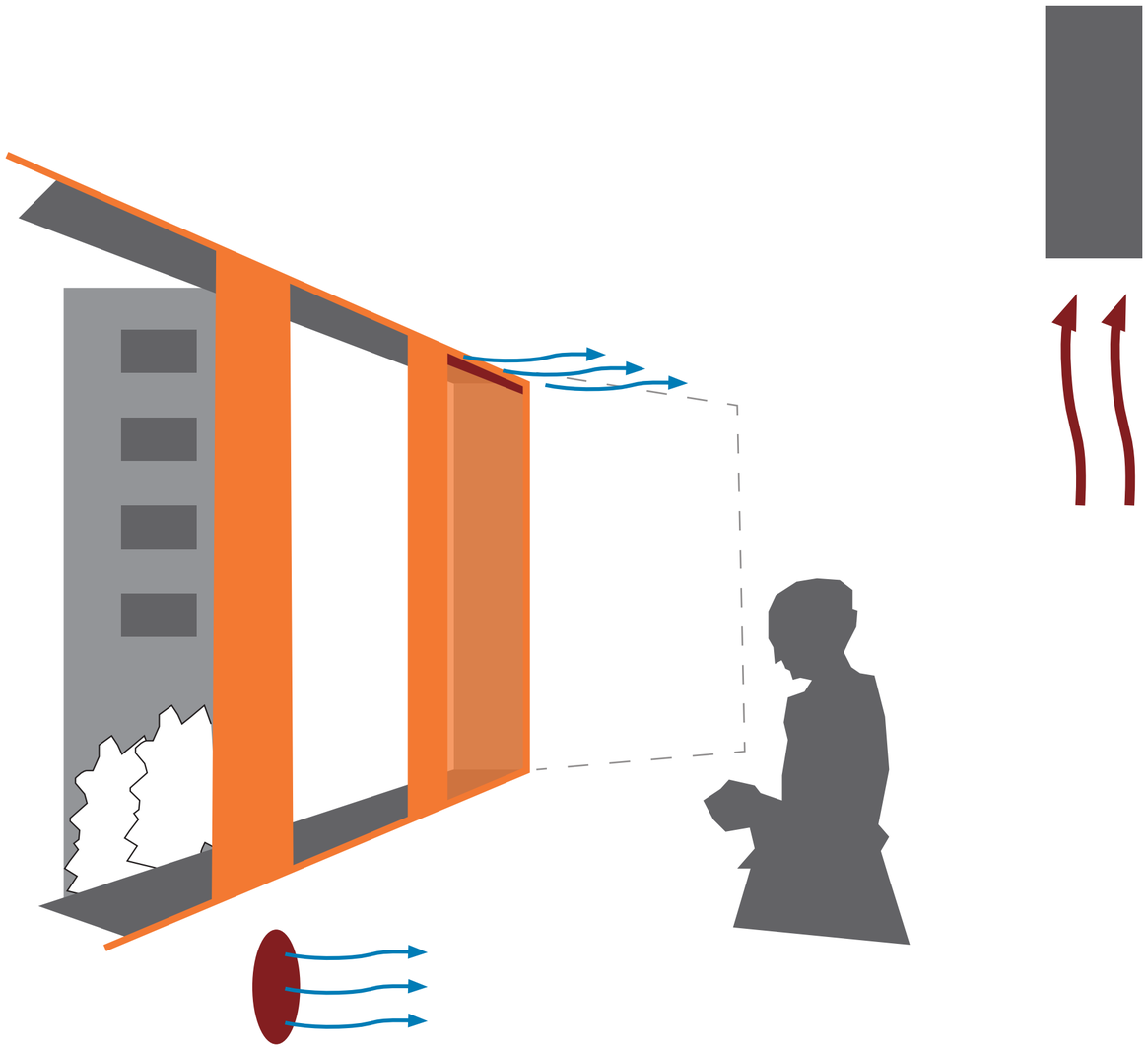

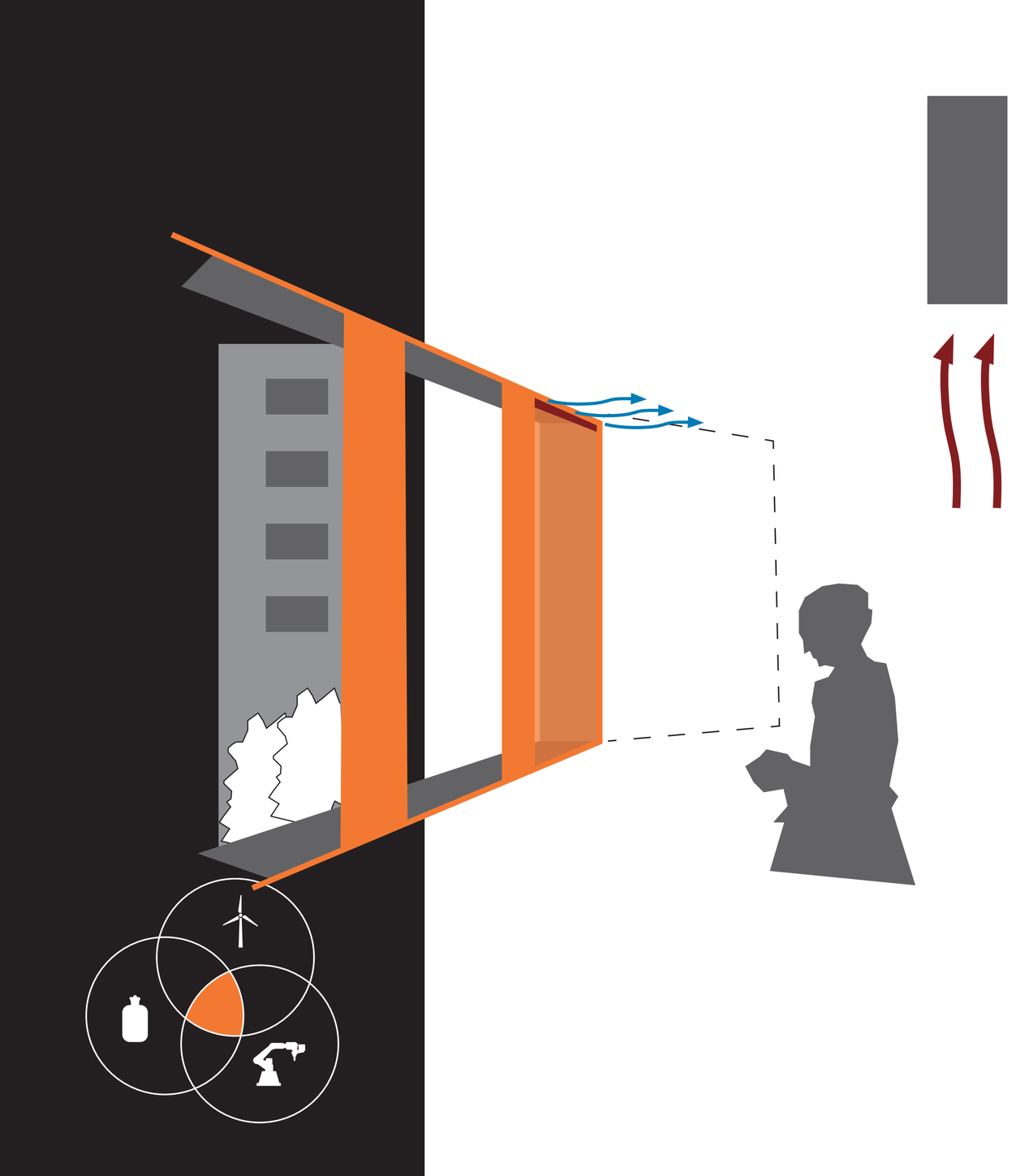

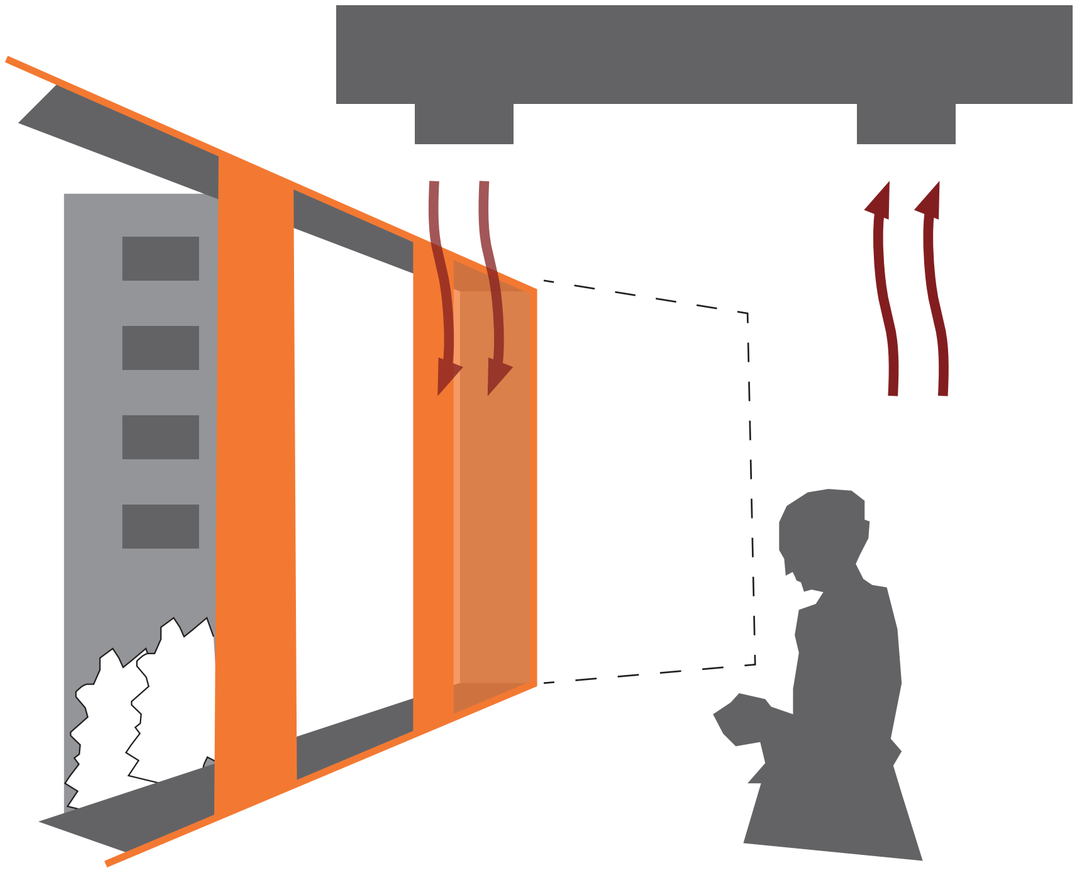

COMPLEX
MAINTAINANCE HEAVY

A RIGHT ANSWER TO A WRONG QUESTION?

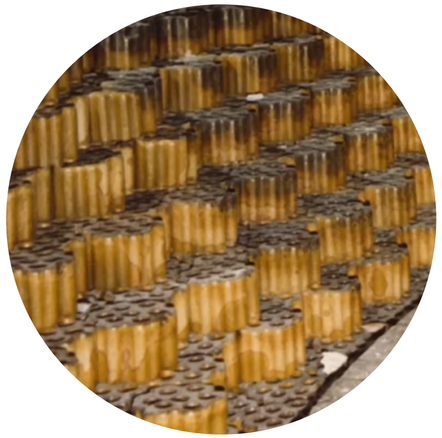

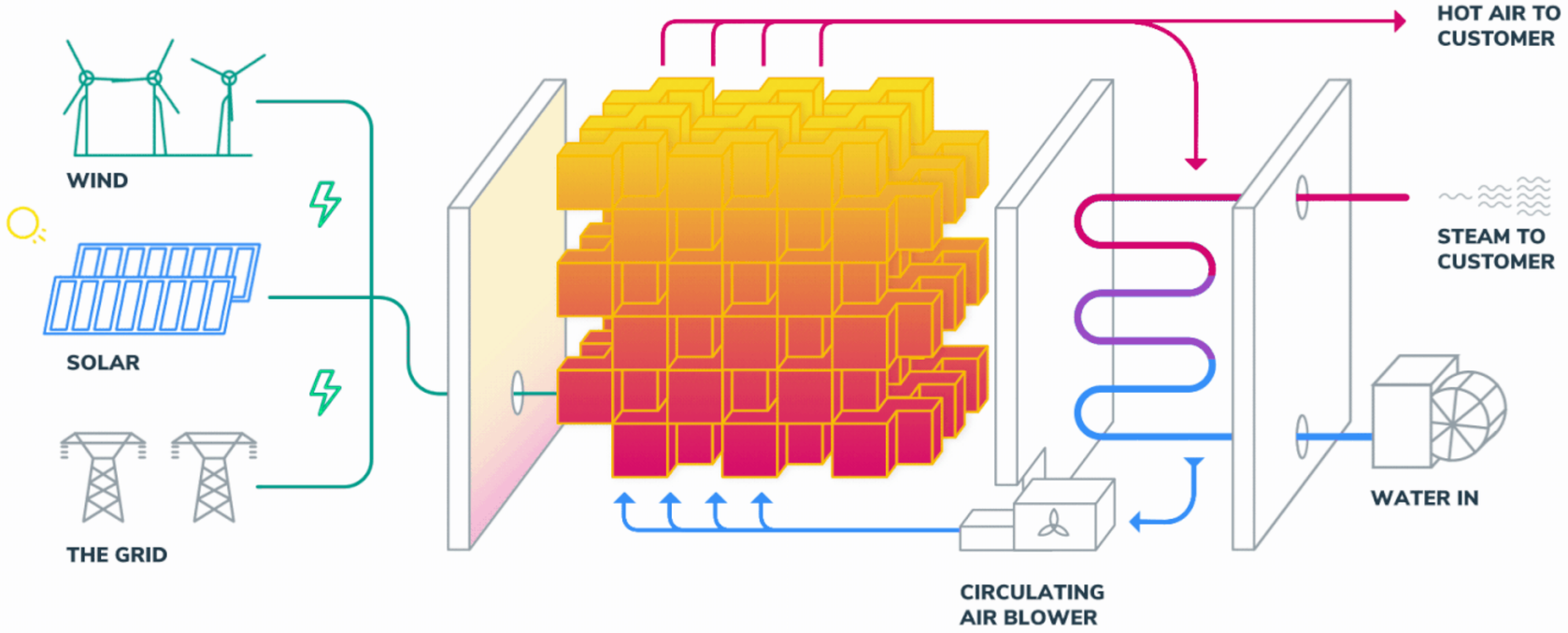

Source: rondo.com

“NEW AND BORING ARE EXCELLENT FOR GOING FAST”

Source: https://www.ted.com/speakers/john_o_donnell

OBJECTIVE

CAN WE, BY USING 3D PRINTINGS STRENGTHS AND ADOPTING A HOLISTIC DESIGN APPROACH, GET SIMILAR ENERGY AND COMFORT PERFORMANCE FROM TYPE C AS FROM TYPE D BUT WITH PASSIVE AND RESILIANTS SOLUTIONS?

EXCERSISE IN HOLISTIC DESIGN

AND CREATE ARCHITECTURAL CONCEPTS IN WHICH 3D-PRINTING CAN FLOURISH

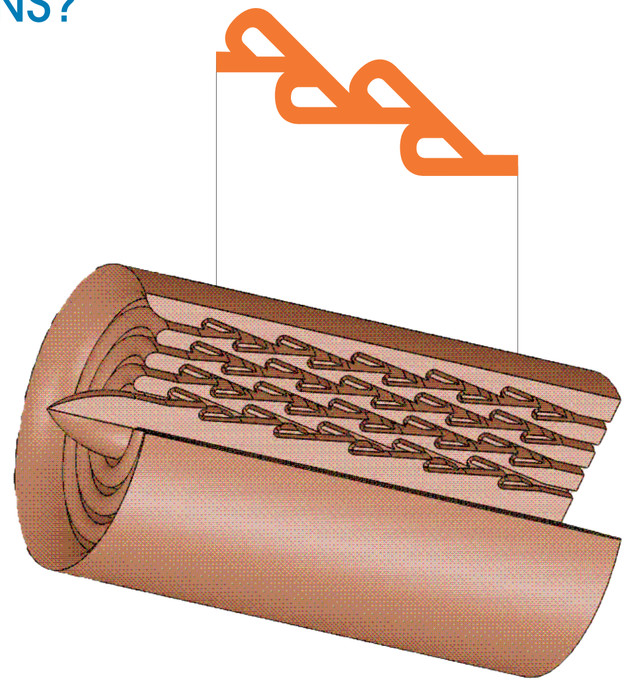

1) IDENTIFY MULTI-FACETED ISSUES

2) IDENTIFY EXISTING SOLUTIONS

3) OPTIMIZE FOR 3D PRINTING

4) INTEGRATE INTO HOLISTIC DESIGN

WHAT DOES THIS MEAN FOR THE BUILT ENVIRONMENT?

NZE BUILDINGS AND RENOV

GREEN ENERGY CAN POWER
A GREAT CIVILIZATION...

...JUST NOT OUR CURRENT ONE

NATE HAGANS

FOSSIL ENERGY

2024

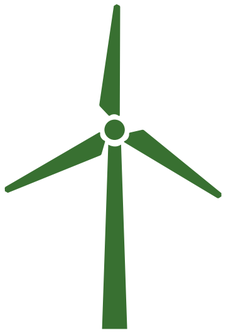

GREEN ENERGY

2050

CURRENT APPLICATION

SCALABILITY

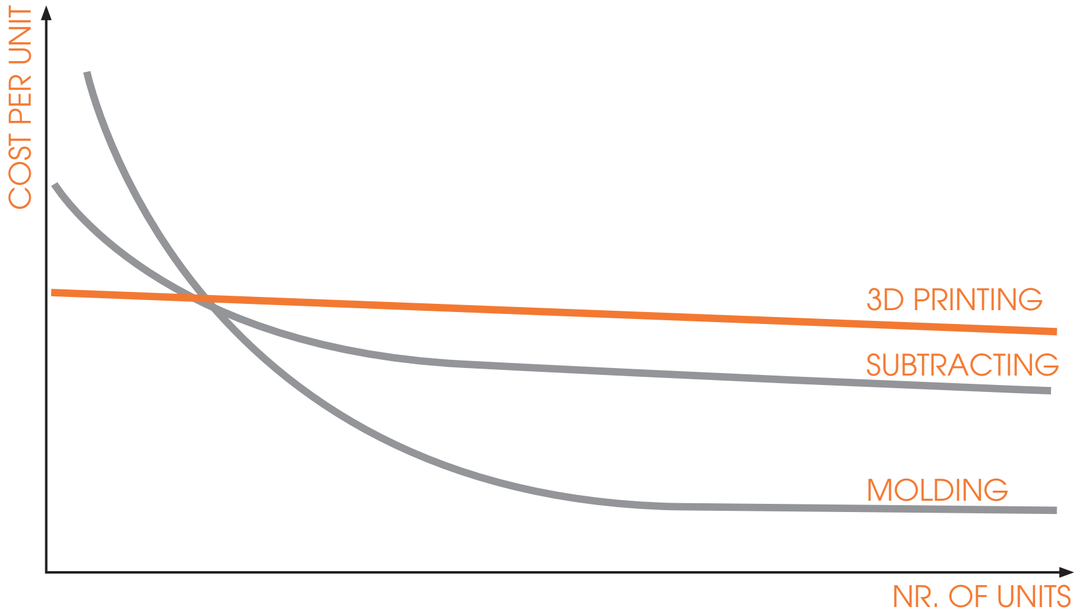

DEPLOYMENT

IN THE BUILT ENVIRONMENT DEVELOPMENT FOCUSES MAINLY ON OBTAINING FINANCIAL AND TIME GAIN FOR TRADITIONAL CONSTRUCTION METHODS

PROBLEM STATEMENT

“Despite decades of development, the adoption of large-scale 3D printing (3DP) in construction remains limited, with a focus on economic gains over innovative design and construction methods, hindering efficiency and radical innovation, while ongoing debate surrounds its cost-effectiveness for traditional building designs, highlighting the need to bridge the gap between theoretical advancements and practical industry needs for innovation and growth within the 3D printing sector.”

RESEARCH QUESTION

“How can a shift towards a more holistic design approach facilitate the widespread adoption of additive manufacturing in the built environment, addressing immediate industry needs and fostering innovation and growth?”

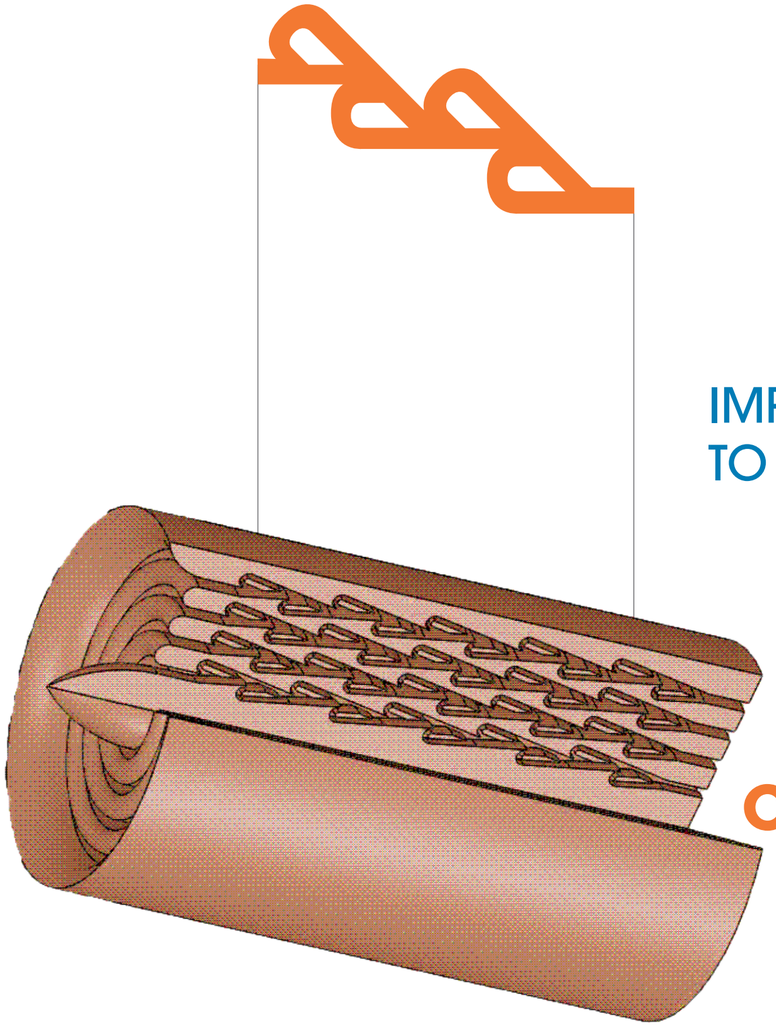

IMPORTANT TO EXPLOIT ITS STRENGTHS
TO OVERCOME ITS WEAKNESSES:

COMPLEXITY FOR FREE
FOR PASSIVE SOLUTIONS

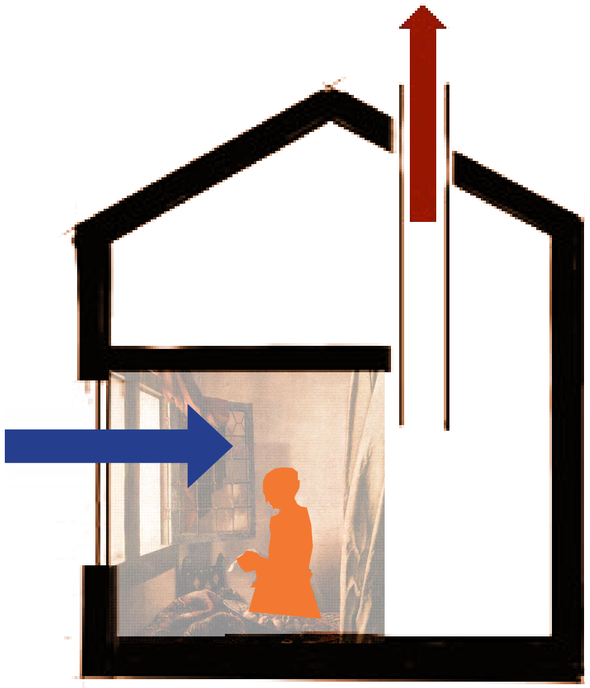

A

65 - 100% OF EXISTING BUILDING STOCK RELIES ON NATURAL VENTILATION

75% OF BUILDING STOCK IN EU TO BE RENOVATED BY 2050 INTO NZEB

OFFER A MORE RELIABLE WAY OF VENTILATION

1) IDENTIFY MULTI-FACETED ISSUES
2) IDENTIFY EXISTING SOLUTIONS
3) OPTIMIZE FOR 3D PRINTING
4) INTEGRATE INTO HOLISTIC DESIGN

1) IDENTIFY MULTI-FACETED ISSUES
2) IDENTIFY EXISTING SOLUTIONS
3) OPTIMIZE FOR 3D PRINTING
4) INTEGRATE INTO HOLISTIC DESIGN

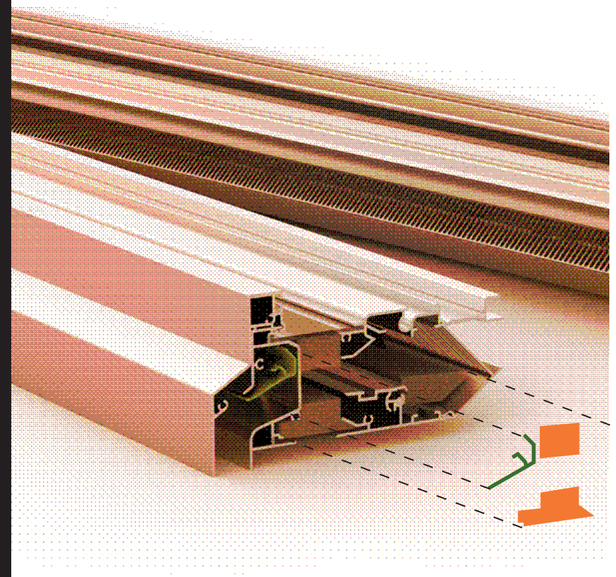

SOURCE: DUCO

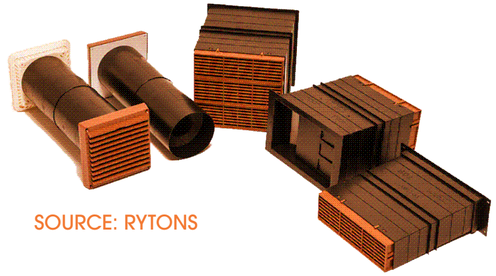

SOURCE: RYTONS

SOURCE: DUCO

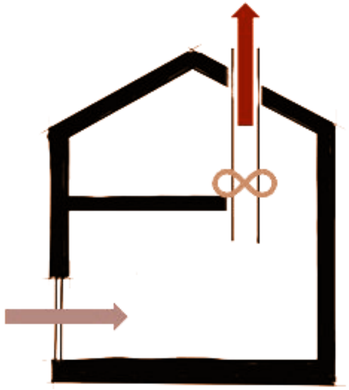

C

RELIES ON BACKGROUND VENTILATORS THAT:

REGULATE INFLOW MECHANICALLY OR AUTOMATICALLY

ABSORB SOUND THROUGH ACOUSTIC LINING

CAN BE IMPLEMENTED INTO WINDOWS AND WALLS

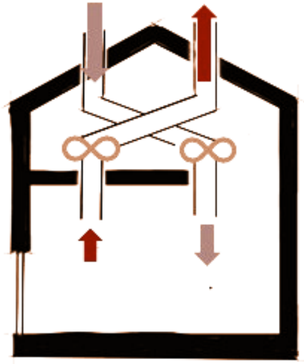

D

FULLY MECHANIZED SYSTEM, SO:

IT CAN RECAPTURE HEAT

NO DIRECT HOLES IN FACADE

THUS NO ACOUSTIC COMPLAINTS

AIR PRE-WARMED

1) IDENTIFY MULTI-FACETED ISSUES
2) IDENTIFY EXISTING SOLUTIONS
3) OPTIMIZE FOR 3D PRINTING
4) INTEGRATE INTO HOLISTIC DESIGN

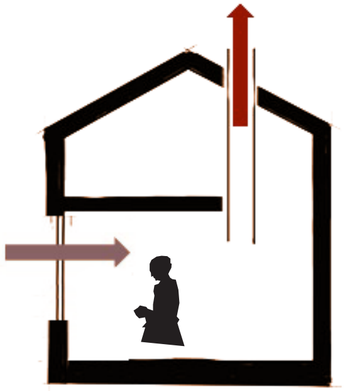

A

RESILIENT
INEFFICIENT
LOW COMFORT

B

BARELY USED IN
PRACTICE

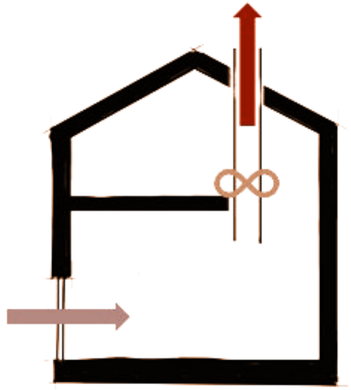

C

RESILIENT
DECENT EFFICIENCY
DECENT COMFORT

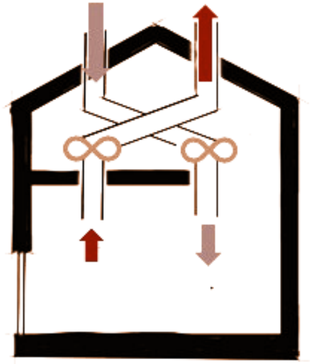

D

COMPLEX
EFFICIENT
HIGH COMFORT

1) IDENTIFY MULTI-FACETED ISSUES

2) IDENTIFY EXISTING SOLUTIONS

3) OPTIMIZE FOR 3D PRINTING

4) INTEGRATE INTO HOLISTIC DESIGN

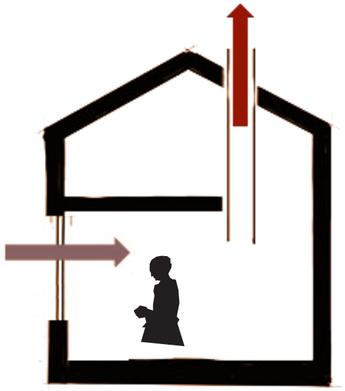

A

MOST COMMON

B

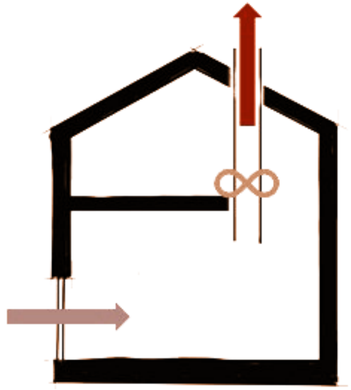

C

MOST SUITED FOR
RENOVATION

2.5 MLN DWELLINGS TO BE RENOVATED IN THE NETHERLANDS

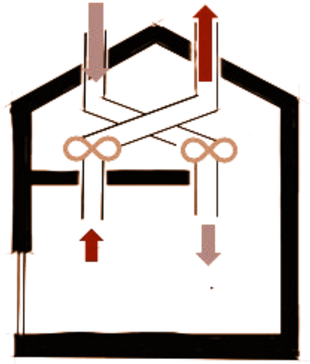

D

MOST SUITED FOR
NEW CONSTRUCTION

900.000 NEW DWELLINGS IN THE NETHERLANDS

QUARTER WAVE LENGTH RESONATORS

SOURCE: STUDIO PHI

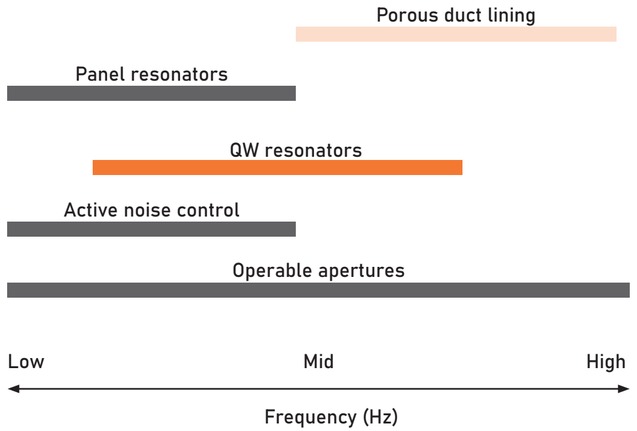

1) IDENTIFY MULTI-FACETED ISSUES
2) IDENTIFY EXISTING SOLUTIONS
3) OPTIMIZE FOR 3D PRINTING
4) INTEGRATE INTO HOLISTIC DESIGN

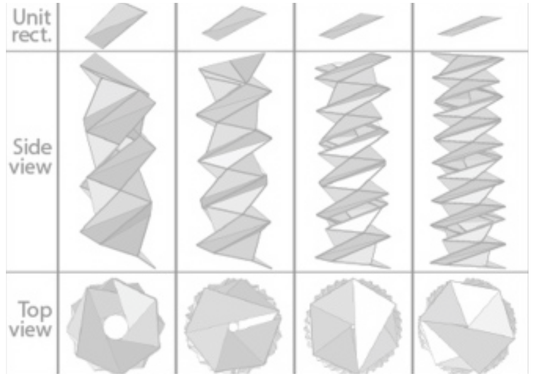

SOURCE: CAMBONIE ET AL (2018)

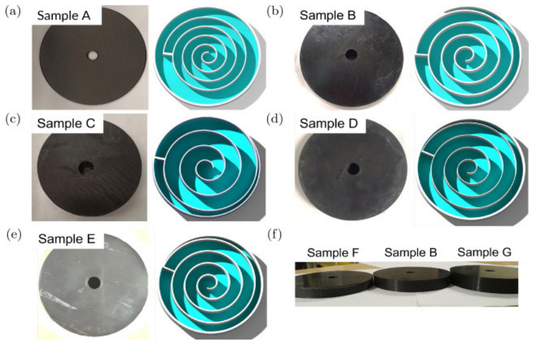

SOURCE: CATAPANE ET AL. (2023)

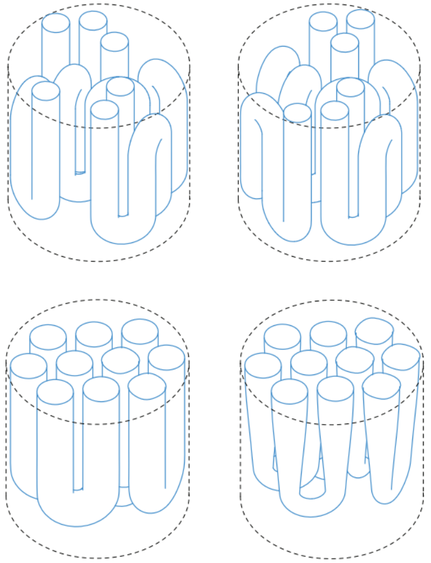

SOURCE: SETAKI (2012)

1) IDENTIFY MULTI-FACETED ISSUES
2) IDENTIFY EXISTING SOLUTIONS
3) OPTIMIZE FOR 3D PRINTING
4) INTEGRATE INTO HOLISTIC DESIGN

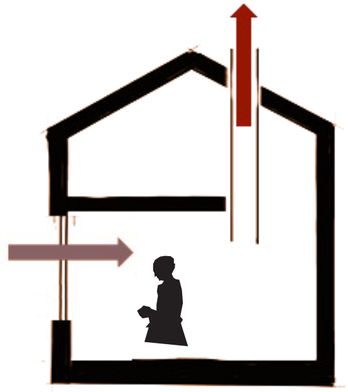

A

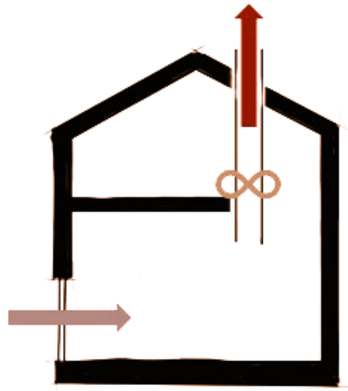

C

	A	C
P	1 Pa	5 Pa
V	0.2 m/s	0.2 m/s

1) IDENTIFY MULTI-FACETED ISSUES
2) IDENTIFY EXISTING SOLUTIONS
3) OPTIMIZE FOR 3D PRINTING
4) INTEGRATE INTO HOLISTIC DESIGN

FUNCTIONAL

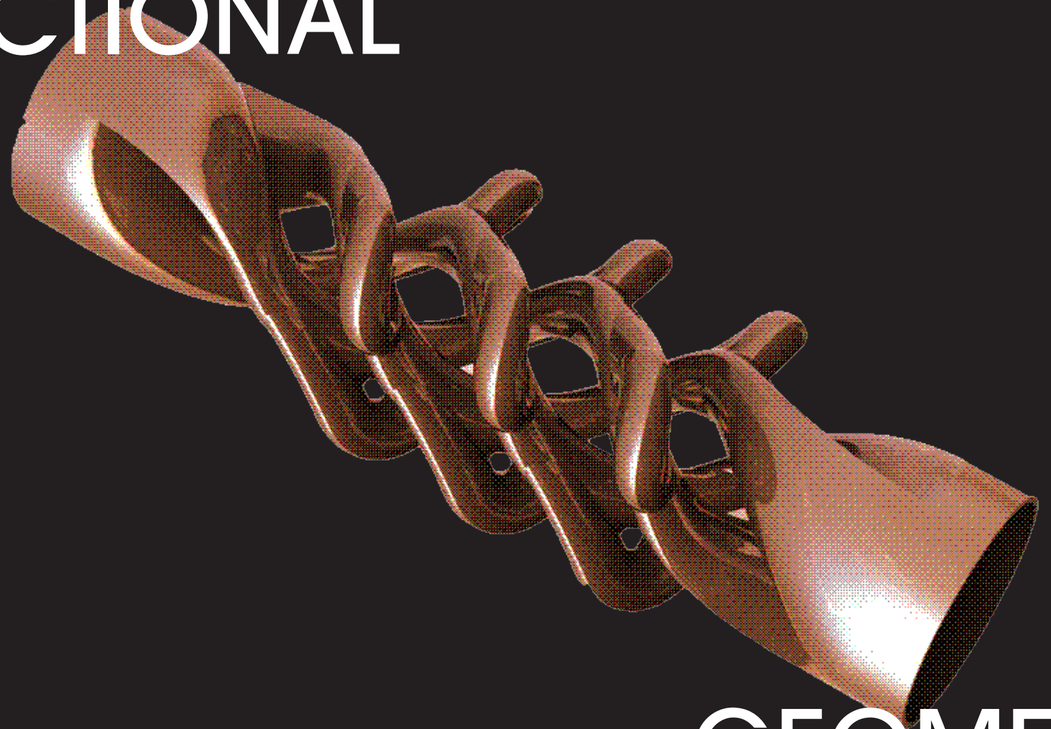

GEOMETRIES

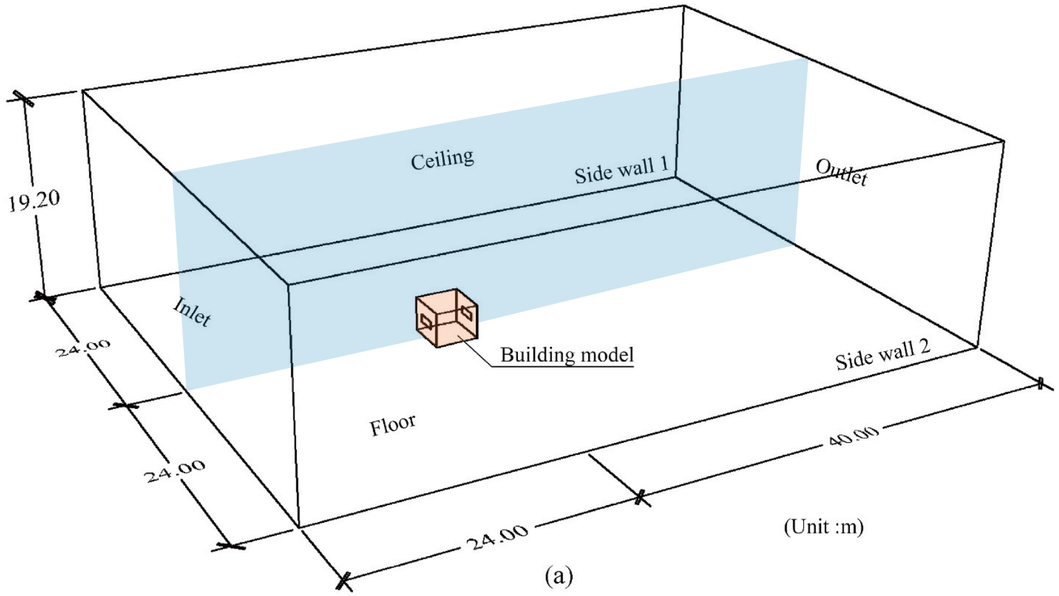

(a)

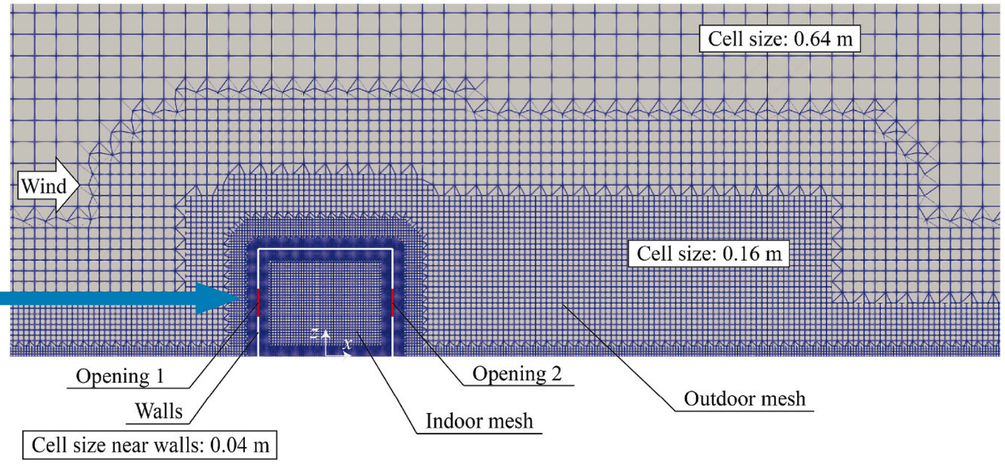

(b)

$$\Delta P_w = \frac{1}{2} \cdot \rho \cdot C_p \cdot v^2$$

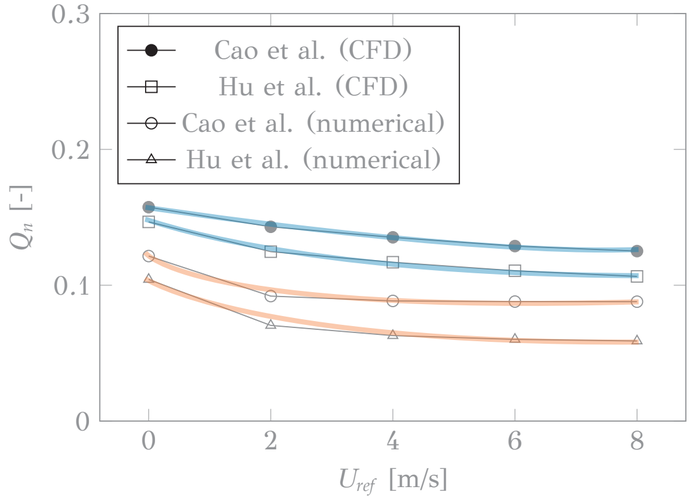

$C_p = 0.6$

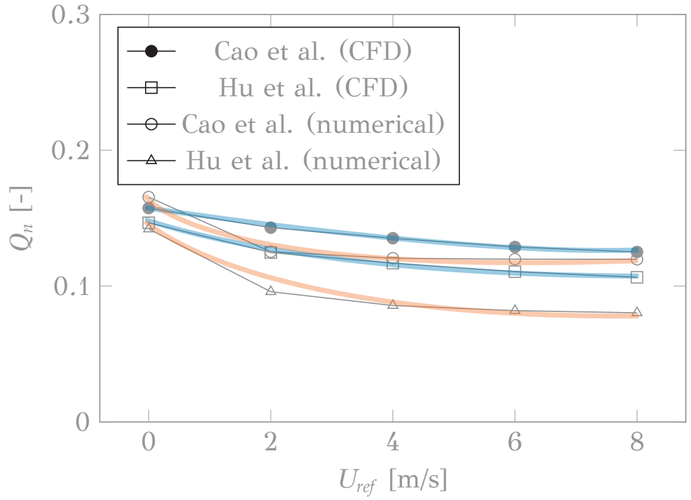

$C_p = 1.2$

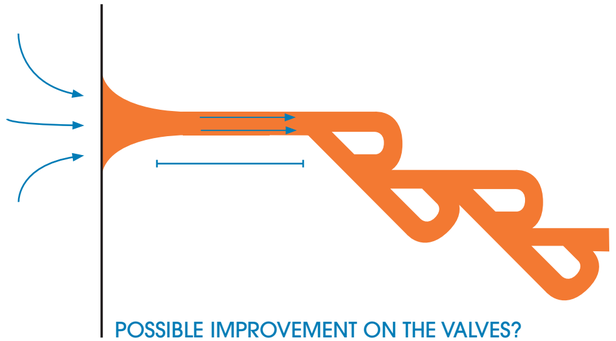

POSSIBLE IMPROVEMENT ON THE VALVES?

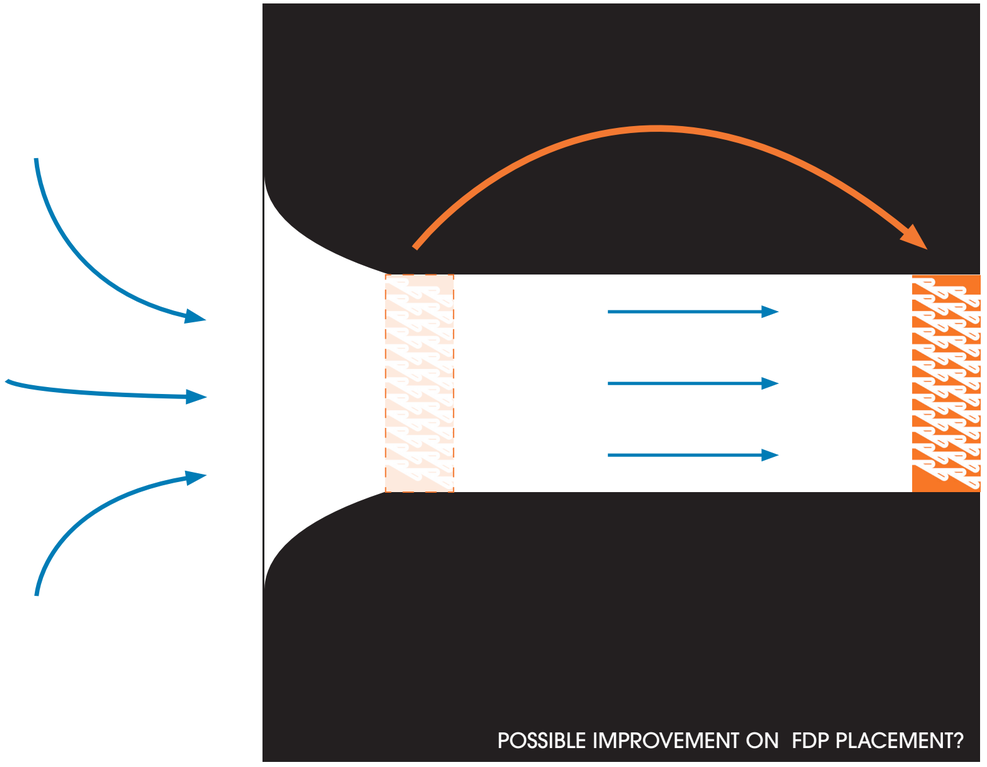

POSSIBLE IMPROVEMENT ON FDP PLACEMENT?

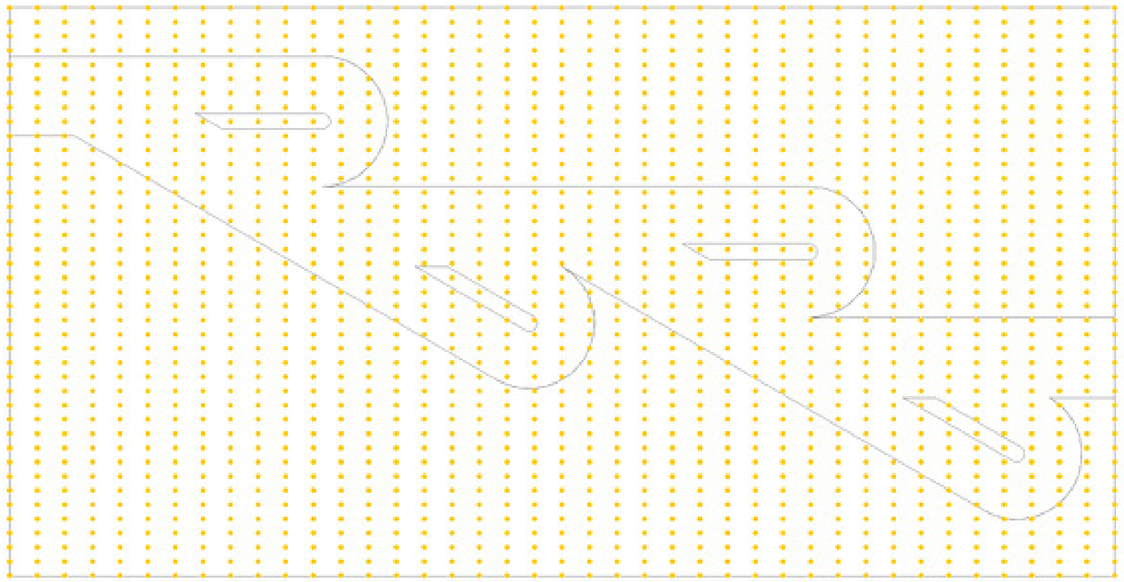

GRID

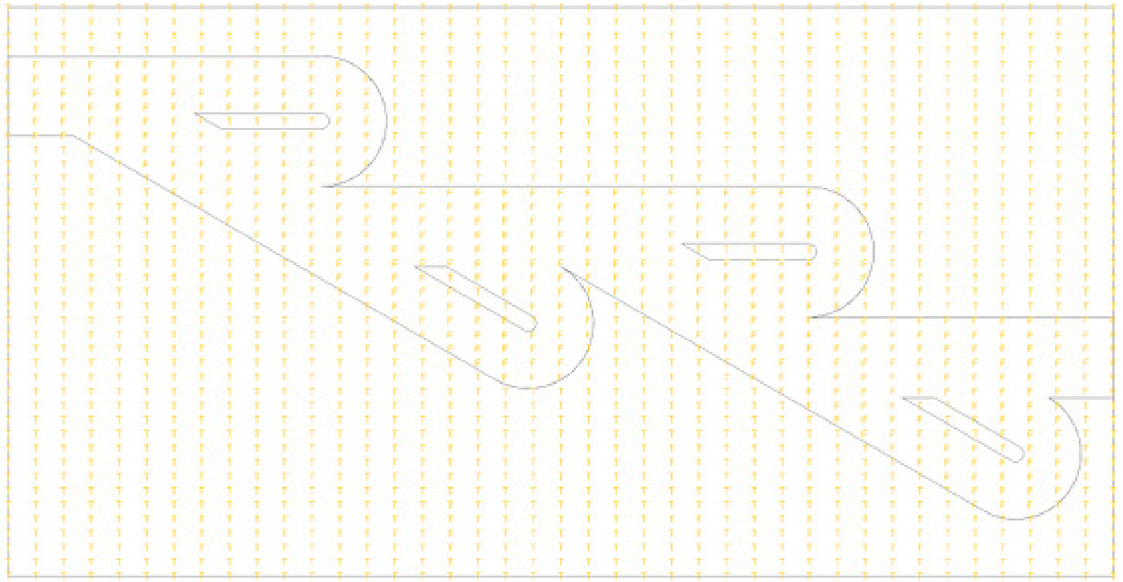

BINARY MASK

DU et al. (2023)

42]. Babaoglu et al. [43] employed both computational fluid dynamics (CFD) and ANN models to investigate and optimize multi-stage Tesla valves. Their research revealed that diminishing the valve-to-valve distance in relation to the hydraulic diameter led to the highest diodicity and the least deviation in flow performance. They achieved a maximum diodicity value of 1.811, while the lowest values for flow performance deviation and maximum relative pressure drop were found to be 194.72 Pa and 352.69 Pa, respectively.

Despite previous studies proposing different modifications to enhance the performance of Tesla valves, achieving optimal fluid control in both directions has remained a persistent challenge. In order to tackle this issue, this study introduces a novel structure for a Tesla valve. In addition to presenting a Tesla valve with a new design, arc-shaped fins are used in the bent part of the channels; so that alongside providing a more suitable thermal performance, a greater pressure drop can be obtained in the reverse direction than in the forward direction. The logic behind the use of these fins is to be able to change the flow path by changing the geometric parameters of the dividers and evaluate the performance of the valve in different designs. Furthermore, the heat transfer properties of the Tesla valve are investigated to gain a comprehensive understanding of its unique performance. To analyze the thermo-hydraulic performances of the aforementioned valve, two ANN with a 3-4-3-2 architecture are employed. The ANNs are used to obtain models for predicting the performance of the valves. The goal is to reach the results in the shortest time and by performing the least calculations. The present work can be a useful reference in the field of construction of the Tesla valves and conducting research on them. It also can offer researchers an efficient and cost-effective means of accelerating their investigations in the related fields. The design variables in focus are the inner radius of the fins (R), the length of the divider's folded segment (L), and the angle of the divider's folded segment (θ). These selected variables are anticipated to have an impact on the objective functions, namely the Nusselt numbers in the forward (Nu_f) and reverse (Nu_r) directions, as well as the pressure drops in the forward (ΔP_f) and reverse (ΔP_r) directions. The performance of the valve is assessed in relation to its geometry, and an optimal design is presented accordingly. Finally, by using the predictive models and genetic algorithm, optimal designs for different conditions are acquired and compared with the results obtained by numerical methods.

2. Model configuration

In order to discover the optimal design for Tesla valves, a new configuration is introduced, and two stages of the device are chosen for examination in this study (as depicted in Fig. 1a). According to the figure, each stage has a divider containing six arc-shaped fins situated within the curved channel. Fig. 1b presents a visual representation of the structural characteristics and precise measurements of the analyzed valve. The length of the divider's folded segment is denoted by L. The inner radius of the fin in the curved portion of the valve is represented by the parameter R, and the angle of the folded segment of the divider is denoted by θ. The main focus of this article is to examine how the efficiency of Tesla valves is affected by three specific parameters, while keeping the other parameters unchanged. The channels possess a square cross-section, with a hydraulic diameter of 6 mm. Additionally, the outer radius of the curved channel is 8 mm, and the inner curve radius is 2 mm. The Tesla valve under examination is equipped with two ports located at the top and bottom, which function as the entry and exit points for fluid flow (depicted in Fig. 1c and d). During forward flow, the fluid entering from the top experiences minimal resistance and flows smoothly through the straight channel. Conversely, during reverse flow when the fluid enters from the bottom, its inertia causes it to be redirected into the curved channel, leading to an increased pressure drop. The working fluid used in this study is water, and its thermal and physical properties vary with temperature, as specified in Table 1.

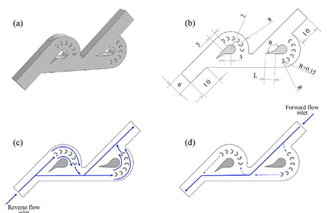

Fig. 1. (a) 3D configuration of the model, (b) structural parameters of the valve, schematics of (c) reverse flow, and (d) forward flow.

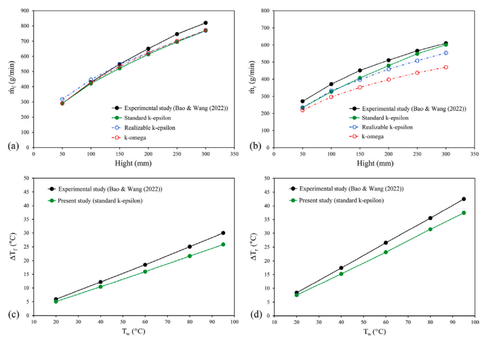

Fig. 4. Comparison of the simulated and experimental results for the Tesla valve using different turbulence models.

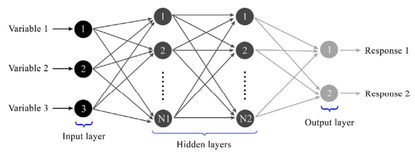

Fig. 5. Schematic of the MLP models.

Table 2
Input variables and the levels at which they vary.

Variable	Variable levels		
	−1	0	+1
R (mm)	0.2	0.6	1
L (mm)	3	4.5	6
θ (degree)	130	150	170

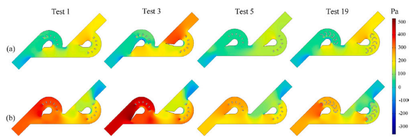

Fig. 7. Pressure variations in the scrutinized Tesla valve with (a) forward flow and (b) reverse flow.

minimal flow entering the curved channels in the forward direction. Whereas test structures 3 and 19 exhibit significant fluid flow through these channels. This difference in flow behavior can be attributed to the angle θ. The angle of the folded segment of the divider, which serves as the structural parameter θ, appears to have a critical influence on the distribution of flow between the main channel and the curved channels. As observed in test structures 3, 5, and 19, changes in this parameter significantly affect the flow patterns and distribution inside the Tesla valve. The primary purpose of a Tesla valve is to create flow resistance in one direction, while allowing relatively free flow in the other. This flow resistance is due to the tortuous path that the fluid must follow as it navigates through the alternating channels and dividers. The angle of the folded segment determines the degree of resistance. When θ is higher, it typically results in greater flow resistance in the forward direction. In other words, fluids have a harder time passing through the valve in one direction, often referred to as the "check valve" direction. This increased resistance in the main channel restricts the flow in that direction. On the other hand, a higher θ can also improve flow in the reverse direction (the "non-check valve" direction). Fluids find it easier to navigate through the curved channels and dividers when flowing in this direction. This allows for more efficient fluid movement when desired. Tesla valves find applications in various fields, including fluid control, pumping systems, and heat exchangers. The ability to control flow based on the θ makes them adaptable to different requirements. The velocity contours and the Nu values presented in Table 4 indicate that the flow behavior within the Tesla valve, particularly through the curved channels, has an impact on thermal performance. It has been mentioned that directing the fluid with a higher flow rate through the longer path of the curved channels leads to a larger heat transfer area. The Nu values provided in Table 4 validate this observation by reflecting the heat transfer characteristics of the various test configurations. Nevertheless, it is worth noting that despite test structure 19 exhibiting a larger heat transfer area and thereby providing higher heat transfer, it demonstrates a lower Nu in both flow directions. This disparity suggests that test structure 19 has a lower heat transfer coefficient compared to tests 1, 3, and 5. The heat transfer coefficient represents the efficiency of heat transfer per unit area and temperature difference. Although test structure 19 achieves more extensive heat transfer due to its larger heat transfer area, it does not effectively utilize the available temperature difference, resulting in a lower heat transfer coefficient. The difference observed suggests that test structure 19 performs heat transfer less effectively compared to tests 1, 3, and 5. This evaluation highlights the significance of fine-tuning the design of the Tesla valve to achieve an optimal combination of heat transfer area and heat transfer coefficient. Such optimization should consider the specific needs and goals of the intended application. In tests 3 and 5, the parameters of L and θ result in increased flow entering the curved channels, leading to a longer path. When the folded segment of the divider (L) is shorter, there is less surface area available for heat exchange between the fluid and the valve structure. This can result in a lower Nu, indicating reduced heat transfer efficiency. Shorter segments restrict the fluid's contact with the valve walls, leading to less heat transfer and potentially slower temperature equalization. Shorter segments tend to offer less resistance to fluid flow. They allow the fluid to move more freely through the channels and dividers, resulting in a lower pressure drop across the valve. However, this may come at the cost of reduced flow control capabilities, as shorter segments may be less effective in directing flow in the desired direction. Conversely, a longer folded segment provides more surface area for heat exchange. It allows the fluid to come into contact with the valve walls over a more extended path. This increased contact area can enhance heat transfer efficiency, leading to a higher Nu. Longer segments promote better mixing of the fluid and the valve structure, facilitating more effective heat exchange. Longer folded segments create more obstacles and a tortuous path for the fluid to navigate. This increased path length and contact with the valve structure introduce higher resistance to flow. As a result, a longer folded segment typically leads to a higher pressure drop across the Tesla valve (refer to Fig. 7). This increased resistance can be advantageous when precise flow control or backflow prevention is necessary. In test 19, although the fins in the fluid path are larger, the ΔP is not considerably high. This can be explained by the effective hindrance of significant fluid entry into the curved channels by the fins. As a result, most of the fluid is directed through the main channel, which offers a relatively shorter flow path and consequently a lower ΔP. Test 21, which combines the structural characteristics of tests 3 and 19, achieves the highest ΔP among all the conducted tests. This combination involves incorporating larger fins, similar to those in test 19, along with an extended folded segment length of the divider, resembling test 3. By partially closing off the main path, a greater amount of fluid is compelled to pass through the curved channels. These factors collectively contribute to a substantial rise in frictional losses, consequently yielding the highest observed ΔP.

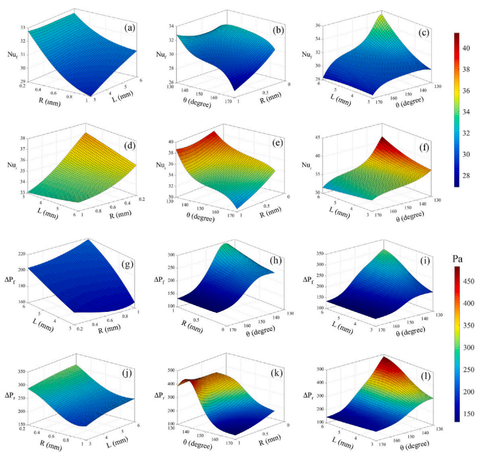

Fig. 10. 3D contours for Nu and ΔP in forward and reverse flow.

Table 10
Evaluation metrics for assessing the performance of the MLP models.

Error function	Mathematical expression	Prediction models			
		Nu_f	Nu_r	ΔP_f	ΔP_r
R^2	$1-\frac{\sum_{i=1}^{m}(T_{num}-T_{pred})^2}{\sum_{i=1}^{m}(T_{num}-\bar{T}_{pred})^2}$	0.984	0.993	0.995	0.999
MAE	$\frac{1}{m}\sum_{i=1}^{m}\lvert T_{pred}-T_{num}\rvert$	0.210	0.201	3.278	2.775
RMSE	$\sqrt{\frac{1}{m}\sum_{i=1}^{m}(T_{pred}-T_{num})^2}$	0.310	0.283	4.052	3.261

They have achieved high levels of accuracy and displayed low errors when predicting the Nusselt numbers (Nu_f and Nu_r) as well as the pressure drops (ΔP_f and ΔP_r) of the Tesla valve. The models exhibit R^2 values that are close to 1, indicating a strong fit between the predicted results and the numerical simulation data. Additionally, they showcase lower MAE and RMSE values, further affirming their

LIU et al. (2022)

black arrow reflects the direction of fluid flow; In the local enlarged view, the streamline results can be clearly seen, which are represented by white lines. Besides, the velocity magnitude in different cases can be well expressed by color bar, and vortex structure can also be observed at the local mutation position. By comparing the color bars in Figure 5(a–c), the better the symmetry, the greater the velocity magnitude in the reverse flow, that is, the greater the pressure drop. However, in forward flow, the symmetrical and asymmetrical Tesla valve systems have almost the same speed magnitude. In addition, the reverse flow could more easily form vortex structures than the forward flow at the local mutation position for the same configuration Tesla valve pipe system under the same flow rate.

Figure 6 shows the velocity distribution at the middle line of the main straight pipe section of the completely symmetric Tesla valve system. The solid line shows the reverse flow, and the dotted line shows the forward flow. The results show that for the same flow rate, the fluid velocity changed more dramatically at the branch pipe section in the reverse flow than in the forward flow. Meanwhile, the velocity increased with the increase in the Reynolds number *Re* at the same position.

From the above simulation results, it can be concluded that symmetrical structure can improve the one-direction flow characteristics of Tesla valve system. It can increase the pressure drop of the fluid in the reverse flow. What's more, fluid inertia is the main factor affecting the one-direction flow characteristics of Tesla valve system. Therefore, an appropriate increase of fluid velocity may be beneficial to improve pressure drop characteristics.

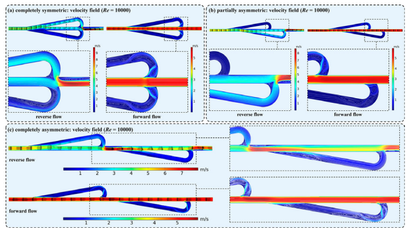

Figure 5. Velocity vector of Tesla valve system (Re = 10,000): (a) completely symmetric, (b) partially asymmetric, and (c) completely asymmetric.

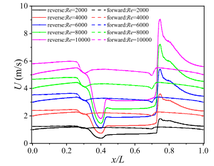

Figure 6. Velocity distribution on the center line of completely symmetric Tesla valve system.

4.1.2. Pressure drop variations

Figure 7 shows the change in the pressure drop ratio *Di*. With the increase in the Reynolds number *Re*, the pressure drop ratio *Di* of both the symmetric and asymmetric Tesla valve systems increased. The Reynolds number *Re* increase was achieved by changing the inlet velocity.

the influence of the other parameters on the completely symmetric Tesla valve system. First, the influence of the shunt angle on the pressure drop ratio of the Tesla valve system is considered. The change of the shunt angle θ ($10^\circ \le \theta \le 60^\circ$) increased by 1° each time, and the variation of the pressure drop ratio *Di* is shown in Figure 9.

The results showed that under the same flow conditions, with the increase in the shunt angle θ, the pressure drop ratio *Di* of the Tesla valve first increased and then decreased. At a small angle ($\theta < 30^\circ$), the system characteristics were relatively good. However, when the shunt angle was large ($\theta > 40^\circ$), the system pressure drop characteristics deteriorated.

4.2.2. Effect of shunt pipe diameter

As shown in Figure 9, when the shunt angle $\theta = 26^\circ$, the system pressure drop ratio *Di* was the maximum. Next, the shunt angle of the symmetric Tesla valve system was set to 26°, and the influence of the shunt pipe diameter d was further considered.

Figure 10 shows the velocity contours of the Tesla valve system for different shunt pipe diameters d (d/D = 0.5, 1.0, 1.5). In Figure 10, the black arrow reflects the direction of fluid flow; In the local enlarged view, the streamline results can be clearly seen, which are represented by white lines. In addition, the velocity magnitude in different cases can be well expressed by color bar.

In the reverse flow, the larger the shunt pipe diameter d, the greater the maximum velocity of the reverse flow of the Tesla valve system. For these three kinds of Tesla valve systems, compared with the forward flow, the reverse flow was more likely to form the energy dissipation of vortex structure in the shunt pipe section, thus having a better 'fluid diode' effect.

Figure 11 shows the effect of the shunt pipe diameter d on the system pressure drop ratio *Di*. The results showed that for three Tesla valve systems with different shunt pipe diameters d, the pressure drop ratio *Di* increased with the increase in *Re*, which is consistent with the conclusion obtained in Section 4.2. Besides, under the same flow conditions, the pressure drop ratio of the system increased with the increase in the shunt pipe diameter d. Taking into account the processing difficulty of the actual pipeline system, it is more appropriate to choose the same diameter of the branch pipe and the main pipe.

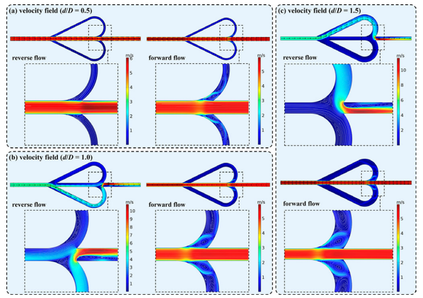

Figure 10. Velocity contours of Tesla valve system for different shunt pipe diameters d (Re = 10,000): (a) d/D = 0.5, (b) d/D = 1.0, and (c) d/D = 1.5.

From the Buckingham Pi theorem (Bridgman, 1922; Buckingham, 1914), the pressure drop $\Delta p = f(L, D, \rho, V, \mu)$ can be replaced by $\Pi_1 = f(\Pi_2, \Pi_3)$, as follows:

$$\Delta p = \rho V^2 f\left(\frac{L}{D}, Re\right) \tag{15}$$

Equation (15) is a universal scaling law for fluid flow in smooth circular tubes, where the function $f\left(\frac{L}{D}, Re\right)$ can be determined either experimentally or numerically.

Next, according to the flow state in a smooth pipe, the force balance relationship in the smooth straight pipe system is considered. The shear stress τ, pressure p, pipe length L, and pipe diameter D satisfy the following equation:

$$\tau = \frac{p_1 - p_2}{L}\frac{D}{4} \tag{16}$$

Furthermore, the dimensionless drag coefficient λ is introduced, and the relationship is as follows:

$$\frac{p_1 - p_2}{L} = \lambda \frac{1}{D}\frac{\rho u_m^2}{2} \tag{17}$$

where u_m is the average velocity of the section. By substituting Equation (17) into Equation (16), we obtain the following formula:

$$\tau = \lambda \frac{1}{D}\frac{\rho u_m^2}{2}\cdot\frac{D}{4} = \frac{1}{8}\lambda \rho u_m^2 \tag{18}$$

In 1911, Blasius (1913) studied a large amount of experimental data and obtained the formula of the turbulent drag coefficient λ in smooth circular tubes:

$$\lambda = 0.3164\left(\frac{\rho u_m D}{\mu}\right)^{-1/4} \tag{19}$$

Substituting Equation (19) into Equation (18) yields the following equation:

$$\tau = \frac{1}{8}\left[0.3164\left(\frac{\rho u_m D}{\mu}\right)^{-1/4}\right]\rho u_m^2 = 0.03955\rho^{3/4}u_m^{7/4}\mu^{1/4}D^{-1/4} \tag{20}$$

By combining Equations (16) and (20), we obtain

$$\Delta p = 0.1582\rho^{3/4}Lu_m^{7/4}\mu^{1/4}D^{-5/4} \tag{21}$$

Therefore, we determine that the dimensional relation Equation (15) in a smooth circular straight pipe can be written as

$$\Delta p = 0.1582L\rho V^2 D^{-1}Re^{-1/4} \tag{22}$$

Further rearranging this, we obtain the following relationship between the dimensionless Euler number *Eu*, length–diameter ratio L/D, and Reynolds number *Re*:

$$\frac{\Delta p}{\rho V^2} = 0.1582\frac{L}{D}Re^{-1/4} \tag{23}$$

For the Tesla valve piping system with a branch (Figure 2), the modification parameter α can be introduced, and Equation (23) can be further modified as follows:

$$\frac{\Delta p}{\rho V^2} \sim (1+\alpha)\frac{L}{D}Re^{-1/4} \tag{24}$$

In Equation (24), when $\alpha = 0$, it corresponds to the smooth circular straight pipe system without branches. For the symmetric Tesla valve system proposed in this paper, α is a multi-factor parameter related to the shunt angle θ, pipe diameter d, and number of valve pairs N of the branch pipeline, namely, $\alpha = \alpha(\theta, d, N)$.

To verify whether the symmetric Tesla valve system with the branch pipes satisfied Equation (24), the functional relationship between pressure drop Δp and velocity V of the Tesla valve unit was first obtained. The finite element simulation data were fitted, as shown in Figure 13. The results showed that the pressure drop Δp and velocity V satisfy $\Delta p \sim V^{7/4}$, which further proved the correctness of Equation (24).

As the influence factors of the modification parameter α are too complicated, only the influence of the number of valve pairs N was considered, and the α in Equation (24) was further improved.

Firstly, the dimensionless parameters L/D and $Re^{-1/4}$ in Equation (24) can be moved to the left side of the formula and further obtained

$$\frac{DRe^{1/4}\Delta p}{L\rho V^2} \sim (1+\alpha) \tag{25}$$

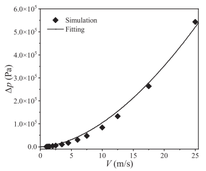

Figure 13. Fitted curve of the simulation results, satisfying $\Delta p \sim V^{7/4}$.

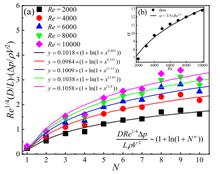

Figure 14. Relationship between the dimensionless parameter $Re^{1/4}D\Delta p/(\rho LV^2)$ and the number of valve pairs *N* for different *Re*.

Next, Figure 14(a) illustrates the variation of $Re^{1/4}D\Delta p/(\rho LV^2)$ with N at different Reynolds numbers. The results show that with the increase in the number of valve pairs N, the dimensionless parameter $Re^{1/4}D\Delta p/(\rho LV^2)$ of the system increased. Furthermore, by fitting the simulated data with the function $y = k(1 + \ln(1 + x^\alpha))$, the scaling law relation can be obtained as follows:

$$\frac{\Delta p}{\rho V^2} \sim (1 + \ln(1 + N^\alpha))\frac{L}{D}Re^{-1/4} \tag{26}$$

where α is a parameter related to the Reynolds number *Re*. Thus, the relationship between α and *Re* was given in Figure 14(b). Naturally, based on data fitting, it is easy to derive that α and *Re* satisfy the function relation $\alpha = 3/5 \times Re^{1/3}$.

Therefore, Equation (27) can be further modified to obtain the scaling law between pressure drop Δp of the Tesla valve system with branches and other parameters as follows:

$$\Delta p \sim (1 + \ln(1 + N^{\frac{3}{5}Re^{1/3}}))\rho V^2 LD^{-1}Re^{-1/4}. \tag{27}$$

4.5. Discussion on the flow characteristics of the Tesla valve

By analyzing the data curves in Figures 5, 7 and 8, we can draw the following conclusions. Under the same fluid state, the completely symmetrical Tesla valve system has better one-direction flow characteristics than the asymmetric Tesla valve system. This is because the symmetrical Tesla valve system has higher fluid resistance in reverse flow. Considering the reverse flow of the fluid in the symmetrical Tesla valve system, based on the inertia of the fluid, when the fluid in the branch pipe section collides with the incoming flow in the straight pipe section, due to the sudden reduction of the cross-sectional area of the pipe, complex flow fields such as local turbulence are formed, resulting in huge energy dissipation of vortexes.

In addition, the flow performance of Tesla valve can be significantly improved by reasonably designing the parameters such as shunt angle, shunt pipe diameter and the number of valve pairs. Additionally, the modified parameter α is obviously a multi-factor parameter related to the shunt angle, shunt pipe diameter and number of valve pairs. In this paper, we have obtained the scaling law considering number of valve pairs as the influence parameters, while the scaling law relationship of shunt angle and shunt pipe diameter as the influence parameters needs to be further considered in the future work.

5. Conclusion

This work focused on the flow characteristics of the Tesla valve piping system with symmetric structure. By using the finite element method, the effects of the geometry, Reynolds number *Re*, shunt angle θ, shunt diameter d, and number of valve pairs N on the pressure drop characteristics of the system were studied in detail. The fluid flow scaling law of the Tesla valve system was determined based on dimensional analysis theory. The main conclusions of this research are as follows:

(1) For the symmetric and asymmetric Tesla valve piping system, the higher the symmetry was, the greater the pressure drop ratio *Di* of the system became. After the symmetry was broken, the pressure drop ratio *Di* decreased.
(2) When the Reynolds number was large ($Re > 2000$), the Hagen number Hg and Reynolds number *Re* of the forward flow and reverse flow of the symmetric Tesla valve system satisfied $Hg \propto Re^2$.
(3) The shunt angle θ had a greater effect on the pressure drop ratio *Di* of the Tesla valve system. When $\theta < 30^\circ$, the pressure drop characteristics of the Tesla system were better. When $\theta > 40^\circ$, the Tesla valve system pressure drop characteristics deteriorated. That is, the Tesla valve system with small angles had better pressure drop characteristics.
(4) With the increase in the branch pipe diameter d, the system pressure drop ratio *Di* also increased. When $d < D$, the pressure drop characteristics of the system were poor.
(5) For the symmetric and asymmetric Tesla valve piping systems, under the same flow conditions, as the

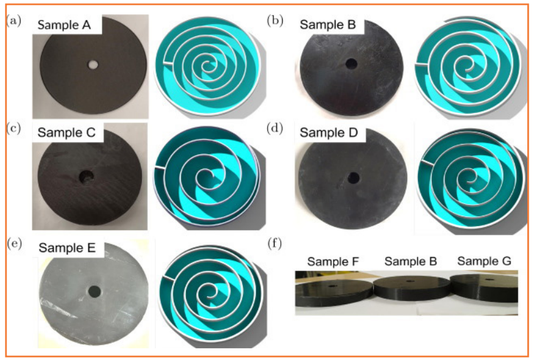

?

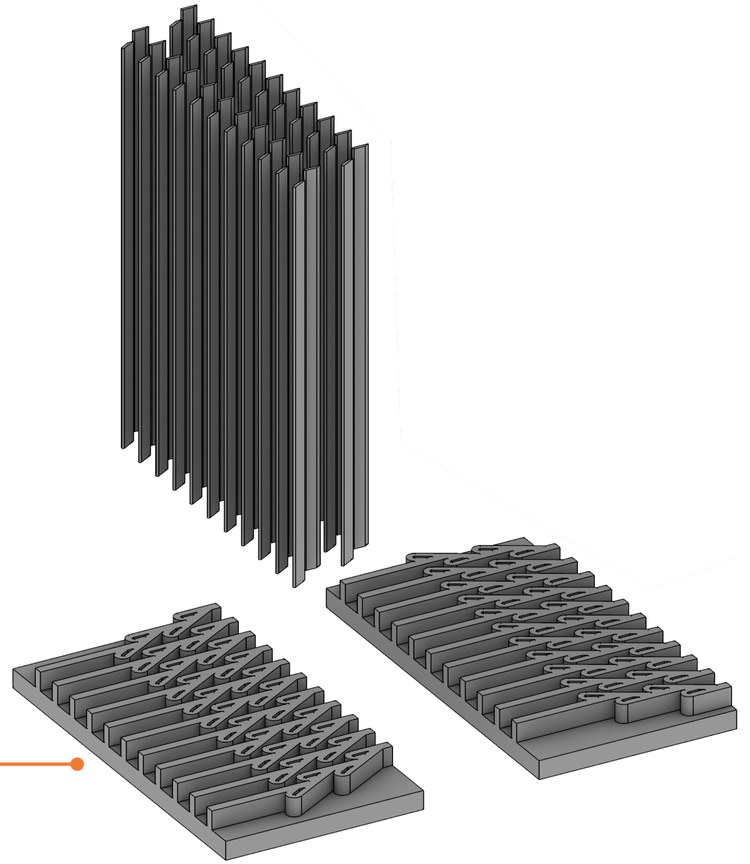

1) IDENTIFY MULTI-FACETED ISSUES

2) IDENTIFY EXISTING SOLUTIONS

3) OPTIMIZE FOR 3D PRINTING

4) INTEGRATE INTO HOLISTIC DESIGN

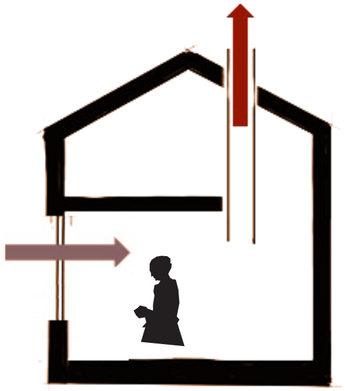

A

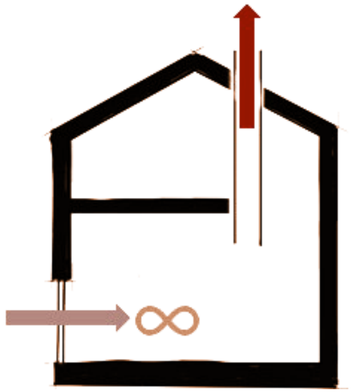

B

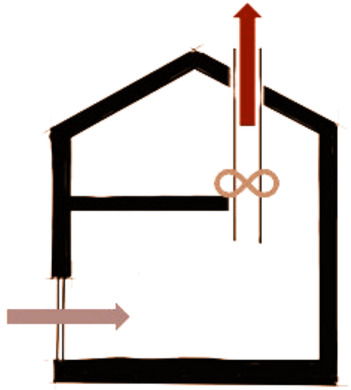

C

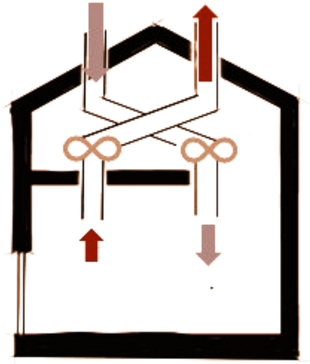

D

1) IDENTIFY MULTI-FACETED ISSUES

2) IDENTIFY EXISTING SOLUTIONS

3) OPTIMIZE FOR 3D PRINTING

4) INTEGRATE INTO HOLISTIC DESIGN

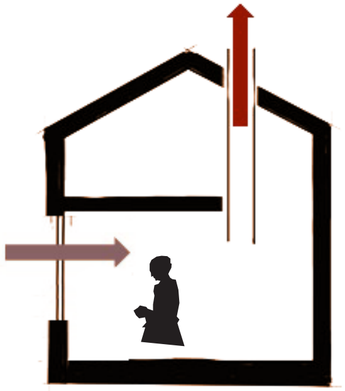

A

B

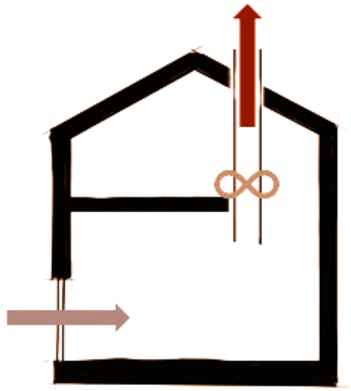

C

D

1) IDENTIFY MULTI-FACETED ISSUES
2) IDENTIFY EXISTING SOLUTIONS
3) OPTIMIZE FOR 3D PRINTING
4) INTEGRATE INTO HOLISTIC DESIGN